Observations of southern hemisphere gamma ray emitting blazars

McKenny, Joy Martina

Observations of Southern Hemisphere Gamma Ray Emitting Blazars

Joy Martina McKenny, M.Sci.

A thesis submitted to the University of Durham in accordance with the regulations for admittance to the degree of Doctor of Philosophy

July 2003

Department of Physics

University of Durham

South Road

Durham

UK

Abstract

This thesis details observations of three Southern hemisphere blazars PKS 2155–304, PKS 2005–489 and PKS 0548–322 using the University of Durham Mark 6 Telescope between 1996 and 1999. The nature of blazars and the physical processes responsible for very high energy emission are also discussed.

A signal above 700 GeV was observed from PKS 2155–304 between 1996 and 1997 but not in 1998 and 1999. One plausible explanation for this is a reduction in sensitivity of the Mark 6.

Evidence for variability of high energy emission from PKS 2155–304 was search for but no firm conclusion was reached. Upper limits to emission from PKS 2005–489 and PKS 0548–322 were determined.

Gamma ray observations for all three objects were tested for correlation with near simultaneous 2–10 keV X-ray emission (taken using the ASM onboard RXTE). No strong evidence for correlation was found. It is worth noting however that gamma ray emission from PKS 2155–304 was detected when the X-ray emission was greatest.

No constraints could be made on models of gamma ray production from blazars. No models were excluded.

Future observations with the new generation of gamma ray telescopes such as H.E.S.S. and CANGAROO will allow more detailed investigation of these objects and many others and their variability while multiwavelength observations will determine the nature of the acceleration processes at work.

Acknowledgements

I would like to thank everyone who has helped me get this far, you all know who you are.

This thesis has been brought to you with the support of PPARC and the University of Durham.

Preface

Joy McKenny was a member of the University of Durham VHE Gamma Ray Astronomy Group for the duration of her Ph.D studentship. During this time she took some observations of PKS 2155–304 using the University of Durham Mark 6 Telescope and re-analysed data for the three Southern Hemisphere blazars PKS 2155–304, PKS 2005–489 and PKS 0548–322 . Some of this work appeared in (Chadwick et al. 2000) as well as in many unrefereed publications.

During her Ph.D she was involved in the development of aluminium mirrors for use on the next generation of Cherenkov telescopes. This work will not form part of this thesis.

Contents

Chapter 1

Gamma ray Astronomy

The study of gamma ray emission from astronomical objects began in the early twentieth century with the balloon experiments of Goeckel (1910) and Hess (1911). These experiments detected what were to become known as cosmic rays. Cosmic ray particles are highly energetic charged particles and are deflected by the magnetic fields in the universe, so that when they reach the Earth, they have retained no information on their origin. Gamma rays however, being high energy photons, are not subject to such deflections and do retain information on their origin. It is this property that makes them of special interest to astronomers. These photons can be observed directly by satellite experiments. However, it is a process known as the Cherenkov effect that makes it possible to observe these photons indirectly from the Earth.

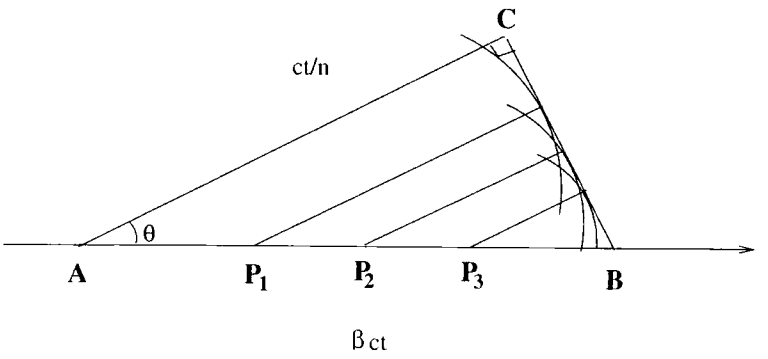

Figure 1.2: Formation of Cherenkov light: A charged particle moving along AB with velocity $\nu > c/n$ through a medium of refractive index n emits Cherenkov radiation at points P. The individual wavefronts at each point lead to a net emission of Cherenkov light over the surface of a cone with semi-vertical angle θ. (Image from S.E. Shaw, Ph.D. Thesis, University of Durham 1999).

asymmetrically polarised and a net electromagnetic field is generated. The result is the emission of Cherenkov radiation. This radiation is emitted at a particular angle, θ, with respect to the direction of motion of the particle (see figure 1.2). If βc is the velocity of the particle and n is the refractive index of the medium,

$$cos\ \theta = 1/\beta n \tag{1.1}$$

with $\beta > 1/n$ and $\theta =$ the Cherenkov angle, by definition. The particle travels faster than the speed of light in the medium, meaning that

- For a given refractive index, there is a threshold velocity $\beta_t = 1/n$ below which no radiation is emitted. The corresponding threshold energy is $E_t = m_0c^2/\sqrt{1-\beta_t^2}$ where m_0 is the rest mass of the particle.

- For an ultra-relativistic particle, where $\beta = 1$ there is a maximum angle of emission

$\theta_{max} = cos^{-1}(1/n)$ for a given medium with refractive index, n.

- Radiation can only occur at frequencies for which $n > 1$. For a typical medium, $n < 1$ in the X-ray and γ–ray regions of the spectrum. Therefore Cherenkov radiation can appear in the microwave, infrared, visible and ultraviolet parts of the spectrum.

Frank & Tamm (1937) carried out the original analysis of radiation produced by an electron moving uniformly in a dielectric medium. They showed that the photon production rate between wavelengths λ_1 and λ_2 for a single charged particle, neglecting dispersion is

$$\frac{dN}{dl} = 2\pi\alpha \left(\frac{1}{\lambda_2} - \frac{1}{\lambda_1} \right) sin^2\theta \tag{1.2}$$

where l is the path length and α is the fine structure constant. The number of photons produced per wavelength interval has an inverse relationship to the wavelength, therefore shorter wavelengths are preferred. The result is that the spectrum of the emitted Cherenkov radiation in air peaks in the UV/blue region of the electromagnetic spectrum.

The threshold energy required for Cherenkov emission in air ($n \simeq 1.0003$) is 21 MeV for electrons, 4.4 GeV for muons and 39 GeV for protons. These energies are quite low compared to typical particle energies in an air shower (see section 1.2), so most charged particles in a cascade will contribute to Cherenkov radiation. Electrons and positrons, being the most common particles, contribute the majority of the photons. The number of photons produced by a typical shower ($\sim$ 500 GeV) is of the order of 10^6. The energy lost by a particle through Cherenkov radiation is normally negligible compared to that lost through ionisation and Bremsstrahlung. For a homogeneous and isotropic medium, radiation is emitted symmetrically in an azimuthal plane about the particle path.

At the altitude of maximum Cherenkov production (~10 km), θ is about 0.8°, which corresponds to a circle of radius 120m at ground level. The increasing density of the air as the shower proceeds downward through the atmosphere increases this emission angle. The combined light from all of the particles in the cascade forms a flash of light seen from the ground (Cherenkov ring), concentrated into a pulse of radiation of duration <6 ns. Figure 1.3 shows the progression of Cherenkov light through the atmosphere, resulting in a Cherenkov ring, as observed. The short duration of the light pulse assists a Cherenkov flash to be distinguished from the much slower Poissonian night sky background.

1.2 Extensive Air Showers

At energies greater than ~10 GeV gamma rays interact with the Earth's atmosphere to produce extensive air showers (EAS) of electrons and positrons. It is these secondary particles that cause the Cherenkov light that is observed by ground-based Cherenkov telescopes. Once the Cherenkov light reaches ground level it is extended over large areas up to about 10^5 m^2. Both gamma rays and cosmic rays can interact with the Earth's atmosphere and eventually result in a Cherenkov light flash. Fortunately there are some fundamental differences between these two types of showers that allow them to be distinguished from each other.

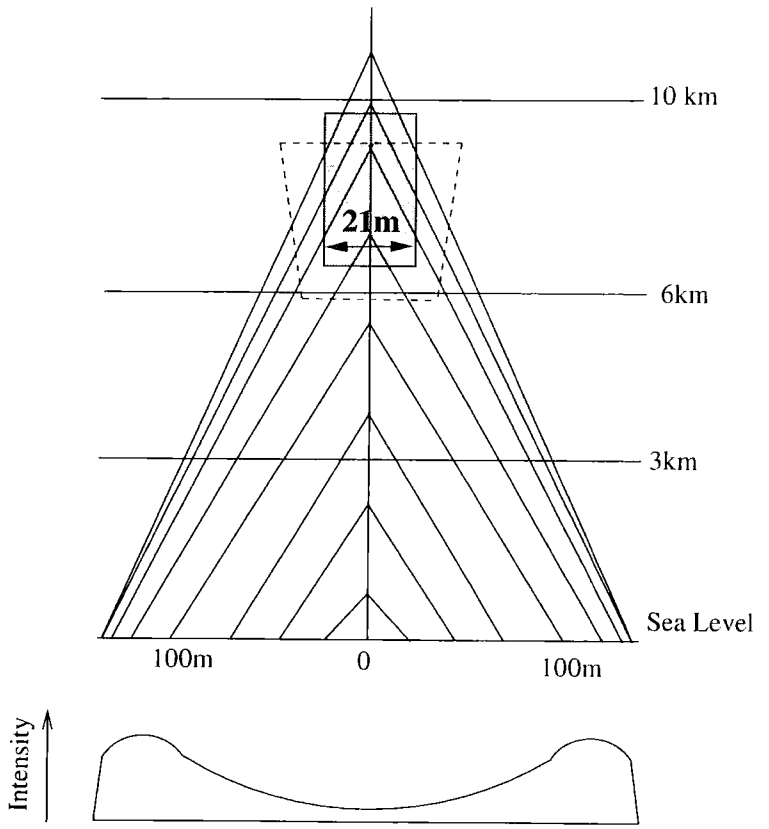

Figure 1.3: The progression of Cherenkov light through the atmosphere. The grey and dashed boxes show the median emission cylinders where one half of the total Cherenkov photons originate from 1 TeV gamma rays and protons respectively. The boxes are centred so that one quarter of the photons are emitted above and one quarter below them. For a 1 TeV photon initiated shower light generated form heights between 6 to 10 km above sea level would fall on the ground within a ring of 110 to 145 m in radius from the shower impact point, if electrons did not multiply scatter. However the directions of the emitters diverge from that of the primary particle due to the multiple Coulomb scattering that they suffer along the way. This broadens the Cherenkov ring, although it does not disappear completely for low energy showers, giving rise to a 'shoulder' in the lateral distribution of the Cherenkov light.

1.2.1 Photon Initiated Cascades

A photon incident on the Earth's atmosphere has a finite chance of undergoing pair production in the electric field of an atom i.e.

$$\gamma + X \rightarrow X + e^- + e^+ \tag{1.3}$$

For electrons and positrons with kinetic energies above 84 MeV the dominant energy loss mechanism is Bremsstrahlung (see section 2.1.4) resulting in:

$$e^- + X \rightarrow X + e^- + \gamma \tag{1.4}$$

The gamma ray produced in the process may carry on to pair produce again, resulting in the generation of more electron-positron pairs. The resulting shower is purely electromagnetic in origin and grows rapidly as it develops through the atmosphere. The maximum number of particles in the shower is reached when the average electron energy drops to below 84 MeV, when ionisation becomes the dominant energy loss mechanism. This point is referred to as shower maximum, since most Cherenkov light is emitted from here. Figure 1.4 shows the development of a gamma ray initiated EAS.

1.2.2 Hadron Initiated Cascades

Proton and other cosmic ray initiated showers are much more complex than gamma ray initiated showers and involve many more physical processes. A very high energy nuclear particle entering the atmosphere has a mean free path of $\sim$80 g cm^{-2}. In general, hadronic cosmic rays penetrate further into the Earth's atmosphere and may initiate cascades at lower altitudes than gamma rays. The most common initial process for a cosmic ray

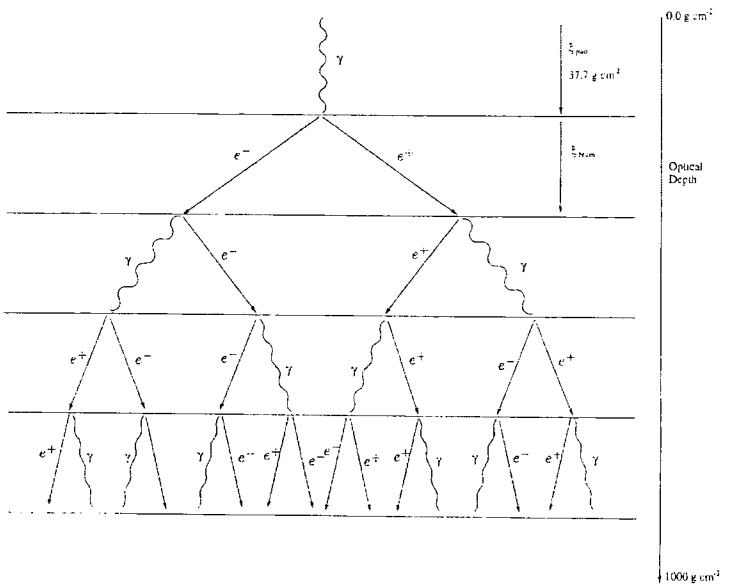

Figure 1.4: A gamma ray initiated extensive air shower as it develops through the Earth's atmosphere. (Longair 1992a)

proton is a proton/proton interaction i.e.

$$p^+ + p^+ \rightarrow p^+ + p^+ + \pi^0 + \pi^+ + \pi^- + \cdots \tag{1.5}$$

This produces pion triplets with large transverse momenta, due to the large opening angle of the pion production interaction. Other daughter nucleons and gamma rays are also produced and continue to interact until they fall below the threshold for pion production (1 GeV). Daughter electrons and positrons are quickly attenuated by ionisation losses. Figure 1.5 shows a typical hadronic air shower. Typical pion and muon interactions are:

$$\pi^0 \rightarrow \gamma + \gamma$$

$$\pi^+ \rightarrow \mu^+ + \nu_\mu$$

$$\pi^- \rightarrow \mu^- + \overline{\nu}_\mu$$

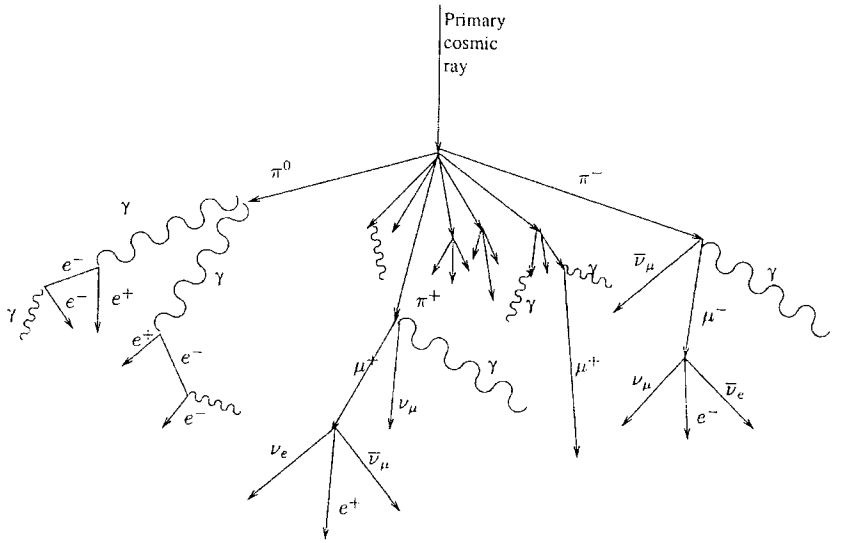

Figure 1.5: A typical cosmic ray initiated extensive air shower progressing through the Earth's atmosphere (Longair 1992a).

$$\mu^+ \rightarrow e^+ + \nu_e + \overline{\nu}_\mu$$

$$\mu^- \rightarrow e^- + \overline{\nu}_e + \nu_\mu$$

Neutral pions have short lifetimes and decay quickly, producing gamma rays that will themselves pair produce and initiate electromagnetic cascades. Charged pions have longer lifetimes and decay to form muons which are long lived relative to pions. Low energy muons may decay to produce electrons or may be brought to rest through ionisation. High energy muons are very penetrating and many survive to reach ground level. The penetrating muon component is a major difference between gamma ray and hadron initiated showers. Hadronic showers also tend to be less compact and lack the uniformity of gamma ray showers due to the large opening angles of the pion interaction and the large transverse momenta given to subsequent particles.

1.3 Hillas Parameters

Events that are observed by a telescope (see section 1.4 for an outline of the design of a ground-based Cherenkov telescope) may be represented by Hillas parameters (Hillas 1985). A graphical representation of these parameters can be seen in figure 1.6.

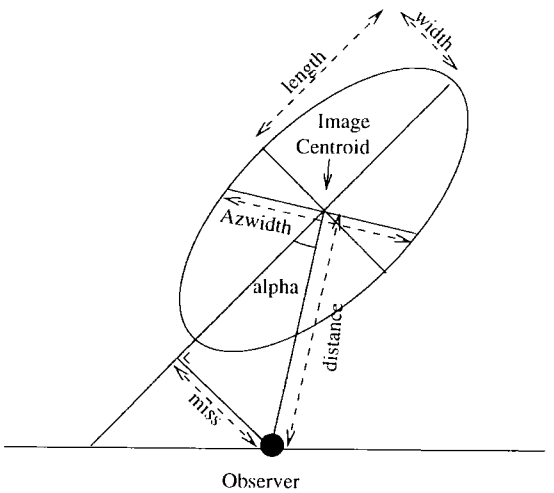

Figure 1.6: A graphical representation of the Hillas parameters to describe a Cherenkov image.

These parameters come under two main categories, those that relate to the shape of the image (size, width and length) and those that relate to the position and orientation of the image (distance, miss and alpha) within the field of view of the observer. Azwidth is a combination of shape and orientation of the image. Section 6.2 describes how an image is defined in the Mark 6 detector.

Hillas parameter	Description
Distance	is the distance from the centroid of the image to the source position.
Size	is the sum of the number of counts in all of the photomultiplier tubes and corresponds to the total light of the event image i.e. the total integrated light content of the shower as viewed by the telescope.
Width	is the rms spread of the light along the minor axis of the image and can be viewed as a measure of the lateral development of the cascade.
Length	is the rms spread of light along the major axis of the image and is a measure of the vertical development of the cascade.
Azwidth	is the rms spread of light perpendicular to the line connecting the centroid of the imaged to the centre of the field of view. This is a measure of both the size and the orientation of the image.
Miss	is the perpendicular distance between the major axis of the image and the centre of the field of view of the detector (the source), a measure of the shower's position and orientation.
Alpha	is the angle between the major axis of the image ellipse and a line joining the centroid of the ellipse to the centre of the field of view of the detector (the source) i.e. $\alpha = \sin^{-1}(\text{miss/distance})$.

Table 1.1: The Hillas Parameters.

Parameter	Description
Eccentricity	relates to the shape of the ellipse best fitting the image. It is defined by the Durham group as $\frac{b}{a}$ where a and b are the semimajor and semiminor axes, respectively.
I-ratio or Concentration	relate to the amount of light within the image expressed as a fraction of the total light within the detector's field of view.

Table 1.2: Other Parameters used in Mark 6 Data Analysis.

Note: I-ratio $= \frac{\text{total light outside the image}}{\text{total light in the camera}}$ is the definition used by the Durham Group. Other groups use a term;

$$\text{concentration} = \frac{\text{total light in the image}}{\text{total light in the camera}} = 1 - (\text{I-ratio}).$$

1.3.1 Gamma ray and Hadron Event Separation by Selection of Hillas Parameters

It is important to be able to identify gamma rays because of the low signal to noise ratio resulting from the cosmic ray background and night sky background events. Monte-Carlo simulations of experiments are used to specify and enhance analysis techniques. Monte-Carlo simulations are also used to predict the gamma ray sensitivity of an experiment. In the absence of a very strong gamma ray signal, a valid telescope model which accurately reproduces the distributions of images of background events is essential to achieving this as it is the only test of how accurately a model may represent gamma rays.

The shape of the image registered by the detector depends on the distance to the core

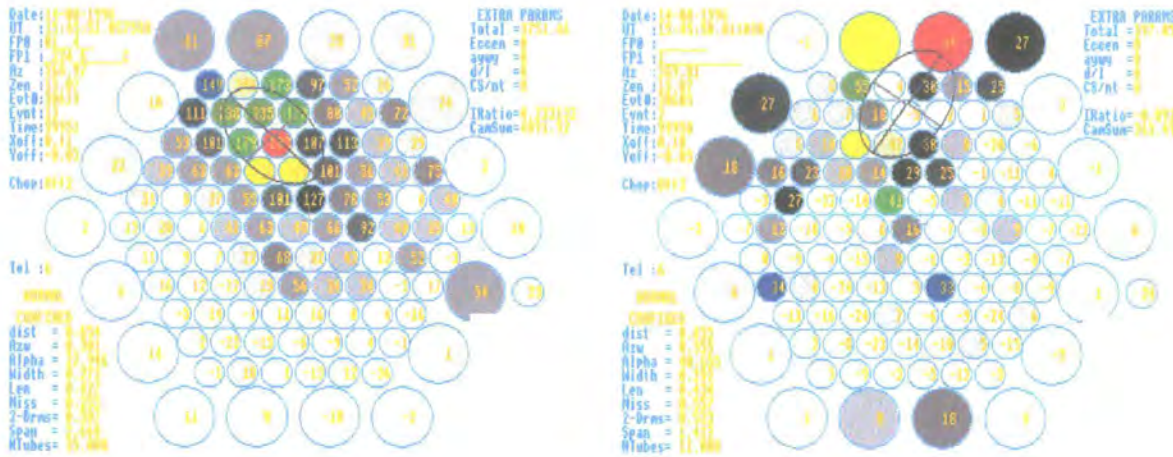

Figure 1.7: This shows a candidate gamma ray event (left) and a hadron event (right) as recorded by the Mark 6 central detector.

of the event. The core of the event is defined to be the centroid of the shower projected onto the ground. When the EAS core is coincident with the optic axis of the detector array, the image is circular in appearance. As the detector becomes increasingly separated from the EAS core, images appear more elongated, until the core is so far away from the detector that most of the Cherenkov photons from the EAS miss the detector. This is true at any distance, since the light pool area is $\sim 10^4$ m^2 and the detector area is $\sim 10^2$ m^2. The longitudinal and lateral development of the EAS give the image its length and width. The different processes involved in electromagnetic and hadronic EAS make the two types of shower look quite different, as seen in figure 1.7. An ellipse describing the image of a hadron initiated Cherenkov event will tend to be wider than that for a gamma ray event and may also include extra light from muons passing close to the detector (Hillas 1996).

For observations of a point source of gamma rays, the most important Hillas parameter

that can be used to reject a large proportion of hadron events is *alpha*. When observing a potential source of gamma rays, the telescope will be pointed towards the source position. The shower producing photons come from a distant point source and travel parallel to the detector's optic axis. The resulting events will have a small value of *alpha*. Hadron events can arrive from anywhere within the field of view and travel in random directions and can therefore have any value of *alpha*.

Results are often presented in the form of an *alpha* plot, which is a histogram of the values of *alpha*. An indication of emission appears as an excess of on-source events at low *alpha* compared to off-source events. By finding the numbers of events on-source, N_{on} and off-source, N_{off} that are below a cut off value of *alpha*, the significance of the detection, σ_{det} can be found (Li & Ma 1983):

$$\sigma_{det} = \frac{N_{on} - N_{off}}{\sqrt{(N_{on} + N_{off})}} \tag{1.6}$$

assuming equal on-source and off-source exposures.

1.3.2 False Source Analysis

As *alpha* contains information on the point of origin of the initial particle, it can also be used to form a map of the significance of any excess on-source signal originating from a particular position on the sky. This can be done using a 'false source' analysis.

This method of proving that gamma ray events originate from a particular point on the sky has been shown by the CANGAROO collaboration (Kifune et al. 1995), Whipple (e.g. Buckley et al. 1996) and by the Durham Group. A false source analysis divides an observation region into a matrix of positions and calculates the value of the Hillas

parameter *alpha* for shape selected events at every position in the matrix. The number of on-source and off-source events with *alpha* less than a specified amount within each matrix element are recorded. This allows a significance map to be produced which shows the most likely origin of the excess events.

1.3.3 Calculation of Gamma Ray Flux from a Source

When there is no clear evidence for emission from a source, an upper limit may be calculated. This is the minimum flux value that would have been detectable in the amount of time the source was observed. The integral flux may be calculated as follows:

$$\text{Upper limit} = \frac{5N}{\text{Effective Area} \times \text{Exposure Duration}} \tag{1.7}$$

where N is the number of excess events that would have to be observed for the given exposure to signify a detection. The criterion required for a significant detection is usually either a 2σ or 3σ excess and the corresponding limits are referred to as 2σ or 3σ upper limits. All upper limits quoted are 3σ upper limits unless otherwise stated. Equation 1.7 assumes that the gamma ray spectrum and the cosmic ray spectrum have the same spectral index, $\gamma = 2.6$. The effective area of the telescope at a given energy is dependant on the energy threshold of the telescope which relates to the mirror area. The effective area of the Mark 6 was 1.7×10^5 m^2 at 700 GeV (Nolan 2002) for observations at zenith angles less than 45°. The retention factor of gamma rays by the Mark 6 is 20% giving rise to the factor of 5 in the numerator of equation 1.7.

One major advantage of ground based gamma ray telescopes is that their effective sensitive area, A_γ, for gamma ray showers is determined not by the size of the telescope

collecting area but by the size of the Cherenkov light pool on the ground, which is much larger.

1.4 Ground-based Cherenkov Telescopes

1.4.1 Principles of Design

An estimate of the size of A_γ can be made for a Cherenkov detector with a given field of view, $\alpha°$.

The furthest gamma ray EAS falling parallel to the detector optic axis, which can be detected, will produce an image with maximum intensity just at the edge of the field of view. This will be at a distance, d from the detector, equal to the vertical height h. A simple geometric approximation for a small field of view gives the radius, $r \approx \frac{\pi\ \alpha\ d}{180}$ of the light pool on the ground. A_γ is then simply the area of the circle with radius r. For showers observed at the zenith, a depth of maximum of ~300 g cm^{-2} gives h~10 km and A_γ ~2×10^5 m^2, using a 3° field of view.

At larger θ (where $\theta = 0$ is the zenith), an EAS which maximises after traversing 300 g cm^{-2} of atmosphere will maximise at a vertical depth in the atmosphere equal to $300\times\cos\theta$. In an exponential atmosphere this will be at a higher vertical altitude, h, than in the $\theta = 0°$ case. This gives a larger value for $d/cos\theta$ and hence an increased A_γ. At $\theta = 60°$ the same energy shower which maximised at 300 g cm^{-2} in the vertical case will actually maximise at a vertical depth of 150 g cm^{-2}. A suitable atmospheric model returns $h = 13.5$ km for this grammage. A_γ is then about five times larger than in the vertical case since $d = \frac{13.5}{cos\theta} = 27$ km.

Observing Cherenkov events at low elevation has been suggested as a way of measuring the energy spectra of astronomical objects at >10s of TeV (Sommers et al. 1987, Chadwick et al. 1999b). At these energies experiments with large A_γ are necessary as the flux of photons from such objects is small. Unfortunately A_γ for gamma ray collection is similar to that for the hadronic cosmic ray background, A_h. The hadron flux can be larger than that from a gamma ray source by factors of several hundreds. Some method of distinguishing gamma ray Cherenkov events from the background needs to be applied if the experiment is to be a success.

1.4.2 Basic Cherenkov Telescope Design

A simple Cherenkov telescope consists of three main components; a light collector and a photon detector, placed on a steerable mounting system. A Cherenkov event occurs in a very short time, ~5 ns, because atmospheric Cherenkov photons result from highly relativistic particles. This time spread is due to the difference in arrival times of photons emitted at the beginning and end of the air shower development which relates to an altitude range of $\approx 6 - 10$ km. There is an additional spread in the arrival time of Cherenkov photons because of the finite thickness of the air shower particle front (arising from multiple Coulomb scattering). This makes photomultiplier tubes with their fast rise times and high gains ideal detectors for Cherenkov telescopes. The choice of window glass and photo-cathode material can also be optimised for maximum sensitivity in the $300 - 500$ nm range in which most of the Cherenkov light is emitted.

Several texts (Fegan 1997, Weekes 1988) define a quantity, N_σ, which is the statistical significance, in standard deviations, obtained by viewing a source of gamma rays with

spectral index α.

$$N_\sigma \propto \frac{A_\gamma \sqrt{T} E_T^{(0.8-\alpha)}}{\sqrt{A_h \Omega}} \tag{1.8}$$

Hence the statistical significance may be enhanced by increasing the amount of observation time of the source, T, and reducing the energy threshold of the telescope, $E_T \propto S_{min}$, where S_{min} is the minimum Cherenkov light signal detectable by a Cherenkov telescope. Minimising the solid angle of the sky viewed by the telescope, Ω, can also increase N_σ although it must remain large enough to detect gamma rays. Current detectors have fields of view with typical radii of $\sim 2°$. In a simple detector A_γ and A_h are given by the size of the light pool at ground level and are similar for gamma rays and hadrons. However, the value of N_σ can be further increased by filtering data to discriminate between gamma ray and hadron initiated events. By removing hadrons from the dataset and retaining gamma rays, A_h can effectively be made smaller than A_γ. When the design of a Cherenkov telescope includes further methods of hadron rejection, equation 1.8 includes a further term

$$N_\sigma \propto Q \frac{A_\gamma \sqrt{T} E_T^{(0.8-\alpha)}}{\sqrt{A_h \Omega}} \tag{1.9}$$

The quality factor Q,

$$Q = \frac{F_\gamma}{\sqrt{F_h}} \tag{1.10}$$

is the increase in the significance of a gamma ray signal when an analysis procedure retains fractions F_γ and F_h of the gamma ray and hadron data, respectively.

The sensitivity of the telescope to Cherenkov photons can be increased by running the photon detectors at a higher gain. However, this causes a high number of 'accidental' triggers from the night sky background as well as actual Cherenkov events. A reduction

in accidental triggers can be obtained by reducing the integration time, t, of the detectors, although in practice this may be difficult. Coincidence techniques can be used to allow the operation of the detector system at maximal gain whilst allowing an acceptable amount of accidental triggers. The technique requires signals from more than one paraxial optical/detector system to pass a discriminator threshold within a narrow time interval, Δt, to trigger the telescope. Assuming an exponential distribution of trigger times, the rate, R, at which a trigger condition requiring C detectors to pass a discriminator threshold is satisfied by chance is given by

$$R = C! n^C \Delta t^{(C-1)} \tag{1.11}$$

where n is the count rate of each detector. Increasing C allows the discriminator threshold to be reduced and hence the sensitivity may be increased.

As well as its effect on increasing N_σ, a reduction in detectable threshold energy is scientifically very important to close the gap in the observed electromagnetic spectrum between ground and space based experiments.

1.4.3 The University of Durham Mark 6 Telescope

The University of Durham Mark 6 telescope (hereafter, the Mark 6) was commissioned in 1995 and decommissioned in Spring 2000. It was located in Narrabri, NSW, Australia. The telescope was designed to detect ~200 GeV gamma rays incident at Earth and to achieve good discrimination between gamma rays >300 GeV and the hadron background. The Mark 6 comprised:

- Three 42m^2 mirrors, each of focal length 7 m. Each mirror consisted of 24 segments

manufactured in a novel way by the Durham group from a combination of highly reflective aluminum, aluminium honeycomb, sheet aluminium and epoxy.

- A central detector of 109 photomultiplier tubes (PMTs) (91 one-inch and 18 two-inch). Left and right detectors each with 19 two-inch hexagonal PMTs.
- Point spread function of the mirrors 0.18°
- Position pointing ±0.008°

The Mark 6 telescope used the three-fold coincidence system whereby an event must have been detected in all three detectors within 10 ns in order for it to be recorded. By employing a coincidence trigger, the number of accidental triggers was reduced and the background was reduced as local muons were not recorded.

The three detectors were arranged so that corresponding left and right PMT pairs viewed the same area of sky as a group of seven 1″ photomultipliers in the central camera. For the telescope to trigger a four-fold temporal and three-fold spatial trigger was applied requiring both corresponding left and right photomultipliers plus any contiguous two of the seven one-inch photomultipliers in the central camera to pass a discriminator threshold.

The Energy Threshold of the Mark 6

The effective sensitive area, A_γ, of a Cherenkov telescope has been shown to be dependent on the distance from the observer to the extensive air shower (see section 1.2). Therefore A_γ is a function of primary energy and the zenith angle of observation. The energy threshold of the Mark 6 has been determined by Monte Carlo simulations (Nolan 2002).

The energy threshold is defined as the energy at which the detected gamma ray flux is at a maximum and is the peak of the function created by multiplying A_γ by the intrinsic differential energy spectrum. Figure 1.8 shows A_γ of the Mark 6 telescope and the convolution of this function with a differential energy spectrum of $E^{-2.6}$, the value for PKS 2155–304. The threshold of this telescope for this spectrum at 30° was $E_T \sim 0.7$ TeV.

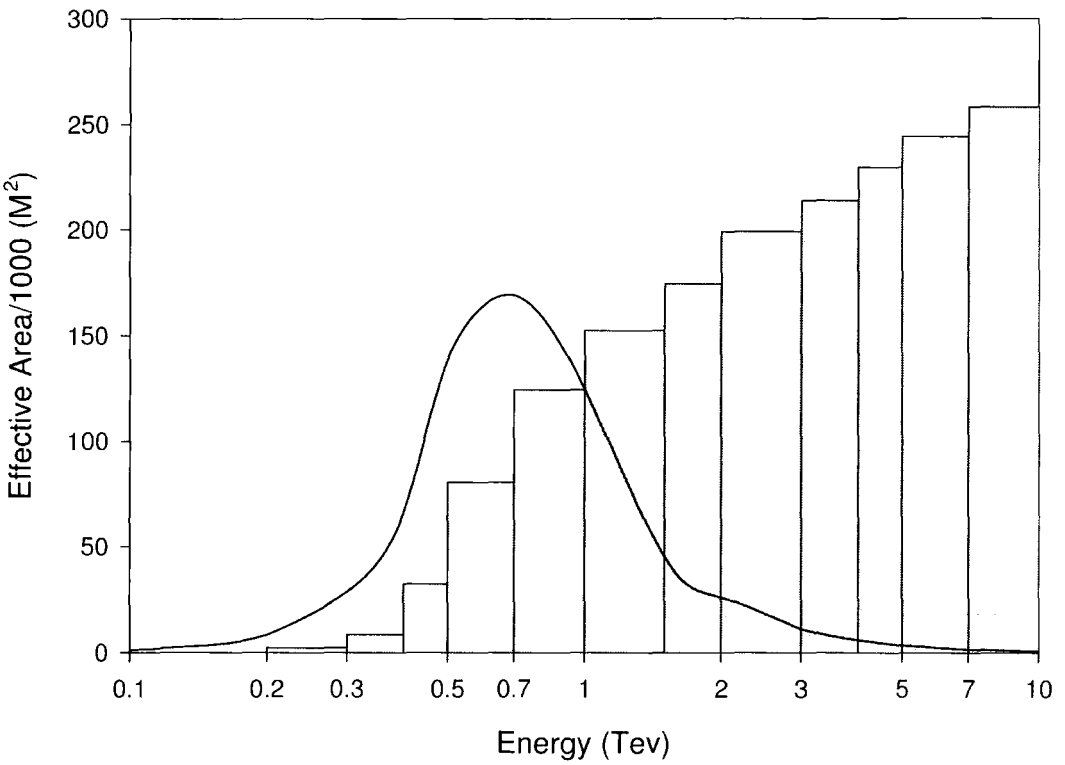

Figure 1.8: The histogram gives the variation of the effective area of the telescope with the energy for gamma ray showers. The curve, having a vertical scale in arbitrary units shows the form of the triggering spectrum for a power law differential source energy spectrum of index -2.6 (Aye et al. 2001).

1.5 Other Experiments

There are a variety of experiments currently in operation studying high energy emission from astrophysical objects. In the Northern Hemisphere there are the VERITAS 10m and MAGIC. In the Southern Hemisphere there are H.E.S.S. and CANGAROO III. These four experiments are ground based Cherenkov telescopes. H.E.S.S. and CANGAROO II are telescope arrays while MAGIC and the VERITAS 10m are stand alone single dishes.

Gamma ray satellites such as GLAST will observe the MeV to GeV regime. GLAST is due for launch in 2006. There are a number of solar array experiments, CAT, STACEE, etc. that also operate in these energy ranges. Milagro is a 60m$\times$ 80m pond, covered with a light-tight barrier, using 450 PMTs and 1.5m of water to detect Cherenkov radiation from air shower particles reaching the ground. An additional layer of PMTs at the bottom of the pond detects muons and helps to distinguish gamma ray showers from hadronic showers. It is able to continuously observe the overhead sky in the TeV energy regime and has detected the Crab Nebula and Mrk 421 at TeV energies (Atkins et al. 2004). These experiments will not be discussed here. The ground-based Cherenkov telescopes in operation, will be briefly outlined below.

1.5.1 CANGAROO

The Collaboration of Australia and Nippon (Japan) for a Gamma Ray Observatory in the Outback, CANGAROO, is an international collaboration aiming to study the existence and properties of very high energy gamma rays from celestial objects in the southern sky by using imaging atmospheric Cherenkov telescopes. It is based at Woomera, South

Australia, Australia.

CANGAROO II has a parabolic mirror of 10m diameter comprising 114 80cm diameter mirrors on an alt-azimuth mount. It has a focal length of 8m and a 4° field of view. It has a point image size of 0.2° at the focus. The experiment's pointing accuracy is less than 1arcmin. It has a maximum pointing speed of $0.5°s^{-1}$.The detector consists of 552-pixel photomultipliers. It has an energy threshold of 100GeV. CANGAROO III is an array which will consist of four telescopes similar to CANGAROO II. It is due for completion in 2003.

1.5.2 H.E.S.S. Phase I

The High Energy Spectroscopic System (H.E.S.S.) collaboration members are from universities and scientific institutions in Europe and Africa. Phase I consists of four imaging atmospheric Cherenkov telescopes (IACTs) situated on the Gamsberg plateau in Namibia, a site of excellent astronomical quality. This array will observe gamma rays above 50 GeV. The first telescope saw first light on 11^{th} June 2002 with the other three due to come online in 2003/4. Its position in the Southern Hemisphere will make it possible to probe the centre of the Galaxy and look for evidence of dark matter through detection of neutralino annihilation line emission.

1.5.3 H.E.S.S. Phase II

Phase II is likely to comprise a further 8 to 12 telescopes of similar design to phase I. Construction is due to begin in 2004/5 with each additional telescope to come online in six-monthly intervals. The design however, is not yet fixed and as technology develops a

more advanced design may be realised. The sensitivity will be increased and it will be the largest IACT array in operation. It is likely that this array will be used to observe multiple sources at the same time.

1.5.4 MAGIC

MAGIC is an imaging Cherenkov telescope inaugurated in October 2003. MAGIC has the world's largest mirror and new technology photomultipliers and is located on the Roque de los Muchachos, La Palma. The mirror surface is $\sim$ 230 m^2. MAGIC can detect gamma rays at an energy threshold of $<$ 15 GeV. MAGIC's active mirror surface of 234 sq.m. is made of square elements 50cm $\times$ 50cm with f/D = 1.03. Its camera has a 1.5m diameter, with an inner hexagonal area of 397 one-inch PMTs surrounded by 180 PMTs of 1.5" diameter, arranged in four concentric rings. All tubes have an effective quantum efficiency of 25 to 30%. The threshold for gamma ray detection is around 30 GeV with classical PMTs; future high-QE red-extended PMTs will bring the threshold down to 12 GeV. The maximum time to reposition the MAGIC telescope anywhere on the observable sky should be no more than 20 seconds despite a moving weight of $\sim$ 40 tons. This allows it to respond to burst alerts.

1.5.5 VERITAS

The Very Energetic Radiation Imaging Telescope Array System, VERITAS, will be a new ground-based gamma ray observatory with an array of seven 12m optical reflectors for gamma ray astronomy in the GeV–TeV energy range. VERITAS will be constructed in two phases, with a four telescope array complete in 2005 and a seven telescope array

complete in 2007. The new telescope design will be based on the design of the existing 10 m gamma ray telescope of the Whipple Observatory. It will consist of an array of imaging telescopes which will be deployed so that they will permit the maximum versatility and will give the highest sensitivity in the 50 GeV–50 TeV band (with maximum sensitivity from 100 GeV–10 TeV).

The seven identical telescopes in VERITAS, each of aperture 12 m, will be deployed in a filled hexagonal pattern of side 80 m; each telescope will have a camera consisting of 499 pixels with a field of view of 3.5°.

Chapter 2

Physical Processes for Production of Radiation from Active Galactic Nuclei

This chapter discusses the important physical processes in the field of very high energy (VHE) gamma ray astronomy. In particular, the processes responsible for the emission of radiation from AGN will be discussed. Cyclotron radiation (section 2.1.1) is emitted by electrons spiralling along magnetic fields. Synchrotron radiation (section 2.1.2) is the relativistic analogue of cyclotron radiation and occurs in the jets of active galactic nuclei.

Observations of the Crab Nebula, one of the first known gamma ray emitters, have allowed astronomers to determine the nature of many of the processes responsible for high energy emission. The optical nebula is centered on the complex structure around the pulsar which must have an ambient magnetic field of $\sim 3 \times 10^{-4}$ G, from equipartition arguments. This is probably where the observed gamma radiation originates. Gould

(1965) stated that if the amorphous radiation from radio to X-rays from the Crab Nebula was due to synchrotron radiation by relativistic electrons, then these same electrons should Compton scatter the photons, boosting them to gamma ray energies.

Thomson scattering (section 2.1.5) takes place between photons and stationary electrons. The relativistic analogue is Klein-Nishina scattering (section 2.1.6) which has a lower probability of occurring which is responsible for the decline in the gamma ray production via the synchrotron self-Compton process (section 2.2).

2.1 Physical Processes at the Source

For high energy electrons the most relevant processes which occur are (i) elastic or inelastic collisions with atoms or ions resulting in emission of Bremsstrahlung photons during the scattering process, (ii) Compton scattering with photons of the radiation field and (iii) emission of synchrotron radiation by interaction with a magnetic field. These are photon-producing processes; detection of these photons can give information on the interactions taking place in the medium.

2.1.1 Cyclotron Radiation

Cyclotron or Larmor radiation is emitted by non-relativistic electrons spiralling along magnetic field lines. This is the non-relativistic analogue of synchrotron radiation (see section 2.1.2). Most of the energy of the cyclotron radiation is emitted at the cyclotron frequency, ν_c:

$$\nu_c = \frac{eB}{2\pi m_e c} \tag{2.1}$$

where e is the charge of the electron, B is the magnetic field strength, and m_e is the mass of the electron (Zeilik, Gregory and Smith 1992). The energy loss rate due to Larmor radiation is

$$-\left(\frac{dE}{dt}\right)_{rad} = \frac{q^2|\ddot{r}|}{6\pi\varepsilon_0 c^3} \tag{2.2}$$

where $(\frac{dE}{dt})_{rad}$ is the total radiation rate, q is the charge of the particle, $\ddot{r}$ is the proper acceleration of the charged particle and ε_0 is the permittivity of free space (Longair 1992a). The radiation loss rate is that measured in the instantaneous rest frame of the particle. The radiation is polarised, with the electric field vector lying in the direction of the acceleration vector of the particle as projected onto the sphere at a distance r from the charged particle.

2.1.2 Synchrotron radiation

This is the electromagnetic radiation emitted by a charged particle moving in a magnetic field at a speed very close to the speed of light (see figure 2.1). The emission appears in a continuous spectrum extending over a very wide range of wavelengths. According to Kembhavi & Narlikar (1999), for a single electron, the emitted power due to synchrotron radiation is

$$P_s = \frac{2}{3} r_0^2 c \beta^2 \gamma^2 B^2 \sin^2 \alpha \tag{2.3}$$

where, α = pitch angle, which is the angle between the velocity vector and the direction of the magnetic field, $r_0 = \frac{e^2}{mc^2}$, $\beta = \frac{v}{c}$, and γ is the Lorentz factor of the electron.

The power is emitted mainly in a narrow cone of opening angle $\sim \frac{1}{\gamma}$ around an axis coinciding with the velocity vector. The power emitted is $\propto m^{-2}$, which implies that syn-

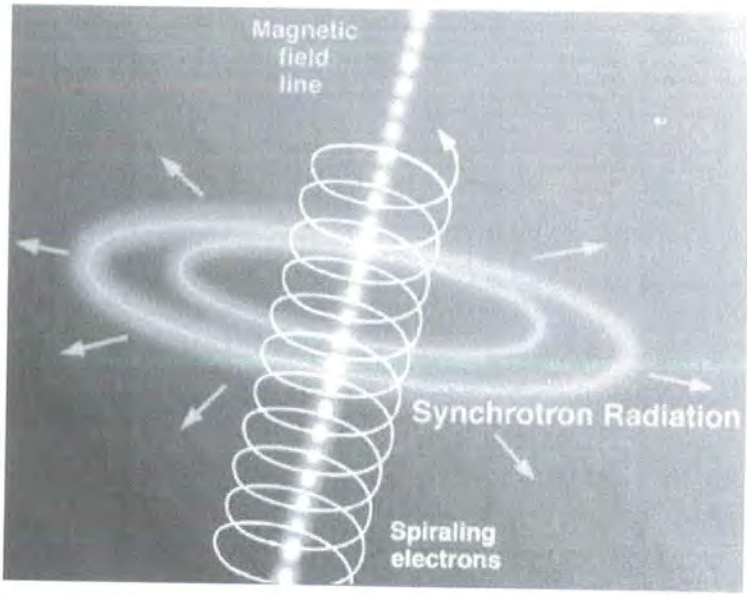

Figure 2.1: Synchrotron radiation emitted by a relativistic electron as it spirals around a magnetic field line. Image courtesy of the "Gemini Observatory".

chrotron radiation from an electrically neutral plasma is overwhelmingly from electrons. If there is equipartition of energy between the protons and electrons the power emitted is $\propto m^{-4}$.

Averaging over pitch angle

$$P_s = \frac{4}{3}\sigma_T c\beta^2\gamma^2 U_B \tag{2.4}$$

where σ_T = Thomson scattering cross section, and $U_B = \frac{B^2}{8\pi}$ = energy density of the magnetic field. For relativistic electrons $\beta \approx 1$. An important effect of the relativistic motion is that the radiation is concentrated in a narrow cone with its axis in the direction of the velocity vector and half-angle $\theta \sim \frac{1}{\gamma}$.

Consider an ensemble of electrons with energy in the range (E_1, E_2). Let $n(E)dE$ be the number density of electrons with energy between E and $E + dE$. The power emitted

by the electrons as a function of the frequency of the emitted radiation is given by

$$P(\nu) = \int_{E_1}^{E_2} P(E,\nu) n(E) dE \tag{2.5}$$

The observed radio spectra from emission regions which are transparent to the radiation are of the form $P(\nu) \sim \nu^{-\alpha}$, where α is a constant. In the synchrotron as well as the Compton case (section 2.1.7), power law emission can be produced if the electrons have a power law distribution of energy.

Figure 2.2 shows the frequency dependence of the synchrotron spectrum emitted by an electron.

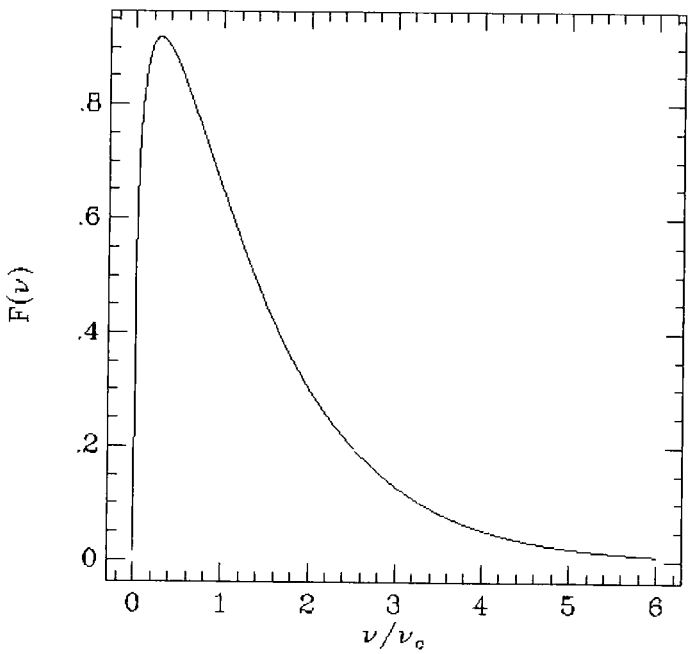

Figure 2.2: An example of a synchrotron spectrum showing the characteristic peak emission at $0.29\nu_c$ (Ginzburg & Syrovatskii 1965).

2.1.3 Absorption of Synchrotron Emission

The synchrotron spectrum emitted by an ensemble of electrons with a power law distribution of energy has the simple power law distribution form $P(\nu) \sim \nu^{-\alpha}$ where α is a constant. Such a spectrum will only be seen if there is no absorption of the photons by the emitting region or by the intervening matter such as the host galaxy, intervening galaxy or even our own Galaxy. Spectra from optically thin emission regions sometimes show signs of absorption in the radio which can be traced to thermal absorption in the galactic interstellar medium.

Synchrotron Self Absorption

In this process, synchrotron emission is accompanied by absorption, in which a photon interacts with a charged particle in a magnetic field and is absorbed, giving up its energy to the charge. The change in intensity due to absorption, $dI(\nu)$, in traversing a distance ds is

$$dI(\nu) = j_\nu ds - \alpha_\nu I(\nu) ds \tag{2.6}$$

where α_ν is the absorption coefficient and j_ν is the emission coefficient. If the emitting region is homogeneous and has size $\sim l$

$$I(\nu) = \frac{j_\nu}{\alpha_\nu}[1 - exp(-\alpha_\nu l)] \tag{2.7}$$

As illustrated in figure 2.3, if the source is optically thin i.e. $\tau_\nu = \alpha_\nu l \ll 1$, the spectrum of radiation leaving the medium is $I(\nu) \sim j_\nu l \sim \nu^{-\alpha}$. If the source is optically thick $\tau_\nu \gg 1$ and $I(\nu) \sim j_\nu \sim \nu^{\frac{5}{2}}$. Since the synchrotron self-absorption co-efficient is inversely dependent on ν, a given source will be optically thick below the frequency ν_a at which

$\tau_a \simeq 1$ and may be considered optically thin at $\nu > \nu_a$. If the source subtends a solid angle $\Delta\Omega$ to the observer, the flux density received is $F(\nu) = I(\nu)\Delta\Omega$, and

$$F(\nu) \propto \nu^{-\alpha}, \quad \nu > \nu_a$$

$$F(\nu) \propto \nu^{\frac{5}{2}}, \quad \nu < \nu_a$$

Synchrotron self-absorption produces an inverted spectrum of power law form with spectral index of $\frac{5}{2}$ regardless of the value of the power law index in the unabsorbed part.

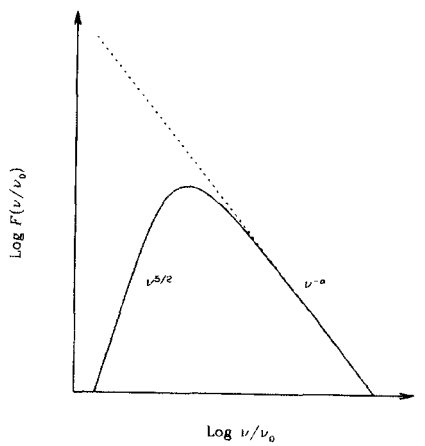

Figure 2.3: The turnover in the synchrotron spectrum due to synchrotron self-absorption. ν is the observed frequency while ν_0 is the frequency at which the self-absorption optical depth becomes unity. The dotted line shows how the optically thin $\nu^{-\alpha}$ spectrum would extend to low frequencies in the absence of self-absorption (Kembhavi & Narlikar 1999).

However, a slope of $\frac{5}{2}$ has never been seen, and what is found in compact sources is a spectral index considerably flatter than that found in extended sources or in spectra that are complex and undulating. This is due to different parts of the source becoming

optically thick at different frequencies. Therefore the absorbed spectrum is a superposition of spectra that peak in these different parts of the source.

2.1.4 Bremsstrahlung

Radiation due to the acceleration of a charged particle in the Coulomb field of another charged particle is called Bremsstrahlung. Bremsstrahlung (breaking radiation) or free-free radiation results when a charged particle is decelerated and loses energy in the form of electromagnetic energy. The deceleration may be caused by either electric or magnetic fields, and Bremsstrahlung is therefore associated with the deceleration of electrons in the electrostatic fields of ions and the nuclei of atoms. See figure 2.4.

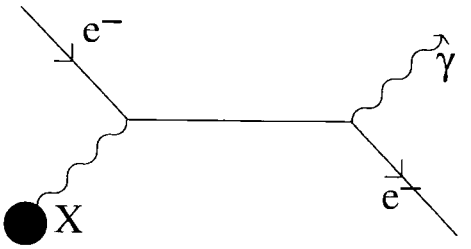

Figure 2.4: Feynman diagram for Bremsstrahlung.

When $\hbar\omega \ll \gamma m_e c^2$

$$\frac{\omega' - \omega}{\omega} = \frac{v}{c}\frac{(\cos\theta - \cos\theta')}{[1 - (\frac{\nu}{c})\cos\theta']} \tag{2.16}$$

To the first order, the frequency changes are $\propto v/c$ if θ and θ' are randomly distributed and the photon is as likely to increase as decrease in energy. It is only to the second order i.e. v^2/c^2 that there is a net energy gain for the photons. If a photon of energy $\hbar\omega$ collides with a stationary electron, the centre of momentum frame moves at velocity

$$\frac{v}{c} = \frac{\hbar\omega}{m_e c^2 + \hbar\omega} \tag{2.17}$$

Therefore if the photons to be scattered have energy $\hbar\omega \geq m_e c^2$, a proper quantum relativistic scattering cross section must be used.

However, if the photons are of low energy $\hbar\omega \ll m_e c^2$, but the electron is moving ultra-relativistically with $\gamma \gg 1$, then the centre of momentum frame moves with a velocity close to that of the electron and in this frame the energy of the photon is $\gamma\hbar\omega$. If $\gamma\hbar\omega \sim m_e c^2$, the Klein Nishina cross section should be used.

Scattering by nuclei can be neglected as they cause very much less scattering than electrons by a factor of $\sim (m_e/m_N)^2$ where m_N is the mass of the nucleus.

2.1.8 Inverse Compton Scattering

High energy electrons scatter low energy photons to high energy so that in the Compton interaction the photons now gain and the electrons lose energy. When the photon gains energy the process is called inverse Compton scattering. Consider the scattering of low energy photons by ultra-relativistic electrons. The high energy electrons scatter low energy photons to high energies so that in the Compton interaction the photons gain and the

electrons lose energy as shown in diagram 2.7.

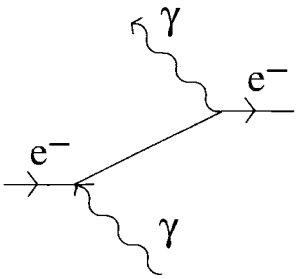

Figure 2.7: Feynman diagram for inverse Compton scattering.

There is a net gain in the energy of a photon when it is struck by a fast-moving electron; the electron passes over a small amount of its energy to the photon and the photon's wavelength decreases. If an electron with velocity βc and Lorentz factor γ encounters a low energy photon of frequency ν', the photon appears in the rest frame of the electron to have a frequency of:

$$\nu_e = \nu'(1 + \beta \cos\theta) \tag{2.18}$$

Where θ is the angle between the incident electron and photon directions. If $h\nu \ll m_e c^2$ the photon can undergo Thomson scattering by the electron, being redirected over a wide possible range of angles in the rest frame of the electron. Figure 2.8 shows the emission spectrum resulting from inverse Compton scattering.

Energy Loss due to Inverse Compton Scattering

The energy loss rate due to inverse Compton scattering is

$$\frac{dE}{dt} = \frac{4}{3}\sigma_T c U_{rad} \left(\frac{v^2}{c^2}\right) \gamma^2 \tag{2.19}$$

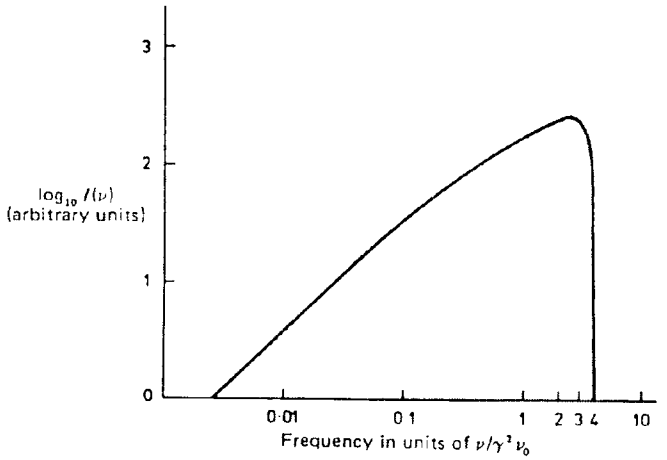

Figure 2.8: The emission spectrum of inverse Compton scattering; ν_0 is the frequency of unscattered radiation (Blumenthal & Gould 1970). Picture taken from Longair (1992a)

The inverse Compton emission is produced by seed photons which are upscattered by electrons or other relativistic particles in the jet (see chapter 3 for a description of jets). The energy of the photons increases by a factor of $\sim \gamma^2$, where γ is the Lorentz factor of the relativistic particle. Consequently there are two crucial factors that determine the nature of the inverse Compton emission: (i) the maximum energy of the jet electrons, which determines the turnover of the synchrotron component and (ii) the typical energy of the seed photons, which is governed by the relative strengths of the thermal and non-thermal components.

2.2 Synchrotron Self-Compton Emission

Synchrotron photons emitted by energetic electrons can undergo inverse Compton scattering from the same set of electrons, acquiring in the process $\sim \gamma^2$ times the energy

Chapter 3

Active Galactic Nuclei

The classification active galactic nucleus (AGN) is used to describe energetic phenomena in the central regions of galaxies which cannot be attributed clearly and directly to stars. AGN can be divided into many subclasses, the main two classes being Seyfert galaxies and quasars. The difference between these two classes relates to the amount of energy emitted by the central source. For a typical Seyfert galaxy the total energy emitted by the nuclear source at visible wavelengths is comparable to the energy emitted by all of the stars in the galaxy (i.e. $\sim 10^{11} L_{\odot}$) whereas in a typical quasar the nuclear source is brighter than the constituent stars by a factor of 100 or more.

One of the most unexpected developments in the field of extragalactic astrophysics was the discovery of a class of AGN which emits γ-rays in excess of 100 MeV. The first of these, the nearby quasar 3C 273, was detected in 1978 with the satellite experiment COS B (Swanenburg et al. 1978). However, it was not until the launch of the EGRET experiment on-board the Compton Gamma Ray Observatory in April 1991 that the detection of extragalactic photons at these energies was confirmed. To date over 60 AGN have been

detected with EGRET in the energy range 100 MeV to 10 GeV (Hartman et al. 1999). In addition six AGN have been detected at energies greater than 300 GeV by ground based imaging atmospheric Cherenkov telescopes (IACTs). Information on emission at these energies imposes significant constraints on the physical processes believed to be at work in AGN. The physical processes responsible for the production of high energy γ-ray emission are currently not certain. These processes will be discussed in chapter 4.

This chapter will outline the subclasses of AGN, the nature of these subclasses and how they are connected.

3.1 The Classification of Active Galactic Nuclei

The classification of these objects is hindered by observational constraints i.e. there is not full coverage of all objects in all wavelengths at all times. Therefore it is likely that there is overlap between the various classes of AGN. Figure 3.1 shows the relationship between some types of AGN.

3.1.1 Seyfert Galaxies

The first optical spectrum of an active galaxy was obtained in 1908 at Lick Observatory by E.A. Fath, who noted the presence of strong emission lines in NGC 1068 (Fath 1908). A higher resolution spectrum, obtained by V.M. Slipher, revealed that the emission lines were similar to those seen in planetary nebulae and that they had widths corresponding to velocity dispersions of hundreds of kilometers per second (Slipher 1917). In 1943, Carl Seyfert was the first to realise that there are several similar galaxies which form a distinct

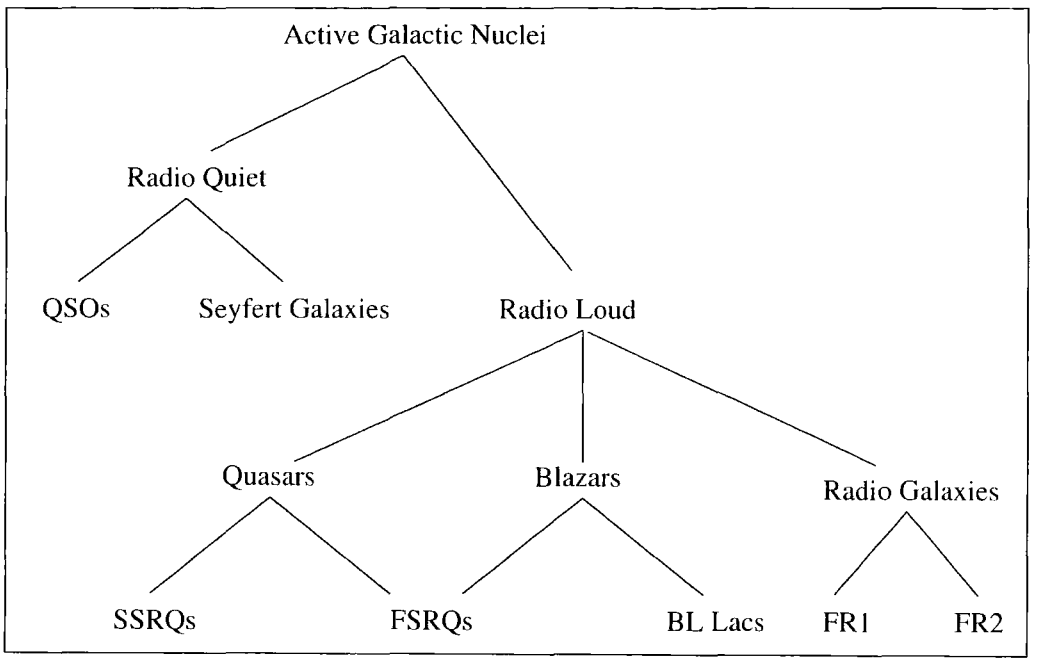

Figure 3.1: This diagram shows the main subclasses of the AGN family.

class. Seyfert selected a group of galaxies on the basis of high central surface brightness i.e. star-like cores. Seyfert obtained spectra of these galaxies and found that the optical spectra of several of these galaxies were dominated by high-excitation nuclear (i.e. nucleus of the AGN) emission lines.

Seyfert galaxies received no further attention until 1955 when NGC 1068 and NGC 1725 were detected as radio sources (Edge et al. 1959).

Seyfert galaxies are relatively low luminosity AGN, with a quasar like nucleus (see section 3.1.2), but with a relatively bright host galaxy. Originally these were defined as galaxies with high surface brightness nuclei and unusual emission line characteristics. However, the definition has evolved so that Seyfert galaxies are now identified by the presence of strong, high ionisation emission lines. Morphological studies indicate that most if not all Seyferts occur in spiral galaxies.

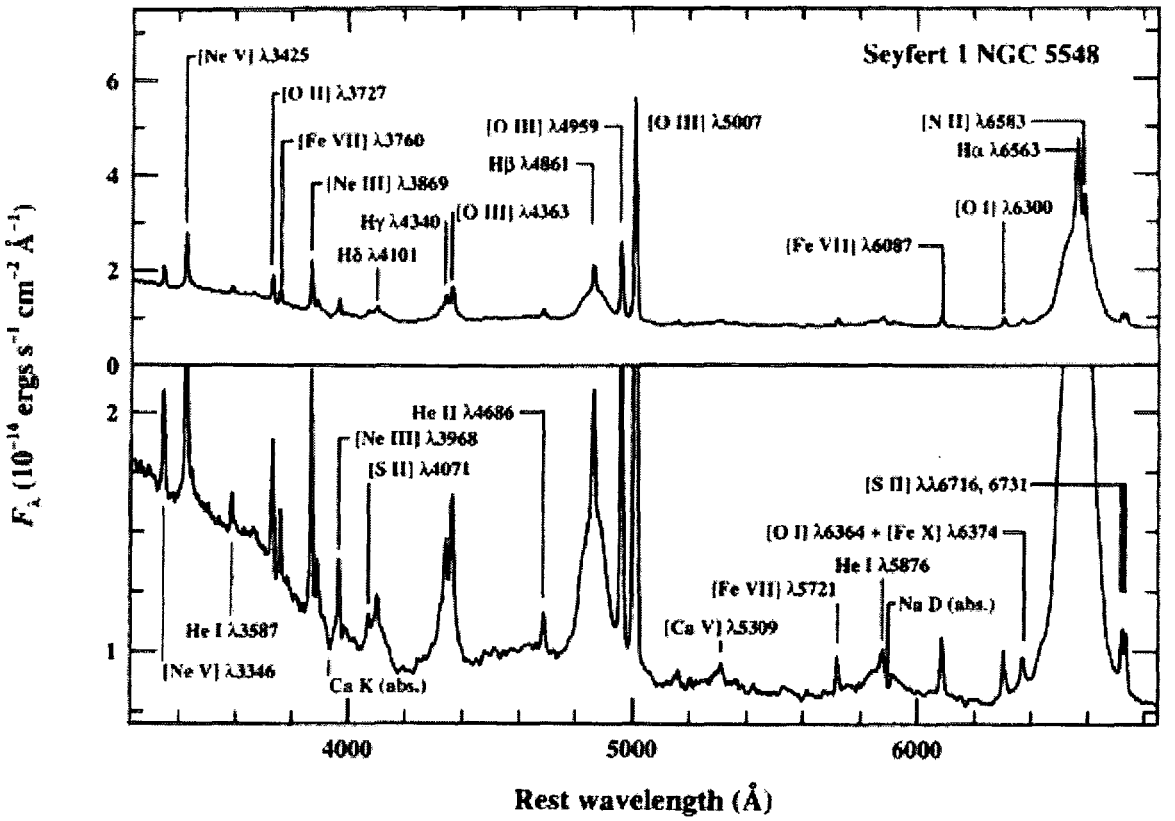

Figure 3.2: The optical spectrum of the Seyfert 1 galaxy NGC 5548. The prominent broad and narrow emission lines are labelled, as are strong absorption features of the host galaxy spectrum. The vertical scale is expanded in the lower panel to show the weaker features. The full width at half maximum (FWHM) of the broad components is about 5900 km s^{-1}, and the width of the narrow components is about 400 km s^{-1}. The strong rise below 4000$\AA$ is the long-wavelength end of the 'small blue bump' feature which is a blend of Balmer continuum and Fe II line emission. This spectrum is the mean of several observations made during 1993 with the 3-m Shane Telescope and Kast spectrograph at the Lick Observatory. (Peterson 1997)

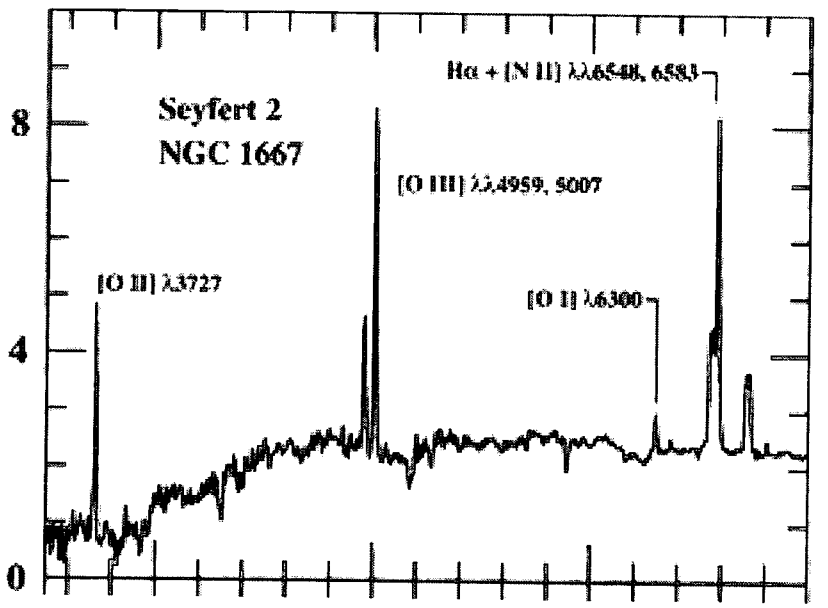

Figure 3.3: The optical spectrum of the Seyfert 2 galaxy NGC 1667 is shown, with important emission lines identified (Ho et al. 1993). This spectrum can be compared with the spectrum shown in Figure 3.2. The units are: Wavelength ($\AA$) for the x-axis and F (ergs s^{-1} cm^{-2} $\AA^{-1}$) for the y-axis (Peterson 1997).

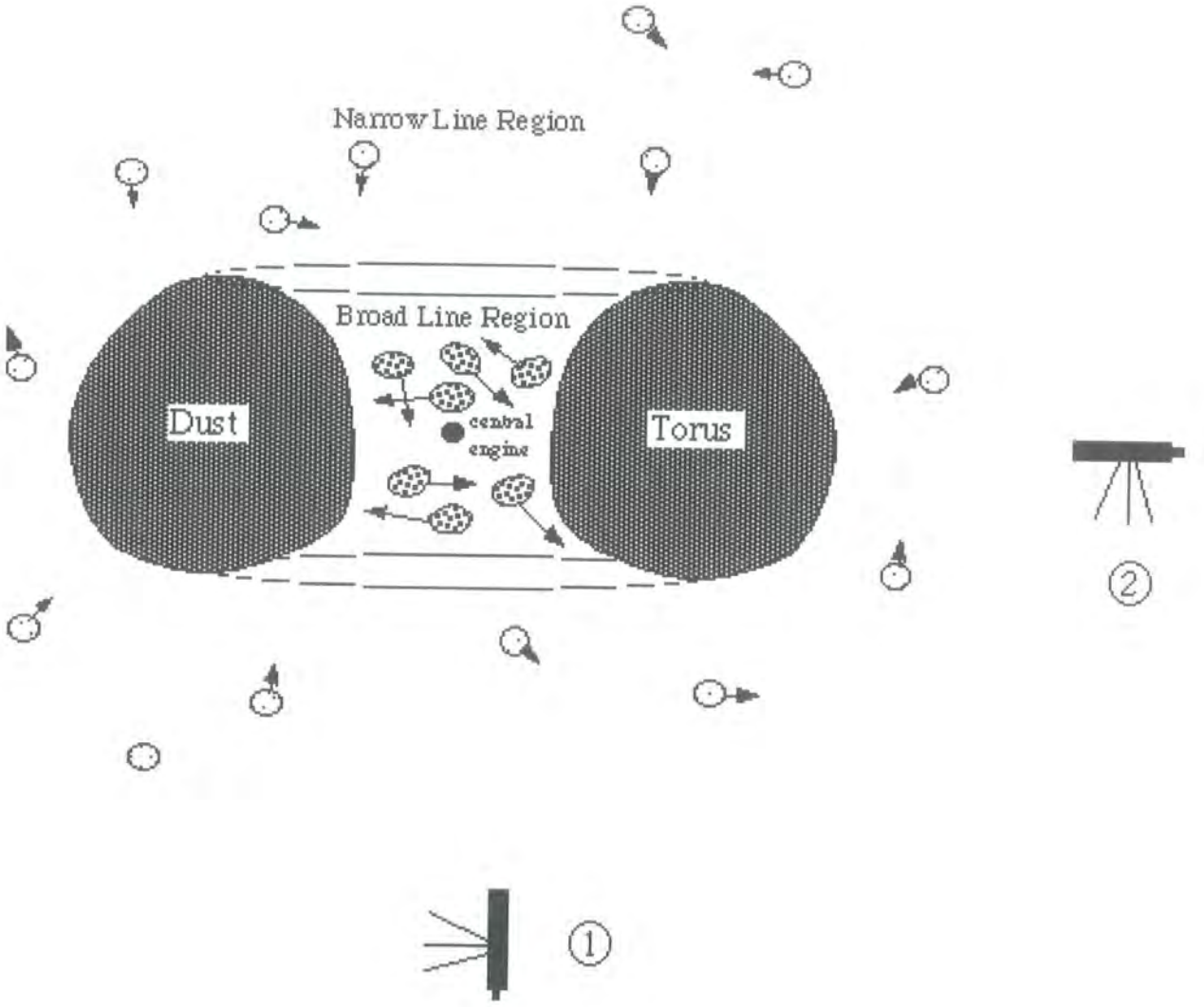

Figure 3.4: The supposed origin of the difference between type I and type II Seyfert galaxies. Viewing angle number one would result in type I spectra while observations from viewing angle number two would result in type II spectra (Merrifield 1995).

all and (b) the narrow lines are generally weaker relative to the broad lines than is the case in Seyfert galaxies. Quasars can be divided into two classes depending on their radio spectra, flat spectrum radio quasars (FSRQs) and steep spectrum radio quasars (SSRQs) with spectral indices below and above 0.5 respectively. Radio quiet quasars are known as QSOs (quasi-stellar objects).

3.1.3 Radio Galaxies

Strong radio sources are typically identified with giant elliptical galaxies, although some of the brightest radio sources are associated with quasars. Two types of radio galaxies have optical spectra of the sort we identify with AGN activity; broad line radio galaxies (BLRGs) and narrow-line radio galaxies (NLRGs) are the radio-loud analogues of type I and type II Seyfert galaxies, respectively. One important difference is that they appear to occur in elliptical galaxies rather than spirals.

Extended radio structures can be divided into two separate luminosity classes (Fanaroff & Riley 1974). Class 1 (FR I) sources are weaker radio sources which are brightest in the centre with decreasing surface brightness towards the edges. In contrast, the more luminous FR II sources are limb brightened and often show regions of enhanced emission either at the edge of the radio structure or embedded within some part the structure other than the centre.

3.1.4 Blazars

In general, AGN show continuum variability at all wavelengths at which they have been observed, from X-ray to radio. A small subset of AGN show short time-scale variations

that are abnormally large, e.g. $\Delta m \gtrsim 0.1$ mag, at visible wavelengths on time scales as short as a day. They also tend to have high polarisation (up to a few percent as opposed to less than one per cent for most AGN) which also varies in both magnitude and position angle. In addition these sources are always radio loud. These are known as optically violent variables (OVVs).

Some of the properties of OVVs, including the radio emission, are shared by BL Lac objects. These are named after the prototype of the class, BL Lacertae, which was originally identified as a highly variable star. BL Lac objects are distinguished by the absence of strong emission or absorption lines in their spectra.

It is thought that both OVVs and BL Lacs are those AGN that have a strong relativistically beamed component close to the line of sight. Collectively OVVs and BL Lacs are sometimes referred to as blazars. Nilsson et al. (1999) found that blazar host galaxies are large (effective radii of $7 - 40$ kpc) and bright (absolute magnitude, $M_R = -23.2$ to -24.6) elliptical galaxies whose surface brightness can be described by a single power law $I(r) \propto r^{-\beta}$ with $\beta = 0.10 - 0.36$ to an accuracy of 0.2 mag. There are found to be two sub classes of blazars. High Frequency-peaked BL Lacs (HBLs) and Low frequency peaked BL Lacs (LBLs) as characterised by their spectral energy distributions (SEDs). Their SEDs will be described in more detail in chapters 7 and 8. Blazars are the only sub class of AGN that have been detected at TeV energies.

3.2 The AGN Paradigm

The unified model attempts to explain different types of active galaxies as being different views of one type of object. See figure 3.5.

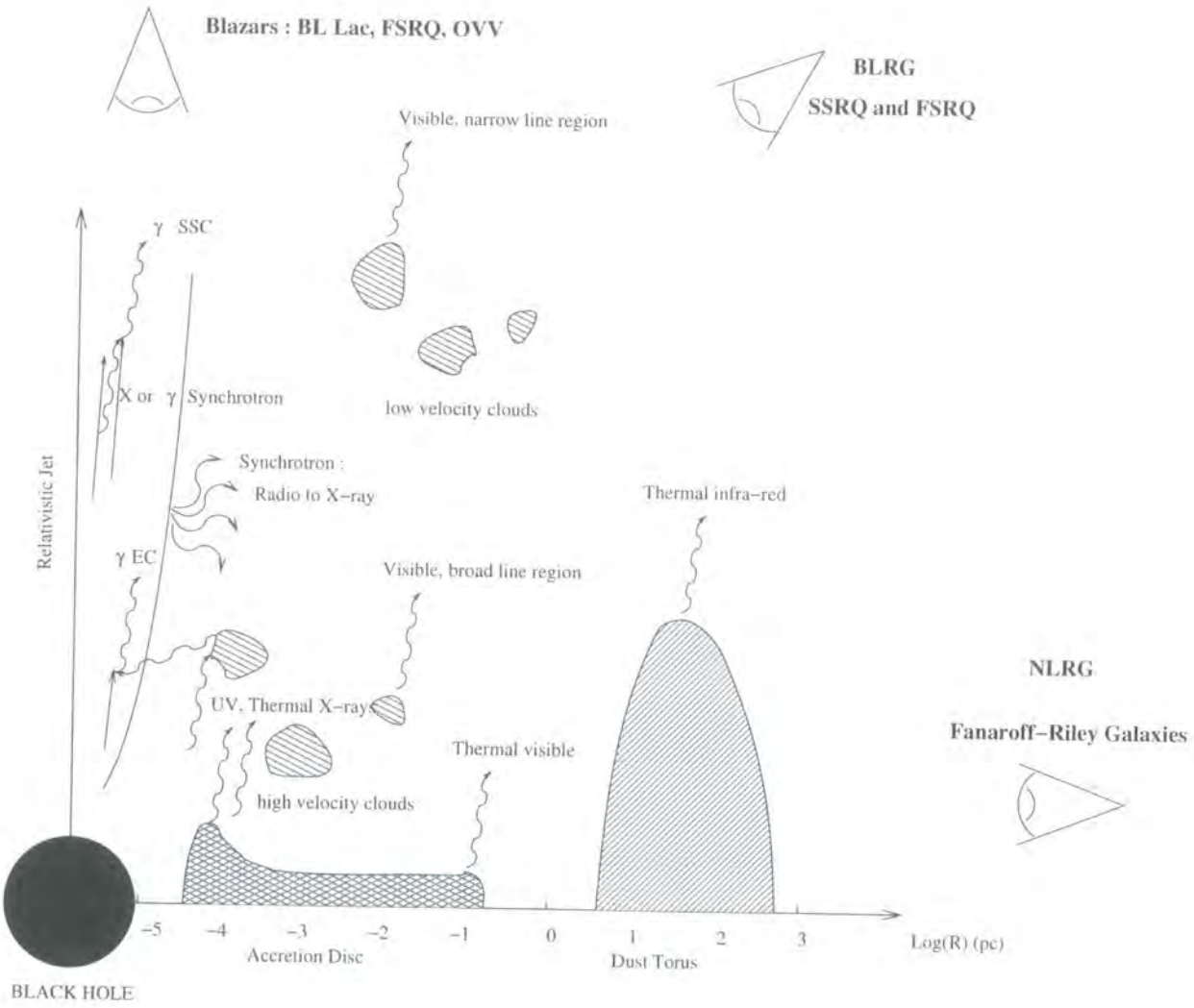

Figure 3.5: The Unified Model: dependency of AGN class on viewing angle.

The fundamental question about AGN is how the energy that is detected as radiation is generated. The problem is that an AGN produces as much energy as up to several trillion stars in a volume that is significantly smaller than a cubic parsec. Further to the

Seyfert galaxy paradigm outlined in section 3.1.1, the current working model for the AGN consists of a 'central engine' comprised of a hot accretion disc surrounding a supermassive black hole. Energy is generated by gravitational in-fall of material which is heated to high temperatures in a dissipative accretion disc. The physical arguments which underly this view are very basic and date back at least as far as Zel'dolvich & Novikov (1964) and Salpeter (1964).

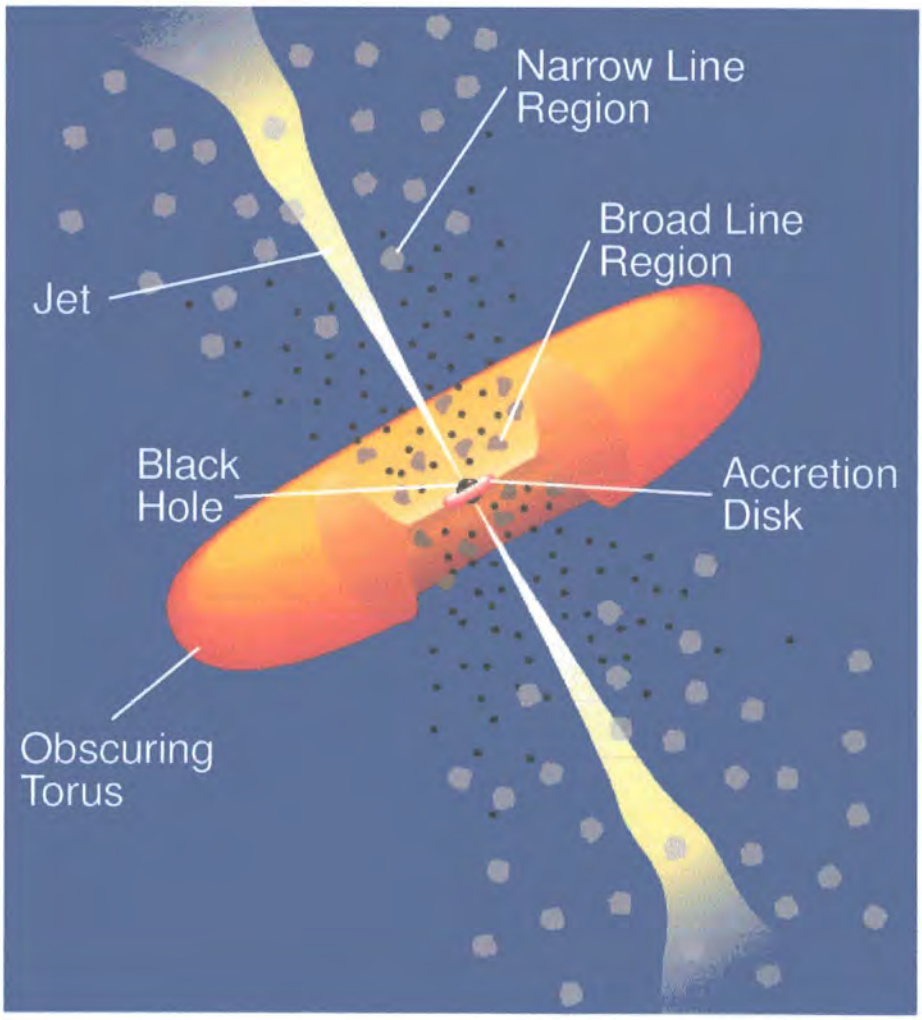

Figure 3.6: Schematic diagram of an AGN (Urry & Padovani 1995).

The nuclear activity is powered by a supermassive ($10^6 - 10^9 M_\odot$) black hole and its

accretion disc, which extends to $\sim$ 1pc. This central engine is surrounded by a dusty toroidal structure, extending to $\geq\sim$ 100pc. The torus provides anisotropic obscuration of the central region so that sources viewed face-on are recognised as type I Seyfert galaxies, those observed edge-on are type II Seyferts (see figure 3.4). The primary evidence for the torus comes from spectropolarimetric observation of type II sources which reveal hidden type I emission via reflection off material situated above the torus opening (e.g. Miller & Goodrich 1990). While compelling, this evidence is indirect in that it involves obscuration and not direct emission by the torus itself. The optical and UV emission lines are produced in moving clouds of gas. The radiation along some lines of sight is obscured by a torus or warped disc of gas and dust. Outflows of energetic particles occur along the poles of the disc or torus escaping to form collimated radio-emitting jets. It is generally believed that radio quiet AGN do not possess jets.

3.2.1 Accretion Discs

In theoretical models, an accretion disc is believed to form when gas with angular momentum is accreted onto the black hole. According to Kepler's third law the inner regions of this accretion disc would orbit the black hole more rapidly than would the outer parts. Thus, the rapidly spinning inner regions would constantly rub against the slower moving gases in the outer regions. This friction would cause the gases to lose energy and spiral inward towards the black hole. As the gases move inward within the accretion disc, they are compressed and heated to very high temperature. This causes the accretion disc to glow thus producing the brilliant luminosity of an AGN. Any variations in the density of the gas will cause the luminosity to fluctuate giving rise to the brightness variations

observed. Accretion discs are identified as a source of continuum emission which can be directly observed. They also maintain the ionisation in the emission line clouds. They are believed to be the sources of mass and spin responsible for fuelling the jets.

There are two types of accretion disc; thick and thin. A thick disc is one that has thickness comparable to its radius, a thin disc is one with thickness much less than its radius. Accretion on to the black hole need not result in the formation of a thin disc. If the infalling gas is unable to cool effectively the inner accretion disc may become geometrically thick and toroidal. This can happen at high accretion rates when a radiation supported torus will be formed (Wiita 1982) or at low accretion rates with large effective viscosity when the ions may be unable to cool and an ion supported torus will be formed (Rees et al. 1982).

The detailed structure of the accretion disc depends on a variety of parameters such as the magnetic field strength, the accretion rate and the presence or absence of a disc corona or jets. Balbus & Hawley (1991) show that accretion disks are subject to a very powerful shearing instability mediated by a weak magnetic field of any reasonable astrophysical strength. They suggest that this instability can help to understand the origin of turbulent viscosity in accretion disks.

3.2.2 Jets

Due to the constant inward crowding of hot gases, pressures climb rapidly in the inner accretion disc. To relieve this congestion matter is expelled along the inner edges of an empty funnel-shaped cavity. This results in two broad, oppositely directed beams of relativistic particles that flow at right angles to the accretion disc (e.g. Sauty et al. 2002).

Magnetic forces play a crucial role in steering these fast-moving particles. These forces arise because the hot gases in the accretion disc are ionised, forming a plasma, and the motion of this plasma generates a magnetic field. As the plasma in the disc rotates around the black hole it pulls the magnetic field along with it, but because the disc rotates faster in its inner region than at its outer rim the magnetic field becomes severely twisted. This twisted field forms two helix shapes on either side of the plane of the disc. Relativistic particles flowing outward from the accretion disc tend to follow these magnetic field lines. The result is that the outflowing beams of particles are focused into two jets oriented perpendicular to the plane of the accretion disc. The characteristic feature of a strong radio galaxy is a double structure: two large radio emitting regions on opposite sides of the observed galaxy, known as radio lobes. An example of a such a galaxy may be seen in figure 3.7.

It is currently assumed that jets are produced close to the central black hole, involving power extraction from the black hole spin (Blandford & Znajek 1977) and/or from the accretion disc (Blandford & Payne 1982). In both scenarios the magnetic field must play a major role in channelling power from black hole or from the disc into the jet; in both cases it should be sustained by matter accreting onto the black hole.

A narrow jet may supply energy and/or material to the radio lobes (e.g. Blandford & Rees 1974). It seems that much of the non-thermal emission seen at higher frequencies may be produced by jets. Their emission, from radio to gamma ray, is dominated by the beamed non-thermal continuum produced in the jet (Urry & Padovani 1995). This is because of relativistic beaming along the jet; gas flowing at relativistic velocities will direct its emission preferentially along its direction of motion, synchrotron self-Compton

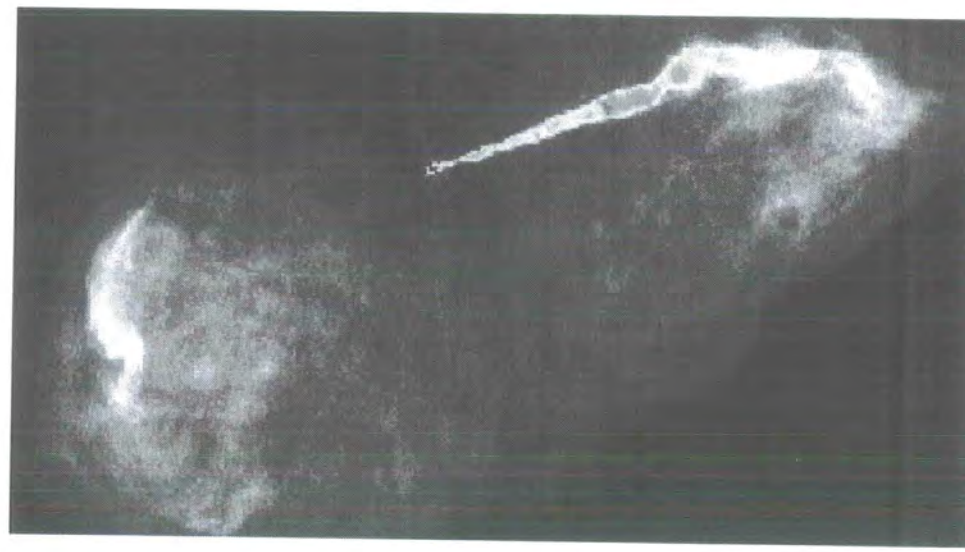

Figure 3.7: Radio image of NGC 9943, showing the two radio lobes (one in the upper right and one in the lower left of the image), a jet and the central source (which is embedded in a host galaxy which is quite small on this scale). The jets are of the order of Mpc in length. Taken from (Flynn 2004).

scattering and the doppler effect. Jets cannot be considered in isolation from discs; they appear to be a natural by product of the formation of a disc.

3.3 Host Galaxies

The study of the host galaxies of AGN has some intrinsic problems associated with it; the AGN's luminosity dominates that from the host galaxy and makes it difficult to identify or classify the host galaxy.

However, there is a consensus based on many different imaging studies that radio-quiet QSOs and Seyfert galaxies tend to be found in disc systems and radio-loud QSOs and BLRGs tend to be found in elliptical galaxies (Hutchings et al. 1989).

All the currently TeV detected blazars are found to be in elliptical galaxies. Falomo et al. (2000) looked at a sample of 30 BL Lacs with $0.03 < z < 0.2$. All the galaxies had characteristics very similar to those of "normal" giant ellipticals. The luminosity, ellipticity, isophote twisting, and amount of 'discy' or 'boxy'* isophotes are consistent with those found in non-active ellipticals and in radio galaxies suggesting that tidal interactions are very infrequent or are short-lived with respect to the nuclear activity. In addition there is no indication of displacement and/or off-centering of the galaxy isophotes with respect to the nucleus, meaning that the unresolved nuclear source truly sits in the centre of the galaxy.

Falomo et al. (2000) searched for faint substructure in the host galaxies, but did not

*This relates to the shape of the isophotes. They can be elliptical in shape to quite rectangular in shape.

reveal notable signatures of tidal distortions or subcomponents (faint discs, bars, etc) and, with only one exception, found no prominent dusty features in the central regions. Instead the BL Lac host galaxies are smooth and unperturbed suggesting that strong external gravitational interactions are not important to ongoing activity. A careful examination of the environment around the nucleus showed a high incidence of close companion (see section 3.3.2) objects whose nature remains unclear pending spectroscopic observations. Falomo et al. (2000) state that galaxies hosting BL Lac objects are rather smooth and unperturbed but that faint substructures could be hidden by the smooth contribution of the stellar component. They constructed a 2-D model of the galaxy using the best-fit parameters from the surface photometry analysis. Using this they were able to see jets in PKS 0521-36, 3C 371 and PKS2201+044. 1ES 0806+52.4 showed arclike emission at $\sim 2''$ from the nucleus, which could be a shell around the galaxy, a feature not uncommon among ellipticals. No other faint structures (shells, bars, or X-shaped features) were detected in the observed sources.

3.3.1 Dust

HST observations of nearby radio galaxies have shown that dusty features are present in the central regions of most of the observed objects (Falomo et al. 2000). These features often take the form of discs or lanes but sometimes the distribution is irregular. The observed dust pattern is generally confined within a region typically less than 1.5 kpc (in most cases the physical sizes of discs and lanes range from 0.3 to 1.5 kpc).

Since BL Lac objects are believed to be radio galaxies with their jet pointing towards us, we should observe similar dusty features also in these objects. However, the bright

nucleus tends to outshine the central region of the host galaxy. Also the average distance of the objects studied by Falomo et al. (2000) was larger than that of comparison samples of radio galaxies observed with HST, making the angular size of dusty features smaller. This lack of detection suggests that the relevance of dusty features may be different in BL Lac objects and radio galaxies with the caveat of the small statistics considered (Falomo et al. 2000).

3.3.2 Companion Galaxies

It is believed that the large-scale (Mpc) environment around AGN might provide important clues regarding the physical conditions that may lead to the AGN activity. The presence of interacting companions may be a factor, as AGN are more likely than other galaxies to have companion systems; the term 'companion' is taken to mean a galaxy which is close enough that the systems may interact gravitationally although it does not necessarily mean that the systems are gravitationally bound. Dahari (1984) found that 15% of Seyfert galaxies have companions whereas only 3% of a control sample of normal galaxies had such companions. This result was confirmed by MacKenty et al. (1990) with a larger and better defined sample. The companion galaxies themselves do not appear to be in any way affected by the presence of the AGN as they do not seem to be unusually luminous (Yee 1987); conclusions about their colours are less definitive.

The high incidence of morphological peculiarities and of close companions is indeed suggestive that interaction with other systems can plausibly trigger AGN activity. However, neither close companions nor disturbed morphology provide either necessary or sufficient conditions for producing AGN. For example strongly interacting systems (such

as those studied by Arp) tend not to show AGN phenomena and some AGN are quite isolated with no obvious companion systems.

Again Falomo et al. (2000) have carried out a statistical study on BL Lac objects and the presence of companions. Although their sample was small they conclude that the association between BL Lac objects and companions is not dominated by chance alignments. However, the role of these companions is not clear. In other BL Lac fields, optical spectroscopy of the companion has sometimes proved the physical association with the active galaxy (Falomo 1996).

Some of the close companions are resolved faint galaxies with absolute magnitudes (assuming they are at the distance of the BL Lac object) in the range $-21 < M_R < -19$ mag. This is consistent with previous evidence that BL Lac objects inhabit environments with higher than average galaxy densities, as in groups or poor clusters. Spectroscopy of the companions is needed to determine their nature.

However, there is little evidence of tidal interaction in the BL Lac host galaxy (appreciable isophote twisting, non-concentric isophotes, etc.), which suggests that the companions are not strongly perturbing it. Gravitational interactions might have had a greater role in the past in the formation and fuelling of the active nucleus and what we see now could be a left over of an earlier (close) interaction. One possibility suggested by numerical simulations (e.g. Bekki 1999) is that the close companions are the product of a past major merger between gas-rich galaxies and also provide fuel for the nuclear activity but are not necessarily linked to the formation of a massive black hole in the nucleus or to the sustenance of an active relativistic jet.

There is no evidence of a connection between the host galaxy properties and the nuclear

properties in BL Lacs (although this has not been thoroughly studied yet). Many BL Lacs appear to have close companion galaxies but in most cases there is no spectroscopic evidence of their physical association. In some cases clear signs of interaction between the BL Lac host and its companion(s) are observed: the host appears distorted or there is a bridge of material connecting it to the companion (e.g. 3C 371: (Stickel et al. 1993); 1ES 1440+122: (Heidt et al. 1999)).

Chapter 4

Models of TeV Gamma Ray Emission From Blazars

AGN jets, if originating near the black hole, are expected to undergo strong Compton interactions with the surrounding dense radiation fields. In particular, electrons travelling in a jet together with protons at bulk Lorentz factors $\Gamma \sim 10$, (typical value inferred from VLBI measurements Vermeulen & Cohen 1994) are expected to produce strong beamed soft X-ray radiation, resulting from scattering off the 'UV bump' produced by the accretion disk (Begelman & Sikora 1987). As a result, the spectra of blazars should show prominent soft X-ray bumps/excesses. These are not observed, suggesting that at least in quasars, where UV radiation fields are very dense, the jets must be accelerated, collimated and/or mass loaded over a much larger distance range than the size of the central engine (Levinson 1996).

Highly polarised and variable infrared and optical radiation is successfully interpreted in terms of Doppler-boosted synchrotron radiation (Blandford & Rees 1978, Blandford &

Konigl 1979), while the most plausible mechanism of the gamma ray production seems to be Compton upscattering of lower energy photons; both processes are most likely due to electrons with random relativistic energies ranging up to $10^3 - 10^5 m_e c^2$. Since the timescales of radiative energy losses of such electrons are very short compared to both synchrotron and Compton processes the electrons must be accelerated in situ, i.e. in the regions where they produce radiation. There have been many models put forward in an attempt to explain the high-energy gamma ray emission from blazars. So far, none has managed to uniquely explain the dominant mechanism responsible for the high energy emission. In this chapter the most promising and favoured models will be described.

4.1 Observational Constraints

Models of blazars must be able to explain the observed properties of blazars, to include the following:

- The source should be transparent to high energy gamma rays. Radiation from particles in the jet must be beamed so that it is not absorbed via pair production close to the source (e.g. Mattox et al. 1993, von Montigny et al. 1995, Dondi & Ghisellini 1995).

- Rapid variability of emission places restrictions on the size of the emitting region. If it were too compact or close to the accretion disc and its corona, gamma rays would not survive absorption via pair production. If it were too large the emission could not vary sufficiently rapidly (Ghisellini & Madau 1996). In the case of Mrk 421, the TeV flux has been observed to vary within a 20 minute timescale (Gaidos et

al. 1996).

- Time lags have been observed, for example between soft and medium X-ray emission. These strongly suggest a leptonic origin of the emission, placing restrictions on the physical parameters of the emitting region (e.g. Dondi & Ghisellini 1995).

- The simultaneity of variation of gamma rays and some other wavelength bands suggests that the gamma rays originate in the same parts of the jets as these other strongly variable components (e.g. Georganopoulos & Marsher 1998).

The simplest model proposed for TeV blazars involves a single zone and a single population of the relativistic electrons emitting synchrotron radiation from radio to X-rays and inverse Compton radiation from X-rays to gamma rays. Models of the high energy emission can be divided into two broad classes.

The first class assumes that the bulk motion of particles in the jet and or electromagnetic energy is converted directly into the internal energy of relativistic electrons with a non-thermal distribution. These electrons emit synchrotron radiation and inverse Compton scatter low energy seed photons to higher energies, resulting in the low and high energy 'humps' of the characteristic blazar SED, respectively. This class can be further subdivided into synchrotron self-Compton (SSC) and external Compton (EC) models. In SSC models the seed photons are the synchrotron photons themselves while in the EC model the seed photons are produced externally to the jet. Examples of potential sources of external photons include isotropised nuclear radiation, broad line photons (Sikora, Begelman & Rees 1994), photons from an accretion disc (Dermer & Schlickeiser 1993) and photons from a dusty torus (Sikora & Madejski 2000).

In the second class of models it is instead believed that energy is mainly stored in hadrons which is subsequently transferred, through particle-particle or particle-photon interactions, to a population of leptons. The two components of the SED in these cases would be mostly synchrotron radiation from primary leptons or protons and secondary leptons or protons, respectively (Mannheim 1993, Protheroe 2001, Aharonian 2000).

4.2 Leptonic Models

4.2.1 Synchrotron Self-Compton Models

SSC models were originally suggested by Ginzburg & Syrovatskii (1969) and developed in detail for spherical homogeneous sources by Rees (1967) and Jones et al. (1974). These models were later incorporated into the relativistic jet scenario (e.g. Königl 1981, Marscher & Gear 1985, Ghisellini & Maraschi 1989, Ghisellini & Maraschi 1996, Mastichiadis & Kirk 1997, Sikora 1997). SSC models have the elegant feature that the synchrotron photons are both produced and comptonised by the same population of relativistic electrons. However, fitting an SSC model to observed blazar spectra is non-trivial (e.g. Maraschi et al. 1992). In SSC models, the relativistic plasma producing non-thermal radiation is constrained to be very weakly magnetised ($B \lesssim 10^{-2}$ Gauss) and located at very large distances ($r \sim 10^{19}$ cm). These can impose problems with jet confinement and with the short observed timescale of variability (Sikora et al. 1997).

For the inverse Compton emission to dominate over the synchrotron radiation, the radiation energy density in the soft photons has to dominate over the magnetic field energy density. The Poynting flux in the jet is insufficient to provide for the energy lost

in the radiation and it is necessary to depend on the bulk kinetic energy of the jet, thus slowing it down as it progresses. This is not consistent with the initial assumptions of the model (Sikora 1994).

There have been many papers published in support of the SSC model for high energy emission from blazars (Ghisellini & Maraschi 1996, Mastichiadis & Kirk 1997, Sikora 1997).

The synchrotron self-Compton model makes two simple predictions in the homogeneous case (Jones et al. 1974) and in some inhomogeneous cases (Marscher 1977, Ghisellini et al. 1985): (1) the continuum emission of the seed photons and of the Compton emission should be similar, and (2) the flux of seed photons should vary in concert with the Compton emission (Bregman et al. 1990).

Figure 4.1 show a schematic picture of an SED of a typical blazar, where the high energy emission results from SSC processes.

4.2.2 Evidence Regarding the Synchrotron Self-Compton Model

Tavecchio et al. (1998) used shape and variability observations to constrain a homogeneous SSC model. It was concluded that in principle, knowledge of the frequency and luminosity relating to the peak in the synchrotron and inverse Compton humps in the SED would allow the determination of the magnetic field, Doppler factor, radius of the emitting region, Lorentz factor of the electrons at the energy break and the electron density parameter. Tavecchio et al.'s (1998) model assumed:

- The relativistic electron spectrum is a broken power law, in which the break energy

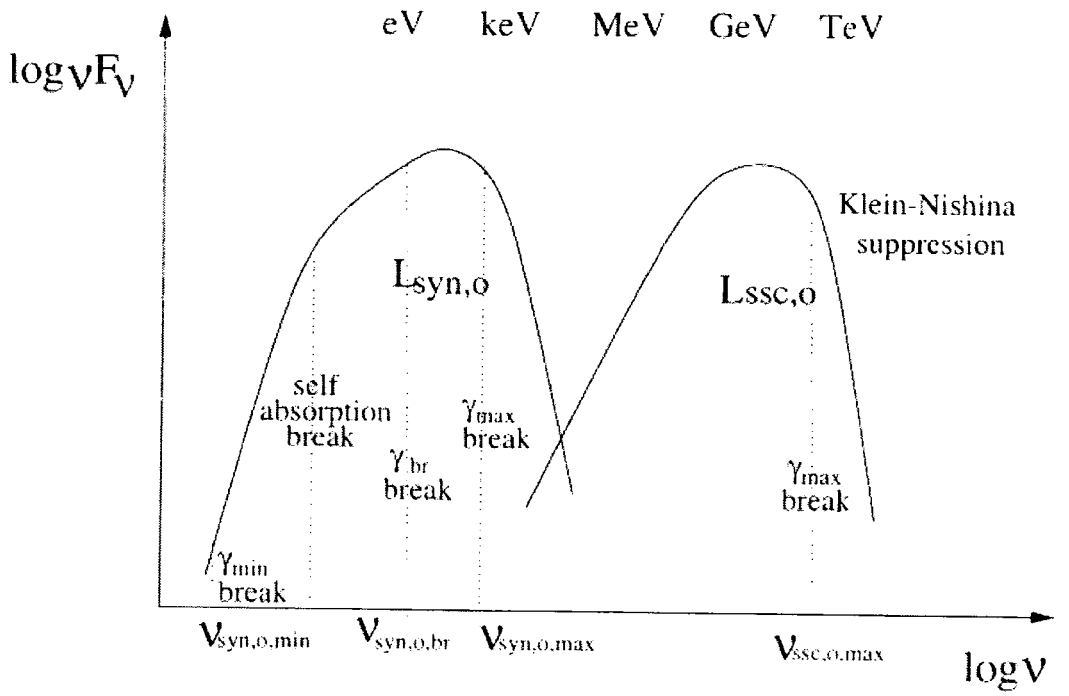

Figure 4.1: A schematic picture of the multifrequency spectrum of a typical TeV blazar. Here $L_{\rm syn,o}$ and $L_{\rm SSC,o}$ are the observed bolometric luminosities of the synchrotron and SSC components, respectively. Corresponding to the break in the relativistic electron energy spectrum in the emission region, a break feature appears in the observed synchrotron spectrum. Around the TeV energy region, the Klein-Nishina effect suppresses the observed flux compared to the Thomson regime. (Kino et al. 2002)

is a free parameter.

- An approximate analytic formula for the case of Compton scattering occurring in the Klein-Nishina regime.

- Restrictions in the parameter space with the break energy resulting from a balance between cooling and escape and that the soft photon lags measured in some sources derive from radiative cooling of high-energy particles.

This model was applied to Mrk 421 and PKS 2155–304. At the time of writing PKS 2155–304 was well observed in the low-energy bands and had been detected on two occasions with EGRET in soft gamma rays. Tavecchio et al. (1998) estimated that the peak of the Compton component should fall at about 10^{25} Hz. After the paper was accepted the detection of PKS 2155–304 by the Durham Group. (Chadwick et al. 1999), was published and was consistent with their estimate. This result will be discussed in more detail in chapter 7.

Although the model could describe Mrk 421 and PKS 2155–304, it was unable to sensibly describe the high luminosity state of Mrk 501 as the required value of the Lorentz factor at the energy break was inconsistent with cooling-escape equilibrium, indicating the need for an efficient continuous reacceleration mechanism.

In 1997, Mrk 501 was observed by the Whipple observatory and found to be in a flare state (Catanese et al. 1997). The average gamma-ray flux above $\sim$ 350 GeV in the 1997 observing season rose to 1.4 times that of the Crab Nebula, 14 times the 1995 discovery level ($8.1 \pm 1.4 \times 10^{-12}$cm^{-2} s^{-1} above 300 GeV Quinn et al. (1996)). Significant hour-scale variability was present in the 1997 data, with the shortest having a doubling time

of $\sim$ 2 hours (Quinn et al. 1999).

Krawczynski et al. (2002) used an SSC model to describe the Mrk 501 1997 flare. They showed that a simple two-component model (with a soft, steady X-ray component plus a variable SSC component) involving substantial pre-acceleration of electrons to Lorentz factors of the order of $\gamma_{min} = 10^5$ could describe the data.

Kino et al. (2002) used a one zone synchrotron Compton model to describe the emission from PKS 2155–304 and found a satisfactory fit using the parameters outlined in figure 4.2.

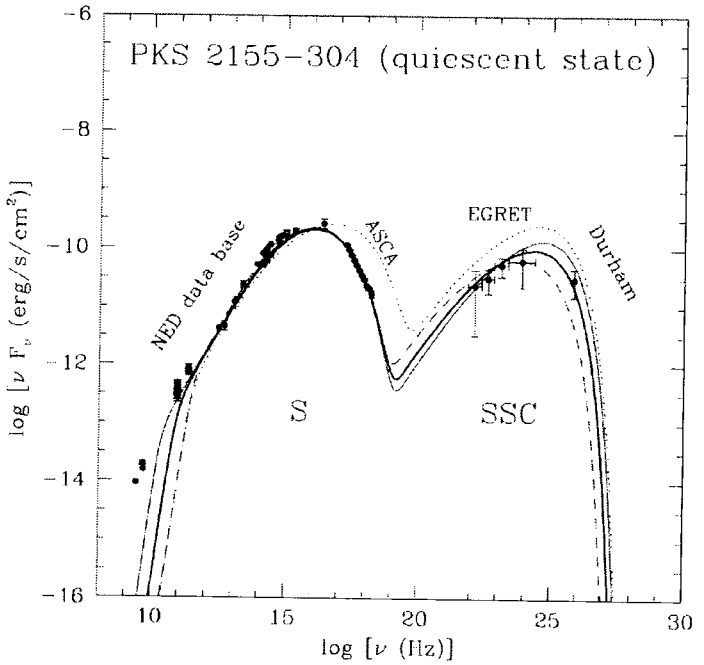

Figure 4.2: The one zone SSC model spectra for the steady state emission of PKS 2155–304. The thick solid line shows the best-fit spectrum where the adopted parameters are $\delta = 33$, $R = 9.0 \times 10^{15}$cm, $B = 0.30G$, $\gamma_{max} = 0.5 \times 10^5$, the injection rate of electrons, $q_e = 2.8 \times 10^{-5}\mathrm{cm}^{-3}\mathrm{s}^{-1}$, the power law index of injected electrons $s = 1.4$, and $u_e/u_B = 3$. The dotted line shows the spectrum obtained using the analytic estimates for PKS 2155–304. The thick solid and dashed lines show the spectra of low and high injection models respectively, to indicate the uncertainty range of the spectral fitting (Kino et al. 2002)

4.2.3 External Compton Models

In EC models, the most natural source of seed photons is radiation from the central accretion flow, some of which is scattered or reprocessed by material in the region through which the jet is passing, as illustrated in figure 4.3.

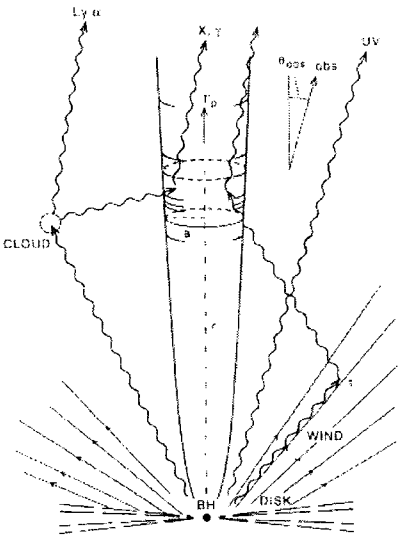

Figure 4.3: Schematic geometry of the source. The radiating region, denoted by the short cylinder of dimension a, moves along the jet with pattern Lorentz factor Γ_p. Underlying flow moves with Lorentz factor Γ, which may be different from Γ_p (Sikora, Begelman & Rees 1994).

Depending on the details of geometry and kinematics, the Compton interaction will be dominated by either the direct radiation field or the diffuse reprocessed radiation field. Begelman & Sikora (1987) first pointed out that Compton scattering of ambient radiation by a cold relativistic jet could reproduce many of the distinctive features of blazar radiation such as large rapidly variable polarisations. This production mechanism with modest bulk Lorentz factors ($\sim$ 10, similar to those inferred from radio observations of superluminal motion), provided that the radiating electrons have ultra-relativistic random energies in

the fluid frame of the jet (e.g. Dermer et al. 1992), could reproduce these features.

Dermer et al. (1992) suggested that external photons for Compton scattering by the relativistic electrons in the jet could be provided by direct radiation from the accretion disc. The production of gamma rays from the process would have to take place at distances $> 10^{17}$ cm from the nucleus so that the gamma rays would not be absorbed via pair production with soft photons (Maraschi et al. 1992). In the jet frame, photons from the disc appear to be highly redshifted while the photons that are scattered and form a diffuse field are blueshifted. The upscattering of the diffuse field photons therefore becomes the dominant process.

Sikora, Begelman & Rees (1994) stated that on sub-parsec scales, the jet of a blazar will be pervaded by radiation from the broad line region as well as by photons from the central continuum source (some of which will be scattered by thermal plasma). In a frame moving with the relativistic outflow, the energy of this ambient radiation would be enhanced. This radiation would be inverse Compton scattered by both cold and relativistic electrons (in the frame moving with the relativistic outflow) in the jet, yielding (in the observer's frame) a collimated beam of X-rays and gamma rays.

The spectral break between the X-ray and gamma ray band observed in 3C 279 and deduced for other blazars, would result from inefficient radiative cooling of lower energy electrons. Sikora, Begelman & Rees (1994) suggested that the existence of such a break strongly favours an EC model over a SSC model.

In order for Compton scattering of external radiation to dominate over SSC emission the energy density of the external radiation as measured in the frame comoving with the jet must exceed the energy density of synchrotron radiation produced in the jet. It is

difficult to satisfy this condition by considering only direct radiation from the central source, as was originally proposed by Dermer et al. (1993). In order for this radiation to dominate over the local synchrotron radiation field, extremely weak magnetic fields are required.

To deal with this problem, Blandford (1993) and Sikora, Begelman & Rees (1993), proposed that the dominant contribution to the energy density as measured in the co-moving frame of the radiating plasma comes from scattered or reprocessed portions of the central source radiation rather than from the direct radiation of the central source. A diffuse radiation field at large distances from the central source can be produced by scattering off a hot accretion disc wind, by reprocessing in the clouds producing broad emission lines, and by absorption and thermal re-radiation of dust. Measured in the frame of a relativistic jet passing through the region of reprocessing, this radiation is strongly blueshifted. Sikora, Begelman & Rees (1994) showed that such a scenario can explain all basic features of 3C 279 spectrum within a "one-zone" model i.e. in the sense that both the IR to UV and X-ray to gamma ray portions of the blazar spectrum are produced within the same region of the flow, by the same population of particles.

4.2.4 Evidence Supporting the External Compton Model

According to Dondi & Ghisellini (1995), the good $L_\gamma - L_{IR}$ correlation, based on EGRET detected objects at $E > 100$ MeV, indicates that the gamma rays cannot be less collimated than the radio emission. It also indicates that the radio synchrotron emission is produced by the same relativistic electrons that produce gamma ray emission by inverse Compton scattering of the radiation from hot circumnuclear dust.

Xie et al. (1997) examined a set of 16 blazars, all well observed in the near-IR and with soft gamma ray flux densities. A strong correlation between the near-IR and the gamma ray flux densities was found. As a result of this correlation, they surmised that there must be a relation between the gamma ray production and the near-IR sources. This in turn would impose constraints on any emission models for gamma ray loud blazars reinforcing the idea that gamma ray flares are created by inverse Compton scattering of the radiation from hot circumnuclear dust by a relativistic electron beam.

According to Sikora, Begelman & Rees (1994), the greatest obstacle to modelling Mrk 421 with an EC model is the photon-photon pair production opacity due to the diffuse radiation field which surrounds the jet. This constraint can probably be overcome if the seed photons come from thermal IR emission by dust rather than the UV photons. To date very few BL Lac objects show evidence for thermal radiation by dust or a thermal UV excess, however, the presence of diffuse IR radiation in BL Lac cannot be be ruled out. An additional advantage of producing the TeV radiation by Comptonising IR photons is that the scattering takes place entirely in the Thomson regime ($\Gamma\gamma E_{ext} < m_e c^2$), thus avoiding the depression in the spectrum associated with the Klein-Nishina regime.

4.3 Differences Between SSC and EC Models

From the measured luminosities and energies of the spectral peaks of the low-energy (synchrotron) and the high-energy (Compton) components, it is possible to estimate Poynting fluxes and magnetic field intensities and then distances at which most of the non-thermal radiation is produced as well as the maximum content of electron positron pairs in the

jets. It was shown that these results are dramatically different for SSC and EC models (Sikora et al. 1997).

Additional constraints on the relative importance of various radiation models can be obtained from the X-ray spectra and from the change of the spectral slope in the vicinity of the MeV peaks. The average energy index of X-ray spectra in FSRQ is $\alpha \simeq 0.7$ (Worrall & Wilkes 1990, McNaron-Brown et al. 1995). As was pointed out by Ghisellini & Madau (1996), such hard spectra cannot be reproduced by EC models with pair cascades. With regard to the MeV spectral break, in most cases the slope change is $\Delta\alpha \leq 0.5$ which can be explained by an homogeneous version of the EC model in terms of incomplete cooling of relativistic electrons below a certain energy.

The criterion determining which radiation field dominates in the Compton energy losses of relativistic electrons can be derived from the comparison of energy densities of these radiation fields in the comoving frame of the jet. Noting that energy density of the synchrotron radiation is

$$u'_s \sim \frac{L_S}{4\pi r^2 c \Gamma^2} \tag{4.1}$$

where L_S is the luminosity of synchrotron radiation and Γ is the bulk Lorentz factor and that the energy density of radiation fields provided by external sources is $u'_D \sim \Gamma^2 u_D$, where

$$u_D = \frac{\xi L_{UV}}{4\pi r^2 c} \tag{4.2}$$

is the the energy density of an external diffuse radiation field, L_{UV} is the luminosity of the central source, and ξ is the fraction of UV radiation, which at a given distance r contributes to the diffuse radiation field.

Sikora et al. (1997) find that the SSC mechanism can only dominate over EC if

$$\Gamma < \left(\frac{L_S}{\xi L_{UV}}\right)^{1/4} \simeq 3\left[\frac{L_{S,47}}{(\xi L_{UV})_{45}}\right]^{1/4} \tag{4.3}$$

or

$$\xi < 10^{-3}\frac{L_{S,47}}{L_{UV,46}}\left(\frac{\Gamma}{10}\right)^{-4} \tag{4.4}$$

where $L_{S,x} = \frac{L_S}{10^x}$ ergs s^{-1}

Since in quasars the reprocessed/rescattered continuum can easily provide $\xi L_{UV} \sim 10^{44} - 10^{45}$ ergs s^{-1}, while statistical analyses (Padovani & Urry 1992) and VLBI observations (Vermeulen & Cohen 1994) give $\Gamma > 5$, the production of gamma rays in the jets of FSRQ is most likely dominated by the EC mechanism.

MeV Break in Compton Models

One of the strongest constraints on the emission models of blazars is the spectral break (i.e. the change of the power-law index) at the frequency where the luminosity peaks. Such breaks can have different origins: they can be related to the break in the electron injection function, as is assumed in homogeneous SSC models (Ghisellini et al. 1996, Mukherjee et al. 1996); they can result from incomplete cooling of relativistic electrons below a given energy, as is predicted by the homogeneous version of the EC model by Sikora, Begelman & Rees (1994); they can reflect the electron spectrum shaped by the pair cascade process, as in the inhomogeneous EC model suggested by Blandford & Levinson (1995); and finally they can correspond to the maximum injected electron energies at a distance where luminosity peaks are produced provided such inhomogeneous models do not involve pair cascades.

The most severe constraints on the nature of the spectral breaks come from the gamma ray observations. There, the spectral breaks observed directly or deduced from extrapolation of the EGRET and X-ray spectra, have a remarkably 'stable' location, usually in the 1–30 MeV range (e.g. von Montigny et al. 1995). Noting that in the homogeneous SSC models the Compton peak is $\propto (\gamma'_b)^4 B'\Gamma$, while in the homogeneous EC models it is $\propto (\gamma'_b)^2\Gamma^2$, this apparent stability of the location of the MeV break seems to require more fine-tuning (as applied to individual sources) of the parameters of the SSC models than of the EC models.

4.4 Hadronic Models

Mücke et al. (2003) looked at BL Lac objects from the point of view of the synchrotron proton blazar model. In this model, the high-energy hump of the SED is due to accelerated protons, while most of the low-energy hump is due to synchrotron radiation by co-accelerated electrons. To accelerate protons to sufficiently high energies to produce the high-energy hump, rather high magnetic fields are required. Assuming reasonable emission region volumes ($R^3 = (10^{15-17})^3 \mathrm{cm}^3$) and Doppler factors ($\sim 10$), Mücke et al. (2003) found that in LBLs, which have higher luminosities than HBLs, there is a significant contribution to the high-frequency hump of the SED from pion photoproduction and subsequent cascading including synchrotron radiation by muons. In contrast, in HBLs they found that the high energy hump of the SED was dominated by proton synchrotron radiation. They were able to model the SED of typical LBLs and HBLs and to model the Mrk 501 1997 flare.

In hadronic models the jet consists of relativistic proton and electron components, which move relativistically along the jet. High-energy radiation is produced through photo-meson production, and through proton and muon synchrotron-pair cascading in the highly magnetised environment. Eichler & Witta (1978) suggested that highly relativistic protons close to the central source produce high energy neutrons through interactions with ambient photons. Either external (i.e. from an accretion disk and/or IR-torus, Protheroe 1996) or internal photon fields (i.e. produced by synchrotron radiation from the co-accelerated electrons, Mücke et al. 2003) can serve as the target for photo-pion production. Putting the energy into the neutrons allows it to be transported to large distances before the gamma rays are produced, which helps to avoid large photon-photon interaction opacities. Hadronic models can, in principle, be distinguished from the leptonic models by the observation of high-energy neutrinos generated in decay chains of mesons created in the photoproduction interactions (for a review see Learned & Mannheim 2000).

As a result of the high-energy threshold for photoproduction, hadronic models require extremely high proton energies which can only be achieved in a highly magnetised environment, and so synchrotron losses become very severe. Magnetic field values of order 10^4 G are expected near the horizon of a supermassive black hole with mass $10^8 - 10^9 M_\odot$ (Blandford & Znajek 1977). Assuming magnetic flux conservation, the jet magnetic field may reach values of 1-100 G in an emission region $\simeq 100 - 1000$ AU away from the black hole horizon.

A hadronic model was considered by Mannheim & Biermann (1992), where electrons and protons in a relativistic jet are accelerated by shocks propagating through the jet. The process favours the acceleration of protons over electrons; because the protons see a

thinner shock front due to a greater gyration radius, they can undergo resonant interactions with the plasma waves and they suffer fewer energy losses at lower energies. The protons acquire Lorentz factors γ_p in the range $10^{10} - 10^{11}$ which is higher than the limit of $\sim 10^8$ required for pion production. The protons interact with soft photons producing mainly pions which decay into neutrino pairs and gamma rays that are further processed. The pairs and gamma rays initiate cascades. If the protons reach their maximum possible energy during the acceleration process, the spectral index in the gamma ray domain $\alpha_\gamma \geq 1$, while if the acceleration of protons is less than the maximum value, $\alpha_\gamma < 1$. The process can produce photons with energy up to the TeV range so that the observation of such ultra-high energy photons from Mrk 421 is naturally explained.

If the coronal radiation is powered by magnetic flares, the pair loading is expected to be non-uniform and non-axisymmetric. Together with radiation drag, this leads to velocity and density perturbations in a jet and the formation of shocks where the pairs are accelerated. Such a scenario can explain rapid ($\sim$ 1 day) variability observed in blazars.

Mannheim (1993) considers relativistic protons in the context of Blandford & Konigl (1979) models of compact radio jets which are assumed to be responsible for the non-thermal emission component of FSRQs and BL Lacs. Baryons are added to the electrons considered as the only radiative agent in the original work.

Mannheim (1993) finds that the differential gamma ray spectrum induced by the protons is an inverse power-law with an index preferentially in the range 1.8 to 2.0. Below a few MeV the spectrum flattens to an X-ray spectrum with index 1.5 to 1.7. For a given energy flux through a jet the apparent radio luminosity is lower for a relativistic

proton enriched plasma than for a relativistic electron enriched plasma (i.e. for jets with a proton/electron energy density ratio > 1) while the apparent gamma ray luminosity is almost constant.

Differential Doppler-boosting, i.e. changes in flux amplification due to changes in the orientation of the radiating plasma element, influences the pair creation optical depth and therefore has an effect on the maximum photon energies of the compact radio source. Hence TeV emission should correlate with high states of the entire continuum flux.

Further consequences are a) an observable diffuse flux of neutrinos with a flat spectrum in the PeV-EeV range, b) a diffuse flux of gamma rays equal to the flux of gamma rays from the Milky Way at an energy of 7 TeV, c) neutrons escaping the blazar that convert their luminosity into the kinetic power of a conical wind surrounding the jet or escape the host galaxy at the highest energies (Mannheim 1993).

Based on the AGN model of Pohl & Schlickeiser (2000), Schuster et al. (2002) predict that the bulk of the neutrino emission is expected between 100 GeV and a few TeV. For a source emitting gamma rays with a flux of $N_\gamma \simeq 10^{-10}$ photons cm^{-2} s^{-1} the observed neutrino rate would be one per month as observed using an instrument like IceCube (Lowder et al. 1991). At this rate an observing time of nearly one year would be required to produce a 3σ detection.

4.4.1 Evidence Regarding Hadronic Models

Cheng & Ding (1994), in their study of gamma ray emission from Mrk 421, used a hadronic model to fit the emission. In their analysis, both electrons and protons could be accelerated to relativistic energy but the maximum energy of electrons was limited by the

radiation loss. Therefore, protons are believed to be the primary accelerated species. Nevertheless, the maximum energy of protons is still limited by either Bethe-Heitler pair production (see appendix B) or pion production in a UV-photon field (Sikora et al. 1987, Begelman et al. 1990). The former and the latter will restrict the Lorentz factor of protons to be 10^6 and 10^8 respectively. The actual maximum energy protons can achieve still depends on the detailed structure of the acceleration region. Nevertheless, the photopion production process is expected to be the dominant mechanism to limit the energy of the proton because its cooling time is $\approx 10^2$ times shorter than that of Bethe-Heitler pair production process (Begelman et al. 1990).

Mücke et al. (2003) applied their synchrotron proton blazar model to the 1997 flare of Mrk 501. They found that an increase of the Doppler factor and acceleration efficiency together with rising proton and electron density (leading to a denser intrinsic synchrotron target photon field) could account for the observations.

Celotti (2002) favours leptonic models as she has concerns about the radiative efficiency, variability timescales, spectral characteristics and relative variability of the two spectral components with hadronic models.

4.5 Infrared Background Absorption

It was suggested by Stecker et al. (1992) that very high energy gamma rays from blazars could be used to measure the intergalactic infrared radiation field, as pair-production interactions of gamma rays with intergalactic IR photons will attenuate the high energy end of blazar spectra. Determining the intergalactic IR field in turn will allow us to

model the evolution of the galaxies which produce it. With a selection of high energy blazars at varying redshifts with known or inferred intrinsic spectra, the attenuation as a function of redshift dependent on the intergalactic IR radiation field can be measured (Stecker & Salamon 1997, Salamon & Stecker 1998). With this information, combined with a direct observation of the IR background from the DIRBE detector on COBE one can, in principle, measure the Hubble constant at truly cosmological distances (Stecker et al. 1994).

There are other areas of physics that would benefit from information on the infrared background. Under certain cosmological scenarios, density fluctuations in the early universe ($z \sim 1000$) could give rise to the pregalactic formation of massive stars ($200 < M/M_{\odot} < 10^5$) at redshifts in the range of $\sim 100 - 300$ (Bond et al. 1984). Very massive objects (VMOs) would collapse to black holes after their main phase without any significant metal ejection. It has been suggested that the remnants of VMOs which would ultimately cluster with galaxies might provide an explanation for the dark matter associated with galaxy rotation curves (Carr et al. 1984). These VMOs would have produced a significant flux of IR photons during their burning phase. Current limits on the infrared background rule out VMO models as providing the explanation for observed galaxy rotation curves, in the absence of substantial reprocessing of radiation by dust (Biller et al. 1998).

Mrk 421 ($z = 0.031$), and Mrk 501 ($z = 0.033$) are particularly useful in separating the spectral characteristics intrinsic to the object from absorption effects in the intervening medium because they have almost the same redshift. They also exhibit strong flares in the TeV energy regime well above typical quiescent levels making detailed spectral

measurements possible for both (Gaidos et al. 1996, Catanese et al. 1997, Aharonian et al. 1997)

The formulae relevant to absorption calculations involving pair-production are given in Stecker et al. (1992). For gamma rays in the TeV energy range, the pair production cross section is maximised when the soft photon energy is in the infrared range:

$$\lambda(E_\gamma) \simeq \lambda_e \frac{E_\gamma}{2m_e c^2} = 2.4 E_{\gamma,\mathrm{TeV}}\ \mu\mathrm{m} \tag{4.5}$$

where $\lambda_e = h/(m_e c)$ is the Compton wavelength of the electron and E_γ is the energy of the gamma ray photon.

For a 1 TeV gamma ray, this corresponds to a soft photon having a wavelength near the K-band (2.2μm). If the emission spectrum of an extragalactic source extends beyond 20 TeV, then the extragalactic infrared field should cut off the observed spectrum between ~20 GeV and ~20 TeV, depending on the redshift of the source (Stecker & Salamon 1997, Salamon & Stecker 1998, Stecker & de Jager 1998).

Stecker & de Jager (1998) concluded that TeV spectra of sources at $z > 0.1$ should suffer significant absorption. Since then however, two blazars at redshifts > 0.1 have been detected in TeV gamma rays: PKS 2155–304 ($z = 0.117$) (Chadwick et al. 1999) and H 1426+428 ($z = 0.129$) (Aharonian et al. 2002, Horan et al. 2002).

Stecker (1999) used the absorption results for the SED of extragalactic IR radiation as calculated by Malkan & Stecker (1998) and assumed an E^{-2} source spectrum and predicted an absorbed spectrum as seen in figure 4.4.

Stecker (1999) found that PKS 2155–304 should have its spectrum steepened by ~ 1 in its spectral index between 300 GeV and 3 TeV and should show an absorption turnover

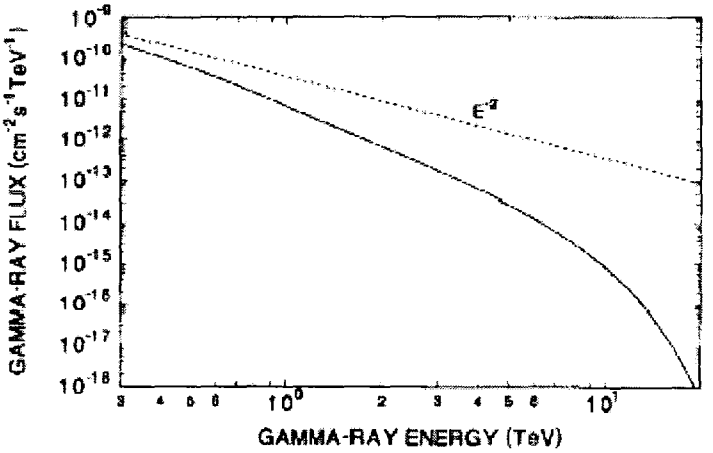

Figure 4.4: Predicted differential absorbed spectrum for PKS 2155–304 (solid line) assuming an E^{-2} differential source spectrum (dashed line) normalised to the integral flux given in Chadwick et al. (1999). Figure taken from Stecker (1999).

above ~ 6 TeV.

4.5.1 Observational Evidence Regarding Infrared Background Absorption

Measurements by various TeV astronomy groups have shown that the energy spectrum of Mrk 501 has significant curvature (Samuelson et al. 1998, Aharonian et al. 1999a, Djannati-Ataï et al. 1999). The two component nature of the multiwavelength picture of blazars implies that over a sufficiently wide energy range, TeV spectra must be intrinsically curved. The measured curvature however depends on the distance of the energy range of the data from the IC peak. During the strong flaring activity, the synchrotron peak of Mrk 501 appears to shift above 100 keV (Catanese et al. 1997, Pian et al. 1998) with the IC peak shifting to several hundred GeV (Samuelson et al. 1998). Measurements by the

HEGRA collaboration have the highest energies extending to $\approx$ 20 TeV; their spectrum is fitted with an exponential cut-off at $\approx 6 - 8$ TeV (Aharonian et al. 1999a, Aharonian et al. 2001).

Several groups have determined energy spectra from Mrk 421, both at low average flux levels (Aharonian et al. 1999b, Krawczynski et al. 2001, Bazer-Bachi et al. 2001) and from intense flares (Zweerink et al. 1997, Krennrich et al. 1999). Analysis of the intense flare data showed that Mrk 421 had a spectral index different (softer) from that of Mrk 501. The fact that the energy spectra of Mrk 421 and Mrk 501 were found to be different was attributed to different intrinsic source spectra, and an interpretation in the framework of a multiwavelength picture was given.

The spectrum of Mrk 421 has high statistical precision and shows a cutoff with a characteristic energy of about $3 - 6$ TeV. The spectrum is best described by a power-law attenuated by an exponential cut-off at an energy of $E_0 = 4.3 \pm 0.3_{stat}(-1.4 + 1.7)_{sys}$ TeV. The cut-off could have several origins, e.g. the termination of the particle energy distribution in the primary beam, the sharp fall in the Klein-Nishina scattering cross section (Hillas 1999), absorption near the gamma ray source (Dermer & Schlickeiser 1994), or absorption by the IR background. If the cut-off energy varied in time or differed for Mrk 421 and Mrk 501 it would be due to the source and not due to extragalactic absorption.

Aharonian et al. (2002) report that the observed energy spectrum of TeV photons from H 1426+428 is in good agreement with an intrinsic power law spectrum of the source $\propto E^{-1.9}$ corrected for absorption by the diffuse extragalactic background radiation (DEBRA). However due to statistical errors as well as uncertainties about the intrinsic source spectrum, they were unable to make any strong statements about the density of

the DEBRA infrared photon field.

4.6 Models Ruled Out

There is no indication of displacement of galaxy isophotes with respect to the nucleus of the galaxy (Falomo et al. 2000). Neither are the galaxy isophotes off-centre with respect to the nucleus (Falomo et al. 2000). This means that the unresolved nuclear source truly sits in the centre of the galaxy, ruling out the microlensing hypothesis for BL Lac objects which predicts these isophote properties. This does not exclude the possibility that some objects could be lensed (see Scarpa et al. 1999) but it cannot be a widespread explanation of the BL Lac phenomenon.

4.7 Conclusion

The discovery of intense gamma ray emission from blazars had a strong impact on our understanding of relativistic jets. The nature of this emission will have an even stronger impact on our understanding of many different aspects of astronomy. It is most likely that it is a combination of the models described that is responsible for high energy emission from blazars.

Chapter 5

Observational History of PKS 2155–304

PKS 2155–304 is a Southern Hemisphere high frequency peaked BL Lac (HBL, see section 3.1.4 for a fuller description). It was first discovered as an X-ray source during observations made with the HEAO 1 satellite (Schwartz et al. 1979, Griffiths et al. 1979) at a position where the Ariel V satellite had previously detected 'confused' emission (Cooke et al. 1978). Like most BL Lac objects it is associated with a compact, flat spectrum radio source and has an almost featureless continuum that extends from radio to X-ray energies. It is the brightest known BL Lac at UV wavelengths, and the object's maximum power is emitted between the UV and the soft X-ray range (Wandel & Urry 1991). PKS 2155–304 has a history of rapid, strong broadband variability as will be shown in this chapter. Due to its brightness, PKS 2155–304 has been the subject of many observations and several multiwavelength campaigns. This chapter will outline the multiwavelength observational history of PKS 2155–304.

5.1 Non-Contemporaneous Observations

PKS 2155–304 has been the subject of many observations at various wavelengths. What follows is a brief account of some of these observations and of the knowledge that can be gained from them.

5.1.1 Radio Observations

PKS 2155–304 has been observed at radio wavelengths on a number of occasions. Tornikoski et al. (1996) reported 1.3 mm and 3.0 mm observations of PKS 2155–304 between 1989 and 1994. The 3.0 mm flux varied between 0.53 $\pm$ 0.06 Jy and 0.18 $\pm$ 0.05 Jy. The 1.3 mm flux varied between 0.33 $\pm$ 0.03 Jy and 0.18 $\pm$ 0.05 Jy. There have been many more radio observations since then, some of which are described later as part of multiwavelength campaigns. PKS 2155–304 is $\sim 10^3$ times fainter in the radio band than the Crab supernova remnant.

5.1.2 Ultraviolet Observations

Edelson (1992) conducted a study of the UV variability of a sample of blazars, including PKS 2155–304, PKS 2005–489 and Mrk 421. Edelson found that the strength of the UV variability was positively correlated with both the apparent UV luminosity and the degree of optical polarisation of the source. This was the first clear indication that the UV continua of blazars are beamed. Edelson noted that Mrk 421 showed a correlation between UV flux and spectral index while PKS 2155–304 did not. Both sources, however, showed correlations between changes in flux density and spectral index.

These results have implications for various emission models. In the case of the SSC model, the long term variability correlation observed gave the first clear indication that the UV emission, like the radio emission, is generally strongly beamed towards the observer.

The accretion disc model would predict that, like type I Seyferts, the luminosity and variability strength of blazars would be anti-correlated, the opposite to what was observed. Blazars show much faster variations than type I Seyferts which would require a smaller accretion disc, although the larger luminosities would require larger accretion discs. These contradictions make the results very difficult to reconcile with the accretion disc model.

In the case of Mrk 421, analysis of spectral variability suggests that the underlying galaxy dilutes the strength of the variations at 2800 Å. This is not the case for PKS $2155-304$, which has a much fainter underlying galaxy and shows weaker variations. This implies that the variations in the central engine of PKS 2155–304 are much less than in the central engine of Mrk 421.

Marshall et al. (1995) conducted a survey using the Extreme Ultraviolet Explorer (EUVE). It was believed that because BL Lac objects are among the brightest extra-galactic sources of extreme UV radiation, this was an indication that they have very little absorbing material in their host galaxies. Models of Marshall et al. (1995) infer a limit on the neutral gas in BL Lac objects of $N_H < 10^{20}$ cm^{-2}.

Marshall et al. (2001) reported observations of PKS 2155–304 taken with the EUVE satellite in May 1994. While it is generally agreed that the soft X-ray emission from many BL Lac objects is the result of synchrotron emission in a relativistic jet (Ulrich, Maraschi & Urry 1997), verification of the synchrotron nature by detection of polarised flux has not yet been obtained. A pure synchrotron spectrum from a uniform source would be

highly polarised, but the optical emission in many BL Lac objects is only moderately polarised, between 5% and 10% in the case of PKS 2155–304. To explain the connection to the X-ray emission most standard models require source inhomogeneities so that the optical and X-ray emission are not necessarily from the same regions. The X-ray emission is expected to arise in a portion of the jet that is closer to the central source and has more well-ordered magnetic fields so the polarisation could approach the theoretical maximum of about 60% to 70% (which depends on the index of the electron energy distribution).

Edelson et al. (1995) found that the UV, optical, and X-ray fluxes appeared to vary nearly simultaneously and with similar amplitudes, lending credence to the idea of a single emission component.

PKS 2155–304 was previously observed spectroscopically in the EUV by Königl et al. (1995) who found evidence for deviations from a simple power-law spectral fit. The deviations could be interpreted in the context of a model in which partially ionised gas that is out–flowing at mildly relativistic ($v \sim 0.1$c) speeds absorbs the continuum in overlapping, Doppler broadened lines of several ionic species. The model reproduced the 600 eV absorption feature first reported by Canizares & Kruper (1984).

The spectra derived from these observations appeared to be consistent with a simple power-law model to within the available statistics and spectral resolution. The exact value of the power-law index depends sensitively on the intervening column density. It is therefore difficult to compare with the power law index measured in the X-ray band. The absorption model suggested by Königl et al. (1995) presented an alternative explanation that could not be ruled out by the data from Edelson et al. (1995) because the ionised absorption edges can overlap so that they are not distinct individually.

5.1.3 Optical Observations

The earliest optical monitoring of PKS 2155–304 reported by Miller & McAlister (1983) showed small amplitude colour variations accompanying long term variations in the optical regime. Pica et al. (1988) reported B-band variations between magnitudes of 12.93 and 14.00 from 1979 to 1986. Carni & Miller (1992) presented long term photometric monitoring results from 1979 to 1990 with a V-band variation between 12.33 and 13.86 mag. Zhang & Xie (1996) constructed a historical light curve for PKS 2155–304, which showed the variation in the B-band was from 12.82 to 14.20 mag. Optical variations on a timescale of the order of one day have been observed by Smith et al. (1992).

Fan & Lin (2000) compiled post 1977 photometric observations of PKS 2155–304 from the Harvard photographic collection. The largest amplitude variations found were: $\Delta U = 1^m.5$; $\Delta B = 1^m.65$; $\Delta V = 1^m.85$; $\Delta R = 1^m.25$; $\Delta I = 1^m.14$. Also colour indices of $(B-V) = 0.30 \pm 0.06$; $(U-B) = -0.72 \pm 0.08$; $(B-R) = 0.62 \pm 0.07$; $(V-R) = 0.32 \pm 0.04$ were found, indicating the dominant emission is in the blue-UV region of the spectrum. Fan & Lin (2000) then used the Jurkevich method * (Jurkevich 1971) and the discrete correlation function method † (Edelson & Krolik 1988), which indicated possible periods of 4.16 years and 7.0 years in the V light curve.

The rapid changes in the optical brightness of blazars, typically with timescales less than a single night, are referred to as microvariations. According to a microvariability study of EGRET blazars carried out by Romero et al. (2002), the shortest gamma ray

*Analysis of expected mean square deviations to search for periodicities in an observational data sample.

†A method for analysing unevenly sampled variability data.

variability timescales ($\sim$ 8 hours, limited by EGRET) as reported for 3C279, a GeV blazar, (Wehrle et al. 1998) are comparable to the preferred timescales for optical microvariability in EGRET blazars. This favours the idea that the optical and gamma ray emission regions are co–spatial and of the order of $10^{15} - 10^{16}$ cm. They believe that if future contemporaneous optical and gamma ray observations revealed the existence of correlated microvariability with zero lag, this would support the SSC model for gamma ray production. However, if non-simultaneous yet well correlated bursts were observed, this would support external Compton models. If an optical burst was observed to precede the gamma ray flare as described by Wagner et al. (1995), this would be indicative of externally rescattered/reprocessed synchrotron radiation from the jet (Ghisellini & Madau 1996).

The most promising scenario to explain the production of both optical and gamma ray flares in blazars is perhaps the so-called shock-in-jet model, where the increase in flux density is the result of shocks formed due to velocity irregularities in the relativistic flow of the jet (e.g. Marscher & Gear 1985, Sikora et al. 2001). Particles in the shocked region cool through synchrotron radiation at optical wavelengths and through the inverse Compton mechanism at gamma ray energies.

Romero et al. (1999), suggested that the difference in the microvariability behaviour of low frequency peaked BL Lacs (LBLs, as described in section 3.1.4) and HBLs could be due to the effect of stronger magnetic fields in HBLs. These fields can prevent the formation of features like density inhomogeneities and bends in the base of the jets by Kelvin-Helmholtz macroscopic instabilities. The results of this study could imply that strong perturbations (like propagating shock waves) are a common phenomenon in the initial section of the jets of radio loud objects whereas localised disturbances in the accretion

discs are more rare occurrences at least at very short timescales. The relativistic jets of radio loud sources seem to be very prone to undergoing strong perturbations. If the flux microvariations are associated with the interactions of thin shocks with small features (e.g. eddies or inhomogeneities in the particle density) in otherwise steady jet flows, then rapid variability studies can be used to explore the fine-scale structure of the inner jet.

Optical Polarisation Studies

Relativistic beaming enhances the polarised non-thermal jet radiation with respect to the unpolarised emission of the host galaxy, resulting in a high net polarisation percentage. Therefore, the short timescale variation of the polarised light traces the dynamics of the plasma inside the jet and monitoring this variation yields the most direct insight into the jet physics and powering source.

Tommasi et al. (2001) intensively and simultaneously monitored the polarised and total flux of PKS 2155–304 in the optical UBVRI bands with the Turin photopolarimeter at the CASLEO 2.15m telescope during four campaigns in 1998 June, August and November and 1999 August (~47 hours). PKS 2155–304 showed a linear polarisation percentage usually ranging between 3% and 7% and a polarisation position angle mainly between 70° and 120°. The highest temporal resolution of 15 min allowed them to detect amplitude variation of the linear polarisation from 6% to 7.5% on timescales of hours. On 8 June 1998, they recorded a decrease of a factor of two in the degree of linear polarisation in all bands, while the polarisation position angle rotated by 90°. This observation was consistent with the presence of two emission components of different polarisation strength and position angle. Intra-night variability of linear polarisation and polarisation position

angle can be interpreted as being due to small-amplitude physical or geometrical changes within the jet. Measurements of the circular polarisation over time intervals of days set upper limits of 0.2%. There was no correlation between flux variations and linear polarised flux.

5.1.4 Infrared Observations

By examining the IR emission from blazars it is possible to examine the soft seed photons that scatter ultra-relativistic electrons by inverse Compton scattering. PKS 2155–304 was detected by the Infrared Astronomical Satellite (IRAS) in 1983 at 12, 15 and 60 microns with a flux of about 100 mJy in all three bands (Impey & Neugebauer 1988). Later observations by Bertone et al. (2000) with ISO revealed that the IR emission had remained constant with time. They have also shown that the contribution to the IR flux from the host galaxy is negligible.

5.1.5 X-ray Observations

In TeV blazars the X-ray emission probes the electrons accelerated to the highest energies; those electrons have the shortest synchrotron cooling times. When events in the jet (such as shocks or changes in the magnetic field) cause changes in the electron energy distribution, we see corresponding changes (such as flares) in the emitted X-rays. From the energy dependence of these variations we can infer constraints on the timescales for acceleration, injection and cooling and on the size of the synchrotron emitting region. X-ray variability on the shortest time scales allows us to derive the sizes of the inner nuclear regions and to trace the kinematics of the jet and thereby study how the relativistic

particles are accelerated and injected in the emission region and how efficiently they cool thereafter and escape.

PKS 2155–304 has been the subject of many X-ray observations (e.g. Angel & Stockman 1980, Mead et al. 1990, Maccagni et al. 1989, Burbidge & Hewitt 1992, Giommi et al. 1990, Hewitt & Burbidge 1993). The historical observed X-ray flux range of PKS 2155–304 spans $\sim (1.5 - 2.5) \times 10^{-11}$ ergs cm^{-2} s^{-1} (Kataoka et al. 2000).

A deep absorption feature at 0.6 to 0.7 keV was detected using the objective grating spectrometer on the Einstein Observatory (Canizares & Kruper 1984). Assuming a redshift of z$\simeq$0.1 the most likely interpretation for this feature is an O VIII Lyα resonance absorption trough associated with hot gas with an outflow velocity of 30,000 km s^{-1} (Canizares & Kruper 1984).

Ghosh & Soundararajaperumal (1995) reported on the multifrequency spectra of EXOSAT blazars, PKS 2155–304 included. They reported that the spectrum of PKS 2155–304 could be best described by a broken power law with a fixed absorption model.

In PKS 2155–304 extrapolations of the flat optical to UV continuum and steep X-ray continuum meet in the soft X-ray band. This spectral form is suggestive of a direct synchrotron origin, with the spectral break being attributable to radiation losses suffered by the electron population. These results suggest that the majority of the variations in the UV to X-ray continuum of PKS 2155–304 can be explained by two factors. First, the whole continuum can rise or fall with a correlation between the hardness of the X-ray slope and the intensity on time scales of a week or greater. Second, rapid variations within the X-ray band occur on timescales down to a few hours which can be parameterised by assuming that the spectrum pivots about a break point $\sim$ 0.3 to 0.4 keV. Variability of the first

type has been modelled by Celotti et al. (1991) who have calculated the time dependent spectral properties arising from a perturbation of the synchrotron emissivity travelling at a fixed speed down the axis of a jet. Below the break frequency of the stationary jet the spectral slope remains constant, whereas at high frequencies the slope hardens with increasing intensity. Temporal variations in the efficiency of the re-acceleration process within the X-ray emitting region could therefore provide a plausible physical mechanism for some of the rapid X-ray variability.

Tanihata et al. (2001) reported ASCA observations which included detailed examination of flares. This examination showed that each of the strong flares did not increase and decrease smoothly but exhibited substructures of shorter flares having a timescale of $\sim$10 ks. The energy dependent cross-correlation analysis showed that inter-band lags are not universal in TeV blazars. Tanihata et al. (2001) determined that the sign of a lag may differ from flare to flare; significant lags of both signs were detected from several flares while no significant lag was detected from others. Tanihata et al. (2001) argued that the nature of the underlying component could affect these values. The fact that all flares were nearly symmetric and that fast variability shorter than the characteristic timescale was strongly suppressed, supports the scenario where the light crossing time dominates the variability timescales of the day-scale flares.

Tanihata et al.'s (2001) observations of time resolved spectra integrated over short time periods, were well fitted by power laws with photon indices in the range $\Gamma = 2.5 - 2.8$, consistent with previous observations. They believe that the synchrotron peak must be below $\sim$1 keV and the observed X-rays represent synchrotron emission from the high-energy tail of the electron energy distribution. There was continuous flaring throughout

the 10 day ASCA observations, each flare having an amplitude of $\sim 30 - -50\%$. The variability amplitudes in the hard and soft X-ray bands were very similar, indicating only a modest spectral change even during the large amplitude flare. The variability in the two energy bands was well correlated and lags between flare maximum in the two bands were smaller than $\sim 10^4$ s. A close look at the light curve showed substructures present in the large flare. Shorter variability with rise and decay timescales of ~10 ks was clearly seen.

Structure function analysis by Tanihata et al. (2001) showed that all TeV blazars have a break in the structure function at a timescale of ~1 day indicating a characteristic timescale and a very steep slope below the characteristic timescale that suggested strong suppression of the more rapid variability. They inferred that the timescale of the break in the structure function indicated the minimum timescale of the individual shots and the slope at shorter timescales than the break becomes steeper than 1 until it finally reaches 2. On the other hand they also detected faster substructures having timescale of ~10 ks but with smaller amplitude.

The energy dependent cross-correlation suggested that inter-band lags are not universal in TeV blazars. Multiple flares detected in the long-look observations showed that the energy dependence of the lags differed from flare to flare. This supports the inference that the timescales of acceleration and cooling of the electrons responsible for the X-ray emission are comparable for TeV blazars and the balance of these parameters controls the lags. Uncertainties remain however, mainly concerning the nature of the underlying component of variability on even longer timescales than considered in Tanihata et al. (2001).

It is striking that in this source similar patterns of X-ray variability are seen spaced apart by many years suggesting recurrent conditions in the mechanism of jet powering and activity development (Brinkmann et al 2000).

Zhang et al (2002) reported on 3 sets of BeppoSAX observations recorded in November of 1996, 1997, 1999. Successive flares were detected. The variability showed larger amplitudes and shorter timescales at higher energies. The power spectral densities had steep power-law slopes of $\sim 2-3$ indicating shot noise variability. From cross correlation analysis they found that the values of soft lags, i.e., delays of soft ($0.1-1.5$ keV) photons with respect to hard ($3.5-10$ keV), differed from flare to flare, ranging from a few hundred seconds to about one hour. The soft lags were also energy dependent, with longer lags of lower energy emission with respect to the emission in the $4-10$ keV range.

PKS 2155–304 was brightest as observed by BeppoSAX in 1997. In 1996 PKS 2155–304 was found to be in an intermediate state of flux and it was faintest in the 1999 data. The main conclusions of these observations were that

- The amplitude of variability was larger and doubling timescales shorter at higher energies. Both quantities did not correlate with the brightness of the source and complex behaviours were detected

- The variability of the source could be ascribed to the shot noise

- Soft X-ray photons lagged the hard ones and the value of the soft lags seemed to correlate with the duration of the flares

- Time resolved spectral fits with a curved model suggested that the peak position of synchrotron emission would move to higher energy with increasing flux

- Spectral changes were complicated without any clear correlations of spectral slope versus flux and between spectral slopes at different energies

Other X-ray observations taken as a part of a multiwavelength campaign will be described in section 5.2.

5.1.6 GeV-MeV Gamma ray Observations

The EGRET experiment on board the Compton gamma ray Observatory was used to detect 30 MeV - 10 GeV gamma ray emission from PKS 2155–304 during 1994 November 15-29 (Vestrand, Stacy & Sreekumar 1995). These observations indicated a very hard spectrum with an integral power law spectral index of 1.71 $\pm$ 0.24, and this, combined with its proximity, makes it an excellent candidate TeV source. However, a recent detailed analysis of the shape of the X-ray spectrum and of the X-ray variability by Giommi et al. (1998) suggested that PKS 2155–304 would not be an important TeV emitter producing photons with a maximum energy of ~800 GeV, although a very high degree of beaming may allow the production of photons with higher energies. The idea of the presence of a high degree of beaming was further reinforced by the detection of PKS 2155–304 at TeV energies as reported by Chadwick et al. (1999). Indeed, the absence of any signature of gamma ray absorption due to pair production at energies up to 8 GeV in observations of PKS 2155–304 is consistent with the suggestion that it contains a relativistic jet oriented nearly along our line of sight (Vestrand, Stacy & Sreekumar 1995).

5.1.7 TeV Gamma ray Observations

Results of observations with the Mark 6 between 1996 and 1999 will be discussed in detail in chapter 6

There are currently only two ground based atmospheric Cherenkov telescopes located in the Southern Hemisphere, CANGAROO in Woomera, Australia and H.E.S.S. near Windhoek, Namibia.

The CANGAROO collaboration published a paper on observations of three HBLs, PKS 2155–304 being among them. Their observations took place during October, November and December 1997 and were split into two distinct sets. The first set contained 14 hours of on-source and 13 hours of off-source observations with an estimated energy threshold of 1.5 TeV. The second set contained 5 hours of on-source data and 5 hours of off-source data with an estimated energy threshold of ~2.5 TeV. They found no evidence for gamma ray emission in these observations. They published upper limits to emission based on these observations at $F_{(>1.5\ \mathrm{TeV})} < 9.5 \times 10^{-12}$ photons cm^{-2} s^{-1} and $F_{(>2.5\ \mathrm{TeV})} < 0.6 \times 10^{-12}$ photons cm^{-2} s^{-1}.

It is probable that that the infrared background attenuates the high energy emission from blazars, as discussed in section 4.5. This is one possible explanation for why no emission was detected at these energies.

5.2 Multiwavelength Observations

By constructing the overall spectral energy distribution (SED) of a blazar and by determining the relationships between the emission in different energy bands, the physical

parameters describing the system and the emission mechanisms taking place can in principle be constrained. Moreover, the temporal evolution of the SED and in particular the inter-band relationships can be used to explore the dynamics and the structure of the jets which ultimately give clues to the physical properties of the blazar system.

A good multiwavelength campaign of a TeV blazar object will have simultaneous observations in as many wavelength regimes as possible. In gamma ray astronomy, the most relevant are observations in the X-ray and TeV regimes combined with UV/optical/IR observations. Ideally a campaign would be long enough to cover quiescence, pre-flare, flare and post-flare activity. This would enable the study of inter-band relations at all stages in a blazar's activity.

The 1994 campaign (section 5.2.3) covered optical IR, radio and UV/EUV/X-ray observations, no TeV observations were taken at this time however. The 1997 campaign (section 5.2.5) covered TeV and X-ray observations only. A more comprehensive campaign is planned for the future.

5.2.1 1983 to 1985

Treves et al. (1989) reported X-ray observations of PKS 2155–304 taken over nine epochs between 1983 and 1985 with the EXOSAT satellite (0.1 - 15 keV range). These were complemented by simultaneous and quasi-simultaneous observations in the far-UV with the International Ultraviolet Explorer (IUE) and in the optical and infrared with ESO telescopes. Analysis of the X-ray observations found on two occasions that the flux showed a rapid regular rising with a doubling time $\sim$1 hr. Marginal evidence for an absorption edge was found at $\sim$7 keV in the best exposed spectrum. It was later suggested by

Giommi et al. (1998) that this absorption feature could be the Fe K_α line which could indicate the presence of cold gas, possibly associated with an accretion disc (George & Fabian 1991).

The quasi-simultaneous UV and optical data allowed the reconstruction of the energy distribution on several occasions. They found that on all but one of these occasions, the optical, UV and X-ray intensities were correlated. They also noted that the variability amplitude decreased and the timescales increased with decreasing frequency. They concluded that those results were indicative of an inhomogeneous model of the source, with the inner region being responsible for the X-ray emission and the periphery for the radio, as proposed by Urry & Mushotzky (1982). They believed that the origin of the X-rays was synchrotron emission and that there were distinct but connected emission regions for the X-ray, UV and optical bands during their observations.

5.2.2 The 1991 November Multiwavelength Campaign

These observations are reported in Urry et al. (1993), Brinkmann et al. (1994), Courvoisier et al. (1995) and Smith et al. (1992).

PKS 2155–304 was monitored daily throughout November 1991 with the IUE satellite and the results were reported by Urry et al. (1993). This study revealed large amplitude, rapid variations in the UV flux of this BL Lac object. Over the course of the month a doubling of the flux over about 10 days with smaller, more rapid flares superimposed on this general trend was observed. The well-resolved flares that occurred during the intensive monitoring had an apparent quasi-periodicity of ~0.7 days. This, however, is only marginal evidence for periodicity as the data train was too short to confirm the

reality of the period. Such flares might be expected from disturbances propagating along the magnetic field lines in a jet (Camenzind & Krockenberger 1992).

The short and long wavelength UV light curves are well correlated with each other and with the optical light curve. The formal lag was zero but the cross-correlation was asymmetric in the sense that the shorter wavelength emission led the longer, suggesting that the loss time scales were faster for the shorter wavelength emission, as expected in the synchrotron process.

Small but significant spectral variability was detected. The UV spectral index and intensity were inversely correlated (harder spectra corresponding to higher intensity) but the change in index led the change in intensity by 1 or 2 days. The inverse correlation between spectral index and intensity was consistent with the non-thermal acceleration processes expected in relativistic plasmas so that the present results were again consistent with relativistic jet models. The accretion disc scenario of Wandel & Urry (1991) was ruled out because of the simultaneous optical and UV variability. This correlation is not predicted in an accretion disc model.

Brinkmann et al. (1994) reported on the ROSAT observations of PKS 2155–304 taken from $12^{\rm th} - 15^{\rm th}$ Nov 1991. The source was found to be in a bright state with a soft X-ray flux of $F_{\rm x}(0.1 - 2.4 \text{ keV}) \approx 7 \times 10^{-10}$ erg cm^{-2} s^{-1}. The observations were performed nearly continuously over $\sim$3 days and showed flux variations from the source of about 30%. The timescale was typically one day and variations at the percent level on timescales of a few hundred seconds may have been present as well. The spectral form remained constant during the observations. The light curve showed nearly simultaneous strictly correlated variations over a broad energy band, from optical to X-ray wavelengths, with the exception

that at the beginning and at the end of the X-ray observations, the UV and X-ray light curves did not correlate as closely as they did in the middle of the observations.

The existence of an absorption feature at an energy of ~600 eV could neither be confirmed nor ruled out by the ROSAT observations. Previous observations by Gould & Jung (1991) claimed that this could be the edge for atomic oxygen at 546 keV, with a reduced photoionisation cross section. If this were confirmed it would prove that the absorption occurs close to the source in a region whose degree of ionisation depends on the strength of the beamed radiation emitted by PKS 2155–304.

Courvoisier et al. (1995) reported on the ground-based observations taken in radio and UBVRI wavelengths together with optical polarimetry. The optical and IR observations of November 1991 produced a set of well-sampled light curves which all had the same shape, and from which only an upper limit to possible lags could be deduced. The 20cm radio observations, although insufficiently sampled to study the variability on short time-scales, did not follow the higher frequency behaviour. The polarised flux varied with an amplitude larger than the total flux at the same frequency. The variations of the polarised flux did not correlate with variations of the total flux, or those of the X-ray emission during the same period.

The lack of correlation of the spectral shape (i.e. the spectral slope) observed in the U-I range with the flux variations indicated that variations in the beaming factor (either bulk Lorentz factor or orientation) of the jet or parts of the jet were probably being observed rather than variations in the rate of acceleration or cooling.

Smith et al. (1992) reported on ground based optical polarimetry and photometry before and during the IUE monitoring programme from 1-29 November 1991. They reported

that PKS 2155–304 generally brightened throughout the monitoring programme and was nearly 0.8 mag brighter near the close of the IUE program than at the beginning. The maximum daily fluctuations in brightness were ~0.1 mag. No significant changes in the UBVRI colours of the object were observed.

Smith et al. (1992) noted that variations in the linear polarisation were substantial but no correlations with the fluctuations in brightness were apparent. The degree of polarisation varied between 2% and 8% and θ varied between 105° and 140°. The maximum daily variations in polarisation were only 2% - 3%; however, the polarisation position angle, θ was observed to change by as much as 25° in 24 hours.

Any wavelength-dependent polarisation was very weak and there was little evidence for variability throughout the monitoring campaign. The polarisation increased slightly into the blue. On most nights there was no evidence for wavelength dependence in the polarisation position angle.

The optical polarised flux varied much more rapidly than the total optical flux. The variability time scale of the polarised emission was similar to that of the soft X-rays. Comparison of the optical polarised flux variability with variations in the X-ray band may determine if the polarised emission is produced in the same compact region as the X-rays.

These observations are strong evidence that the optical radiation observed is dominated by synchrotron emission from a compact region and that only one emission component is responsible for the observed behaviour during the observed time. Given that the spectral index and the wavelength dependence of the polarisation did not vary substantially it is extremely difficult to explain the generally lower polarisation observed for

PKS 2155–304 compared to LBL objects with a separate emission component that dilutes the synchrotron spectrum.

5.2.3 The 1994 May Multiwavelength Campaign

These observations were reported in Pesce et al. (1997), Pian et al. (1997), Urry et al. (1997) and Edelson et al. (1995).

Pesce et al. (1997) reported on the optical, IR and radio observations as well as on the continuous UV/EUV/X-ray observations during the monitoring campaign in May 1994.

The possibility of a lag of several days between the 8.4 and 15 GHz data and those at 22.5 GHz was reported. When compared with the optical data obtained over the same period, no direct correlation was found, although the 4.8 GHz data from the first 10 days of observations may correlate with the optical data with no measured lags. Any correlation between the radio and the optical data could be spurious, since there were variations on timescales of several days in both bands and many large gaps in coverage.

The fastest (optical) variation of 0.01 mag minute^{-1} makes PKS 2155–304 the most rapid optically variable BL Lac observed to date. The timescales were similar to those observed in the UV (Pian et al. 1997). With a large number of assumptions they limit the mass of the central black hole to $M_{var} \lesssim 1.5 \times 10^9(\delta/10)M_\odot$ where δ is the Doppler factor of the relativistic bulk motion. This is consistent with the mass determined from UV and X-ray constraints and considerably less than was determined previously in the optical band.

Smith et al. (1992) and Courvoisier et al. (1995) found the source to have constant colour. Trends in (B-V) colour have been noted before in the sense that the source

becomes bluer as it fades (Miller & McAlister 1983, Carni & Miller 1992). However, during the 1994 campaign the opposite occurred with slightly redder colours observed as the source faded. This is similar to the result found by Treves et al. (1989) and Smith & Sitko (1991). It is therefore believed that there is more than one physical process at work to create these two different observations.

Polarimetry measurements showed marked colour dependence of the polarisation (higher polarisation towards the blue), which is the strongest such dependence ever observed for PKS 2155–304. The object was also seen to have the highest optical polarisation observed (U band polarisation = 14.3%) although within the range typical for HBLs (Jannuzi 1994). The polarisation variations trace the flares seen in the UV flux.

Pian et al. (1997) describe the IUE observations at ~1 hr time resolution for 10 nearly uninterrupted days in 1994 May. Spectral changes were generally modest and not clearly correlated with flux variations. A resolved central flare of ~35% amplitude was observed in both IUE cameras and was probably correlated with flares of different amplitude and duration at higher energies (Urry et al. 1997). The source flared dramatically and its UV flux increased by a factor of 2.2 in 1.5 hr. This event, which suggested the occurrence of variability on timescales even shorter than the IUE time resolution, represented a definite violation of the limits on luminosity variability, therefore implying the presence of relativistic beaming. Both variability events could be interpreted within a scenario in which synchrotron radiation is the primary emission mechanism and a lower limit of 1 G on the intensity of the magnetic field could be determined. This turns out to be consistent with a calculation of this physical quantity based on the multiwavelength data and with the gamma ray flux observed by EGRET (Vestrand, Stacy & Sreekumar 1995). Unlike

the findings of the 1991 campaign, no periodicity was seen in the 1994 data. The ~1 day anti-correlation between flux and spectral variations was maintained.

Urry et al. (1997) reported on the 2 day X-ray observations taken with ASCA and ROSAT and discussed the results in relation to the other observations taken during the 1994 multiwavelength campaign.

The light curves showed well-defined X-ray flares followed by a broad, low amplitude UV flare ~2 days later. X-ray fluxes were obtained at three well-separated times the preceding week, indicating at least one previous flare of comparable amplitude or perhaps ongoing random X-ray variations. Additional rapid variability was seen at the beginning of the IUE observation, when extremely sharp changes in the UV flux occurred. The X-ray flux observed with ASCA increased by a factor of ~2 in about 0.5 days and decayed roughly as quickly. In contrast the subsequent UV flare had an amplitude of only ~35% and lasted longer than 2 days.

Assuming that the X-ray, EUV and UV events are associated, the lags, the decreases of amplitude with wavelength and the broadening of the temporal profile with wavelength are all qualitatively as expected for a synchrotron emitting region.

Alternatively, the data are consistent with a compression wave or other disturbance crossing a region with stratified particle energy distributions. This kind of situation is expected to occur behind a shock front and/or in an inhomogeneous jet. The May 1994 light curves are in sharp contrast to the multiwavelength variability observed in November 1991, when the amplitude was wavelength independent and the UV lagged the X-rays by less than ~3 hours. This means that the origin of rapid multiwavelength variability in this blazar is complex, involving at least two different modes.

The apparent progression of a strong X-ray flare to longer wavelengths rules out a random acceleration process in a homogeneous volume. It can possibly be explained by an instantaneous injection of high-energy particles near X-ray emitting energies and subsequent energy degradation in a homogeneous radiating synchrotron source. This injection could be achieved by a single-stage acceleration as with a large-scale electric field (Bednarek et al. 1996a, Bednarek et al. 1996b). The estimated physical parameters are similar to those derived with the same assumptions from similar data for the BL Lac object Mrk 421 (Takahashi et al. 1996)

The different multi-frequency behaviour observed in 1991 indicates that different mechanisms drive the variability are in operation in this source.

This X-ray/EUV/UV/optical monitoring of PKS 2155–304 established for the first time that:

- The X-ray through optical emissions in blazars are closely related.
- Variability occurs on timescales less than 1 day.
- The X-ray flux variation leads the UV by a few hours to a few days.

Brinkmann et al. (2000) compared the 1991 and 1994 multiwavelength campaigns. The light curves of PKS 2155–304 from the two campaigns showed significant differences (Urry et al. 1997). In 1991, the X-ray/UV/optical variations were of similar low amplitude, the measured lag was quite small and the variations were nearly achromatic. In 1994, the X-ray flare was much larger than the nearest UV flare and the lag was at least two days. The larger-amplitude wavelength-dependent variability and larger lag in 1994 are likely to result from physical processes in the relativistic jet itself.

The first campaign (November 1991) had only 3.5 days of overlap between X-ray and UV/optical, enough to show a clear correlation and to measure a possible lag, but the X-rays and UV flux appeared to diverge at the end.

The second campaign (May 1994) was excellent in UV coverage but had less than two days of ASCA observations. The X-ray flare appeared to precede the EUV and UV flares by 1 and 2 days respectively. However, only 2 of 12 days were covered by X-ray observation so this depends on the uncertain association of the X-ray flare with the UV i.e. it could be related to another flare at the beginning of the UV light curve. These findings prompted another multiwavelength campaign, set for 1996.

5.2.4 The 1996 Multiwavelength Campaign

Bertone et al. (2000) reported on Infrared Space Observatory (ISO) observations of PKS 2155–304 in May and June 1996 taken during a multiwavelength campaign. It was found that the overall infrared to X-ray spectral energy distribution could be well explained by optically thin synchrotron emission with negligible contributions from thermal sources such as the host galaxy. The ISO light curves of May- June 1996 showed that the time variability of PKS 2155–304 in the mid- and far- infrared bands was very low or even absent. They also noted that the flux had not varied significantly in November 1996 and May 1997 and was similar to that recorded by IRAS in 1983 (except at 60 μm where the IRAS flux seemed significantly lower).

The variability in the optical bands was small as well, while the simultaneous RXTE light curve showed strong and fast variability at energies of $2 - 20$ keV (Urry et al. 1998).

The observations could be explained by assuming that the X-ray flux is due to the

steep tail of an electron population distributed in energy as a broken power law. The first part of this distribution is flat and steadier than the high energy, steeper part. In this case, without changing significantly the bolometric luminosity, large flux variations are possible above the synchrotron (and Compton) peak. An electron distribution with these characteristics can be obtained by continuous injection and rapid cooling (e.g. Ghisellini et al. 1998).

A preliminary report on the RXTE, ROSAT and EUVE data is given by Urry et al. (1998). The RXTE observations were planned for May 1996, but due to unrelated target of opportunity observations they were interrupted. The missing time was re-scheduled for November 1996, contemporaneous with ROSAT and BeppoSAX observations of PKS 2155–304. The RXTE light curves showed strong variability with variations as large as a factor of 2 on timescales of less than a day. For both epochs, the variability amplitude is similar at soft ($2-6$ keV) and hard ($6-20$ keV) X-ray energies. No lags were detected for the better sampled light curve in May, although lags of a few hours or less would not have been detected.

A flare was detected with RXTE around May 17, but was not detected with ROSAT. The flare was found not to be due to variations in the proportional counter array background nor was there a different flaring source in the background.

Brinkmann et al. (2000) reported on the ROSAT observations throughout May and November 1996. They found that the observed intensity variations of more than a factor of 2 in May and of about 20% in November can be separated into slow flux changes with timescales comparable to the observation intervals and superposed, low amplitude flares with durations of $\sim$1 day. They found that a comparison with all previous ROSAT obser-

vations of PKS 2155–304 confirmed the persistence of these phenomena. They concluded that this may be the first AGN where systematic intrinsic temporal variations like the precession of the jets can be observed in X-rays given a sufficiently long observational coverage.

They also noticed a systematic pattern in the variability which can clearly be seen by comparing the light curves taken in 1991 and 1996. They believe that this could be explained by variations associated with a varying aspect, e.g. a helix associated with the rotational dragging of a magnetic field. If the shots or outbursts, characteristic of the short-term variability, occur in blobs of enhanced activity travelling down the jet then they cannot be generated randomly; a rather well defined physical mechanism must at least initiate the generation of these regions.

5.2.5 1997 Campaign

In November 1997, contemporaneous with some of the observations documented here, X-ray emission was detected with the BeppoSAX satellite (Chiapetti et al. 1999) with a flux equal to the strongest previous outburst. Observations of PKS 2155–304 at this time were also taken with RXTE (Vestrand & Sreekumar 1999) and with the University of Durham Mark 6 Telescope (Chadwick et al. 1999).

X-ray observations reported by Chiapetti et al. (1999), taken on 22 November 1997 for 1.5 days found PKS 2155–304 to be in a high X-ray state. The amplitude of variations was seen to increase with energy and the presence of a soft lag with a timescale of the order 10^3 s was found. A continuum spectrum extending to ~50 keV was seen, with no evidence of spectral features. This is consistent with interpretation of the broadband

SED due to SSC emission from a single region. The observed shifts of the SED peaks between the lowest and highest flux levels could be accounted for by an increase of the break energy in the relativistic particle spectrum.

The X-ray state observed by BeppoSAX was one of the highest ever detected though lower than that observed by RXTE before the start of the BeppoSAX campaign. The RXTE observations reported by Vestrand & Sreekumar (1999) were taken on 20-21 November 1997 and found $F_{(2-10\mathrm{keV})} = 2.3 \times 10^{-10}\mathrm{erg\ cm^{-2}s^{-1}}$. The data showed a correlation between the 2–10 keV X-ray outbursts and the GeV/TeV gamma ray outbursts.

5.3 Conclusion

Currently, the most widely accepted picture of blazar emission at radio through UV wavelengths is the synchrotron process in an inhomogeneous jet (Pian et al. 1997). As the spectral steepening from optical to UV to X-rays observed in PKS 2155–304 can be attributed to the decreasing volume of the region emitting at higher frequencies in the inhomogeneous jet model. The completely resolved central flare in the 1994 campaign, together with the 50% and 80% correlated flares detected at the EUV and X-ray wavelengths (Pian et al. 1997), is consistent with a variability amplitude monotonically increasing with energy, as expected for a synchrotron flare in an inhomogeneous jet (Celotti et al. 1991, Georganopoulos & Marsher 1996).

Models are described in more detail in chapter 4 and are typically characterised by a spatial dependence of the magnetic field, electron density and maximum electron energy

and usually incorporate a relativistic velocity of the plasma within the jet which causes beaming of the radiation. The method of power transport along the jet and of transference of power to the high energy electrons responsible for the observed emission is still not known.

Chapter 6

University of Durham Mark 6 Telescope Observations

This chapter discusses the operation of the University of Durham Mark 6 Telescope, hereafter the Mark 6. The pre-analysis processing to which data are subjected is also discussed.

6.1 Observation Modes

There were various modes of observing sources with the Mark 6, depending on the source itself, the time of year and its observational history. Methods used to observe PKS 2155–304, PKS 2005–489 and PKS 0548–322 are described in this section.

6.1.1 Chopped Mode

This was the most common mode of observing PKS 2155–304 and the only mode used to observe PKS 2005–489 and PKS 0548–322. The Mark 6 tracked the same zenith/azimuth space either before or after an on-source exposure. This was achieved by pointing the Mark 6 $\pm 3.75°$ in RA from the on-source track. The on and off-source observations were separated enough that the two fields did not overlap, but were close enough together that a similar region of the sky was observed, in terms of sky brightness etc. The corresponding on-source and off-source observing runs were sufficiently close in time that sky conditions were similar. The order of chopped mode observations was either on-off-off-on (i.e. on-source observation followed by a control exposure, followed by a control exposure followed by an on-source observation) or off-on-on-off in order to avoid systematic effects due to, for example, the on-source observations always occurring before the corresponding off-source observation. This method of observing removed linear effects and secular changes in conditions e.g. sky clarity, temperature etc., to the first order.

This observing mode had the advantage that there was always a measure of the night sky background not contaminated by emission from the target source. The objective was to generate a comparison off-source dataset which was as similar to the on-source data as possible except for the presence of the target in the on-source field. The disadvantage was that the object was not continuously kept in the field of view of the telescope.

6.1.2 Offset Tracking Mode

In this observation mode the target object was kept constantly in the field of view of the detector. The position of the target in the field of view of the camera was changed by 0.5° in RA every three minutes to either lead or trail the source. This implies a small rotation of the object in the field of view because of the change in zenith angle of the object and the telescope's alt-azimuth mount.

To determine off-source data in this mode of observation the following procedure was applied. The same physical events were used but their Hillas parameters were calculated with respect to a virtual off-source position. This virtual off-source position was taken to be a position at the same distance from the centre of the field as the actual source position, where the straight line connecting the virtual off-source position and the actual on-source position passed through the centre of the field of view.

The advantage of this observation mode is that it allowed for longer on-source observations within one night; more specifically the target is never absent from the field of view. This is especially important when observing objects such as blazars, whose emission is known to vary on very short timescales. The disadvantage is that the off-source data are not independent of the on-source data, as in chopped mode. This method of tracking is more difficult and time intensive to analyse as there is not a distinct off-source dataset.

The same Hillas parameter selections were used (see table 6.1) together with a distance cut to exclude any events at the edge of the camera.

6.2 Data Reduction

Data were subject to standard pre-processing routines to eliminate any biases which may have been introduced during observing from either the apparatus or the observing environment. A flow chart outlining these processes can be seen in figure 6.1.

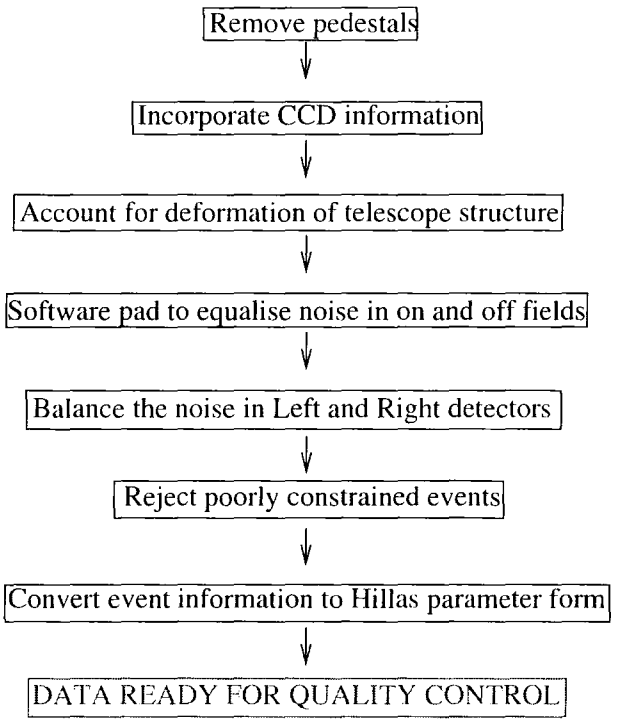

Figure 6.1: The processes to which data are subjected in pre-processing.

The status and condition of influencing factors were recorded during observing. Weather conditions, such as humidity, temperature, atmospheric pressure, and wind speed were recorded at the time of observations. A mid-infrared radiometer was used to measure sky clarity (Buckley et al. 1998, Aye et al. 2003). The status of the various parts of the experimental apparatus were also monitored, such as the currents in the PMTs in the detector packages. The temperature of the PMTs were also stabilised during observations.

In the absence of a Cherenkov signal a PMT will detect random fluctuating signals from

the night sky background. The electronic units which measure the PMT signals were given an artificial positive DC offset, called a pedestal. This was so the system could measure negative charge values i.e. ensured that downward noise fluctuations remained positive. The pedestal had to be subtracted from the signal before the data could be analysed. The pedestal was measured by triggering the telescope throughout an observation with a computer, at a mean rate of 50 per minute. This gave a measure of what the charge digitisers read when there was no Cherenkov light incident on the PMTs. These levels were subtracted from data to account for background noise recorded by the system electronics.

The Mark 6 was equipped with a 337 nm pulsed laser (pulse length 3 ns). The laser fired pulses at random intervals, through a scintillator, at the detector package in order to measure the response of the PMTs. This was possible as the light distribution over the detector was uniform. The response of a given PMT to the light flash compared to another PMT could be determined. This information was used to flat-field the detector so that data from each PMT could be directly compared.

Data from a Santa Barbara Instrument Group ST-4 CCD were used to calibrate the shaft encoder information in order to accurately determine the pointing of the telescope at all times. At the start of an observation a full frame image of the field of view of the CCD camera, mounted to the telescope, was recorded. The position of the brightest star within the field of view was then tracked and recorded within the data for each recorded event. The 50mm f/1.4 lens allowed guide stars of magnitude $m_v \leq 6$ to be used, providing absolute position sensing better than 0.008°, with a typical integration time of 3 s. The output of the CCD was continuously monitored by a microcomputer, which measured the position and brightness of a nominated guide star within the $2° \times 2°$ field. This was

the brightest star in the field, which could change as the telescope tracked across the sky. During the pre-processing of data, this position was compared with the predicted position of the brightest star from a star catalogue subset for the target source. The attitude of the telescope was reconstructed to an accuracy of 1 arc minute and the Cartesian deviation on the focal plane of the projected source direction from the centre of the detector package was calculated. This was adjusted accordingly for the case of offset tracking mode. The encoder values of azimuth and zenith pointing angles were overwritten in the data file and the x, y deviations were recorded elsewhere within the event data record.

The telescope support structure was made from aluminium, which would deform slightly under the weight of the detector package throughout the course of an observing run depending on its zenith position. As a result, the position of the detector package with respect to the focal point of the mirrors would change. The deformation was found to be reproducible and was measured by monitoring the position of an LED on the detector package with a CCD camera. Deformation associated with the detector packages was accounted for in the steering calculations.

When observing in chopped mode, the on and off fields may have different brightness levels. Hence, there can be different noise levels associated with events recorded from each field. The process of 'software padding' was developed by Cawley et al. (1990) and operates by comparing each PMT in the on and off fields and adding extra noise to the darker pixel until the noise levels are equal (Fegan 1997). This technique was very efficient at removing biases induced by differences in the starlight background without significantly reducing Cherenkov sensitivity. All data taken with the Mark 6 were routinely software padded before analysis.

As there were three detector packages in the Mark 6 system, different noise levels were measured for corresponding PMTs in the Left and Right detector packages during an observation. On comparing the Left and Right detector packages, noise was added to the darker of each pair of corresponding pixels to balance or equalise the noise present in them.

An initial rejection of events too poorly constrained to allow good gamma/hadron separation was performed. In this process any events which were deemed to not be wholly recorded, i.e. where the image was truncated by the central detector package, were removed. This was decided by placing an upper distance cut on the position of the centroid of an ellipse. Small events were removed by placing a minimum on the number of PMTs that must be triggered for an event to be deemed useful. Central events were also removed as they contained insufficient directional information.

To calculate the Hillas parameters (see table 1.1) of an event, it was first necessary to decide which PMTs had sufficient Cherenkov light to merit inclusion. Each PMT was given a weighting, either one or zero. Any tube that was $\geq 37.5\%$ of the brightness of the brightest PMT or $\geq 17.5\%$ of the brightest tube and adjacent to a PMT with a brightness $\geq 37.5\%$ of the brightest PMT was given a weighting of one.

Finally, the information for each event was related to the parameters of an ellipse. The size and orientation of this ellipse with respect to the target position was used to determine Hillas parameters (see section 1.3) to represent each event. This made it possible to analyse the data by selection of events using criteria based on these Hillas parameters. This will be described in more detail in section 6.3.1.

It is worth noting that the Mark 6 system did not have to deal with muon events. For

the telescope to record an event, PMTs in a similar position in all three detectors must be triggered. Muons are a local phenomenon and generally will be detected in only one detector at a time. They were not recorded by the Mark 6 due to its 3-fold spatial trigger system.

6.3 Quality Control Requirements

For data taken in any given observation run to have passed quality control requirements a number of criteria must have been satisfied. These criteria were as follows.

- The sky was clear and stable for the duration of the observation, and
- the raw counting rates in each on-off pair were consistent at the 2.5 σ level

Figures 6.2, 6.3, 6.4 and 6.5 show two separate observations with associated radiometer readings. Figures 6.2 and 6.3 show an observation period where there was obviously intermittent cloud in the field of view, as seen by the rise and fall of the radiometer's digital count output and reflected in the simultaneous fall and rise of the Mark 6 count rate. This observation would not have passed these quality control requirements.

Figures 6.4 and 6.5 show a night where the sky was clear and stable. A reasonably constant radiometer plot is seen, until the very end when some cloud is encountered. This is reflected in the mostly constant count rate of the Mark 6, again until the cloud is encountered towards the end. All but the last observation pair taken on this night would pass this quality control requirement.

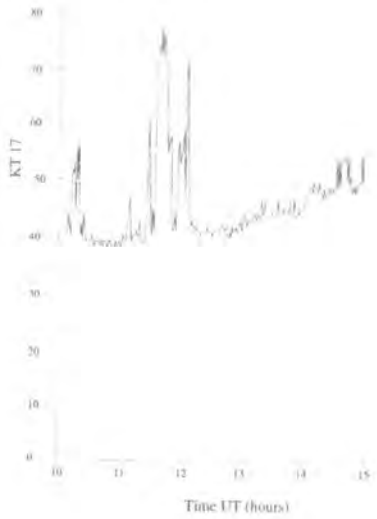

Figure 6.2: Radiometer readings for observations of PKS 0548–322 taken with the Mark 6 on 27th September 1997. The x-axis values are in digital counts. The higher the value, the higher the temperature and therefore the greater the amount of cloud in the field of view. Figure 6.3 shows the simultaneous count rate of events detected with the Mark 6.

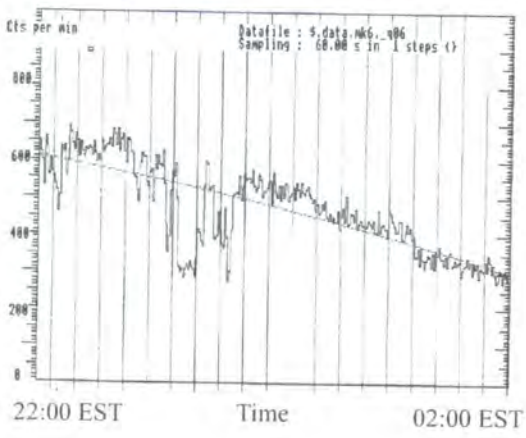

Figure 6.3: The event count rate as detected during observations of PKS 0548–322 taken with the Mark 6 on 27th September 1997, simultaneously with the radiometer readings shown in figure 6.2. The vertical lines mark the division between each on-source or off-source observation segment.

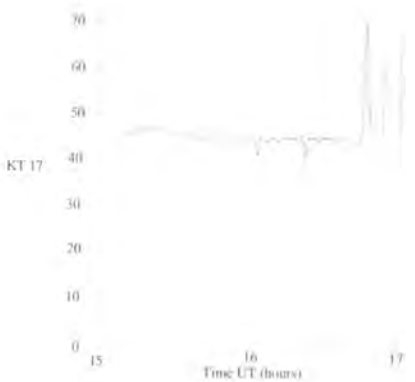

Figure 6.4: The radiometer readings for observations of PKS 2005–489 taken with the Mark 6 on 27th September 1997. The x-axis values are in digital counts. The higher the value, the higher the temperature and therefore the greater the amount of cloud in the field of view. Figure 6.5 shows the simultaneous count rate of events detected with the Mark 6.

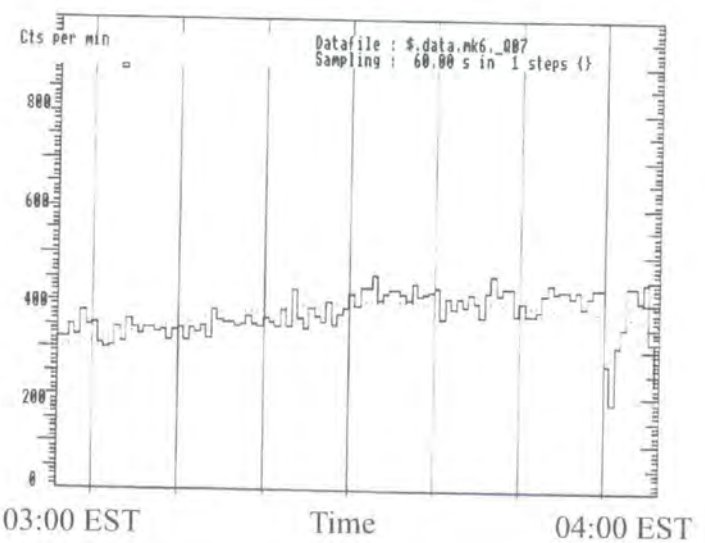

Figure 6.5: The event count rate as detected during observations of PKS 2005–489 taken with the Mark 6 on 27th September 1997, simultaneously with the radiometer readings shown in 6.4. The vertical lines mark the division between each on-source or off-source observation segment.

6.3.1 Event Selection Requirements

Once data had passed the quality control requirements outlined in section 6.3, evidence for a signal was sought. The data were subject to cuts based on Hillas parameter selections as described in tables 6.1 and 6.2.

	Size ranges (digital counts)				
Parameter	500-800	800-1200	1200-1500	1500-2000	2000-10000
Distance (deg)	0.35 - 0.85	0.35 - 0.85	0.35 - 0.85	0.35 - 0.85	0.35 - 0.85
Eccentricity	0.35 - 0.85	0.35 - 0.85	0.35 - 0.85	0.35 - 0.85	0.35 - 0.85
Width (deg)	< 0.10	< 0.14	< 0.19	< 0.32	< 0.32
Concentration	< 0.80	< 0.70	< 0.70	< 0.35	< 0.25
D_{dist}(deg)	< 0.18	< 0.18	< 0.12	< 0.12	< 0.10

Table 6.1: Image parameter selections applied to blazar data recorded at zenith angles less than 45°. The Hillas parameters are defined in table 1.1.

Alpha cuts were determined through simulations of the Mark 6 and optimisation of the PKS2155-304 signal. MOCCA was used to simulate gamma ray and cosmic ray showers, SOLMARK6 was used to simulate the telescope.

The differential spectral index of 2.6 was chosen because at the time the only other known TeV gamma-ray emitting blazars were Mrk 421 and Mrk 501. The spectral index of 2.6 is a reasonable fit to these objects.

	Size ranges (digital counts)			
Parameter	800-1200	1200-1500	1500-2000	2000-10000
Distance (deg)	0.35 - 0.85	0.35 - 0.85	0.35 - 0.85	0.35 - 0.85
Eccentricity	0.35 - 0.85	0.35 - 0.85	0.35 - 0.85	0.35 - 0.85
Width (deg)	< 0.15	< 0.20	< 0.26	< 0.26
Length (deg)	< 0.80	< 0.80	< 0.80	< 0.80
Concentration	< 0.70	< 0.70	< 0.35	< 0.30
D_{dist}(deg)	< 0.25	< 0.08	< 0.08	< 0.08

Table 6.2: Image parameter selections applied to blazar data recorded at zenith angles greater than 45°. The Hillas parameters are defined in table 1.1.

6.3.2 Atmospheric Monitoring

Determination of the state of the atmosphere during observations is essential in the field of ground-based gamma ray astronomy. The atmosphere is an integral part of the detector in ground based Cherenkov astronomy, the effects of which (e.g. atmospheric density profiles and seasonal variations) are discussed in Bernlöhr (2000) and Osborne et al. (2002). Consequently, it is important that any variations in the state of the atmosphere are monitored.

There are several sources of extinction within the atmosphere, including absorption bands of several molecules, Rayleigh scattering, as well as Mie scattering and absorption. All of these factors influence the way in which an EAS propagates through the atmosphere. The brightness of a Cherenkov light flash can be used to determine the primary energy

of the incident photon. Therefore, accurate knowledge of the state of the atmosphere is necessary to fully determine the properties of the EAS caused by an incident gamma ray. It is possible to use this information to determine the primary energy of the incident gamma ray more accurately, and hence improve the energy resolution of the telescope system.

IR Radiometer Readings

An IR–radiometer was used to detect thin cloud in the sky which would otherwise have been difficult to detect with the naked eye. These clouds affect the count rate of the telescope as seen in figure 6.3. The radiometer provides a more sensitive probe of sky clarity than simply relying on the count rate of the telescope, which is limited by statistics, as an indicator of sky clarity and is independent of the telescope itself.

An IR-radiometer operates by integrating radiation between 8 and 14 μm. The detected emission in this range is significantly influenced by emissions due to water vapour present within the 2 degree window through the atmosphere. The measurement can be represented as a radiometric temperature. A clear sky at the zenith has a temperature of between –30 and –70 °C at the location of the Mark 6, depending on the time of year (Buckley et al. 1998). The temperature increases with zenith angle and also with the presence of cloud or other obscuring matter.

Data segments with a poor radiometer trace were rejected from further analysis. For example, if the radiometer trace was seen to vary significantly, indicating intermittent cloud, the data would be considered poor. This instrument provided valuable information on the status of the atmosphere and can be used, in most cases, to explain the variation

of the count rate during observations from the Mark 6.

6.4 Conclusion

Data reduction and quality control of observations is a vital part of any variety of observational astronomy. The Mark 6 data have been subjected to rigorous controls to ensure the high quality of data.

Chapter 7

Observations of PKS 2155–304

This chapter will discuss observations of PKS 2155–304 taken using the University of Durham Mark 6 Telescope between 1996 and 1999 and the relationship between those observations and some contemporaneous X-ray observations.

Very high energy gamma ray emission from PKS 2155–304 has been observed by the Mark 6. This emission was detected in data recorded during 1996 and 1997 when the source was also found to be extremely bright in X-rays. These data were published in Chadwick et al. (1999). In the paper, the level of emission was put at $(4.2 \pm 0.75_{\rm stat} \pm 2.0_{\rm sys}) \times 10^{-11}$ cm^{-2} s^{-1}.

The dataset discussed in this chapter is larger than that published, as there have been more observations of PKS 2155–304, most notably in 1999, since then. The new dataset includes data taken at zenith angles greater than 45° and is analysed in more detail.

7.1 Observation Log

During its lifetime the Mark 6 recorded just under 87 hours of on-source chopped data (see section 6.1.1) and just over 16 hours of offset tracked on-source data from PKS 2155–304 (see section 6.1.2). The observation logs for PKS 2155–304 are given in tables 7.1 and 7.2. Each data segment consists of 14 minutes of observation with another minute allowed for steering the telescope. Each data pair consists of an on-source and an off-source observation segment.

Date (yymmdd)	No. of pairs	Date (yymmdd)	No. of pairs	Date (yymmdd)	No. of pairs	Date (yymmdd)	No. of pairs
960814	6	971020*	3	980721	1	990810	6
960903*	2	971022*	7	980722	2	990811	7
960905*	7	971023*	7	980818	5	990907	7
960906*	5	971025*	3	980819	8	990914	5
960907*	6	971029*	4	980820	4	990915	9
960908*	4	971030*	2	980915	6	990930	1
960909	2	971118*	2	980916	2	991001	1
960910*	8	971119*	4	980917	4	991004	6
960912*	3	971120*	6	980919	8	991005	5
960913	7	971122*	2	981011	4	991007	4
960914*	7	971123*	6	981013	4	991008	8
960915*	7	971124*	7	981016	3	991009	8
960917*	5	971125*	2			991011	8

continued on next page

Table 7.1: *continued*

Date (yymmdd)	No. of pairs	Date (yymmdd)	No. of pairs	Date (yymmdd)	No. of pairs	Date (yymmdd)	No. of pairs
960918*	3					991012	9
961002	3					991104	7
961009*	4					991107	7
961010*	8					991109	8
961012*	5					991110	7
961013*	4					991111	4
961014*	6					991112	3
961015	1						
961102*	3						
961107*	5						
961110*	4						
961111*	5						
961112	5						
961113	3						

Table 7.1: Catalogue of chopped mode observations of PKS 2155–304 with the University of Durham Mark 6 Telescope. The data are listed in columns according to the observing year. Those dates marked with an asterisk were included in the Chadwick et al. (1999) paper.

Date (yymmdd)	Number of segments
990908	23
990911	23
990913	23

Table 7.2: Catalogue of offset tracking mode observations of PKS 2155-304 made with the University of Durham Mark 6 Telescope.

Figures 7.1 and 7.2 show the variation in cosmic ray rate as observed by the Mark 6. These data were taken between 25° and 35° in zenith. Data taken between 30° and 35° in zenith were increased, according to an empirical zenith angle dependance, to equivalent levels between 25° and 30° in zenith. The cosmic ray rate is seen to decrease in 1999 (most notable in figure 7.2). This is an indication that the sensitivity of the telescope decreased towards the end of its lifetime.

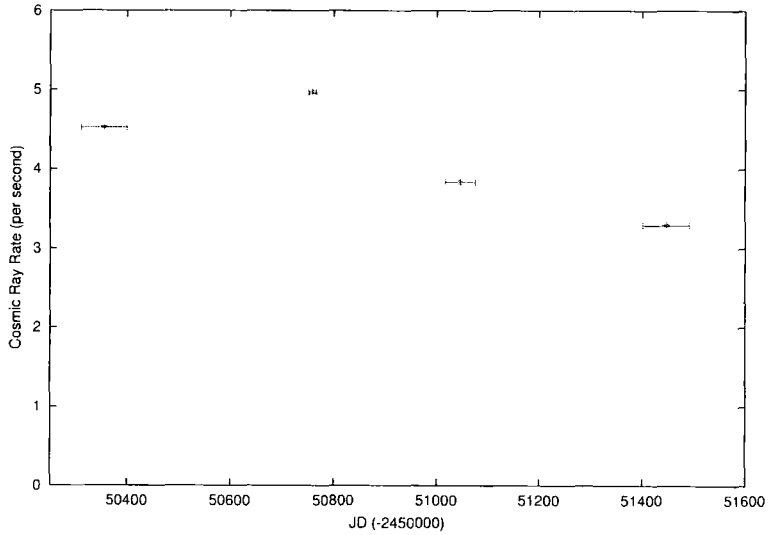

Figure 7.1: The yearly variation of observed cosmic ray rate in observations of PKS 2155–304 between 1996 and 1999.

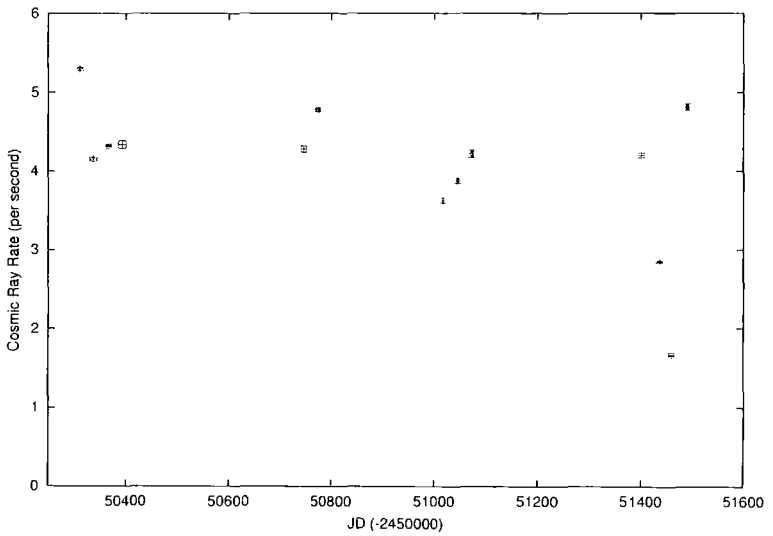

Figure 7.2: The monthly variation of observed cosmic ray rate in observations of PKS 2155–304 between 1996 and 1999.

7.2 Methods of Analysis

As outlined in section 1.3.1, *alpha* plots and levels of significance (see equation 1.6) are used to determine if there is gamma ray emission from a source and the level of this emission, if present.

7.2.1 The Entire Dataset

Table 7.3 shows the number counts present in the dataset at various stages through the analysis procedure.

Figure 7.3 shows the *alpha* plot for the entire chopped mode, Mark 6, PKS 2155–304 dataset. A significant on-source excess of events can be seen in the first two data bins followed by a fall off in the excess to a statistical insignificance, as expected for observations of a gamma ray emitting source. The significance for emission from this

State	N_{on}	N_{off}	$N_{on} - N_{off}$	Significance (σ)
Tidied events	866,231	864,686	1,545	1.2
Shape selected events	56,947	55,870	1,077	3.2
Events with *alpha* $< 22.5°$	9,500	8,624	739	5.4

Table 7.3: Results of various event selections for PKS 2155–304 at all zenith angles. Note: Tidied events are those that are based on information from a minimum of two PMTs and are constrained within the camera

dataset is 5.4 σ for *alpha* $< 22.5°$ i.e. calculated from the excess in the first three *alpha* bins. This represents an overall positive detection of gamma ray emission from PKS 2155–304.

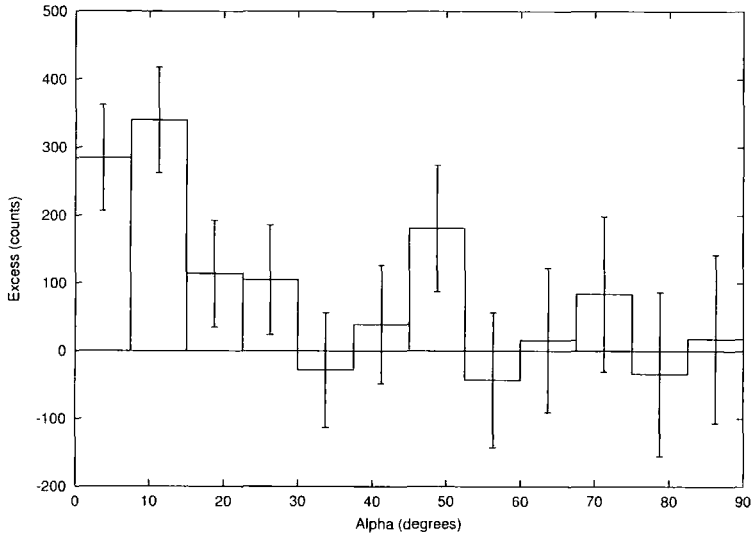

Figure 7.3: The *alpha* plot for the entire 1996–1999 PKS 2155–304 data, containing just under 87 hours of on-source observations at all zenith angles.

However, blazars are known to flare on varying timescales from the order of minutes to years. Therefore, if a large dataset is examined, any short timescale flares in the emission may be lost. Similarly, if too small a dataset were examined any long timescale

variations or persistent low level emission would not be apparent, as the chances of finding a significant excess of on-source events in small datasets are greatly reduced. To account for this, different sized data subsets were examined, ranging from the entire dataset to data from a single night.

7.2.2 Yearly Subsets

The origin of the signal within the dataset needed to be determined more specifically. To this end, the dataset was split initially into four subsets based on the year in which the observations were made. As can be seen in table 7.1, there are more observations in some years than in others. PKS 2155–304 was most frequently observed in 1996 with a total of just under 30 hours of on-source observations compared with 1998 where there were just under 12 hours of on-source observations.

Figure 7.4 shows the *alpha* plots for each individual year. It can be seen that the signal apparent in figure 7.3 is mainly due to observations taken in 1996 and 1997 with some contribution from 1999. The small amount of data taken in 1998 ($\sim$ 12 hours) makes it difficult to determine whether or not PKS 2155–304 was emitting gamma rays during this time. X-ray evidence suggests that PKS 2155–304 was in a high state at this time in 1998 (see section 7.7). It is worth noting that the predicted number of on-source and off-source events is similar to that recorded in 1996, observing time being equal. This implies that the telescope's sensitivity was at a similar level in 1996 and 1998. Therefore, if the source were emitting at the same level as it was during 1996, ten times more excess events would have been recorded.

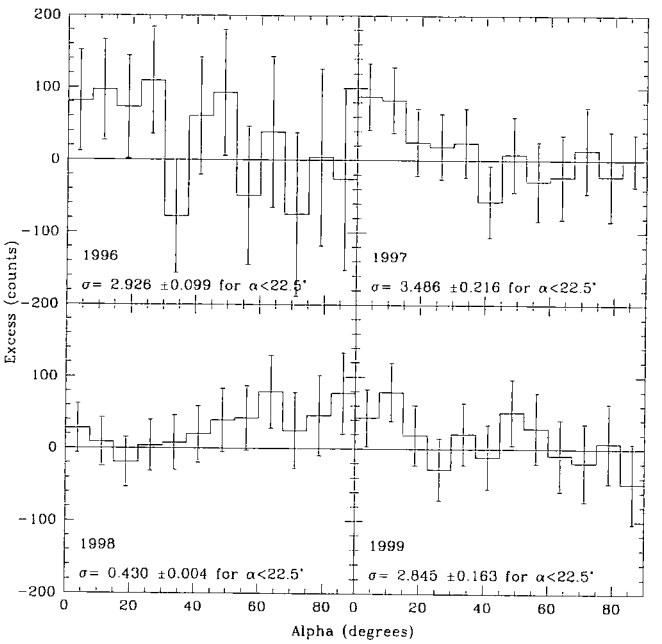

Figure 7.4: The *alpha* plots for individual years 1996 through 1999 for PKS 2155–304. Note: Errors are one standard deviation of N_{ON} and N_{OFF}, the larger errorbars in the 1996 quadrant reflect the fact that there are ~ 4 times more events recorded in this year than in any other.

7.2.3 Monthly Subsets

By breaking down the dataset into further subsets, the origin of the signal may be further located. Figures 7.5 and 7.6 show the *alpha* plots for individual months' observations during 1996 and 1997, respectively. Evidence for gamma ray emission can be clearly seen in September 1996, November 1997 and October 1997. There is no significant excess of on-source events seen in observations during August ($\sim$ 1.4 hours observations), October and November 1996. This could, however, be due to the decreased size of the dataset.

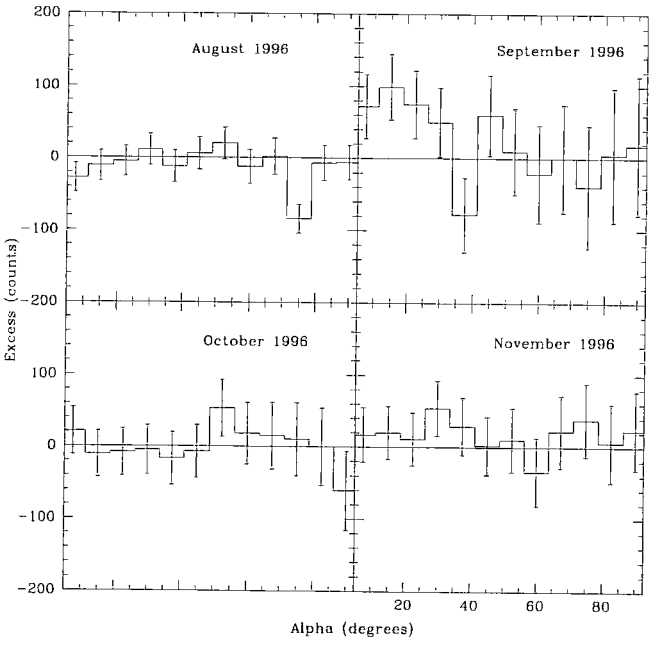

Figure 7.5: Shows the *alpha* plots for individual months in 1996 for PKS 2155–304.

The September 1996 observations were longest (just over 14 hours of on-source data) and show the greatest excess. The significance for emission from the September 1996 subset is 4.2 σ. October and November 1996 observations do not show a significant excess at low *alpha* values. Datasets are becoming so small that a signal would become lost in

the statistics.

There is, however, evidence for variability in the 1996 dataset. The greatest emission is seen in September 1996. If this level of emission were to be maintained by the source throughout October and November (accounting for the different amounts of on-source data) there would have been a total of 91 excess events in October and 112 excess events in November recorded where only 4 and 66 were actually observed, respectively. This would have represented 2.6σ and 2.9σ signals where only 0.1σ and 1.3σ signals were detected. The significance of this difference is $\sim 1.5\sigma$. The number of off-source events recorded were comparable for the September, October and November observations, supporting the evidence for variability of gamma ray emission from PKS 2155–304.

On comparing the monthly excess number count values to the monthly average (weighted to account for different observation times) for all observations, September, and November 1996, October and November 1997, September 1998 and September 1999 had excesses above the average.

The October and November 1997 datasets both show significant excesses at low *alpha* as seen in figure 7.6. The individual significances are 2.2 σ for October 1997 and 3.9 σ for November 1997.

Figure 7.7 shows the monthly gamma rays per cosmic ray rate for PKS 2155–304 as observed by the Mark 6, where;

$$\text{Gamma rays per cosmic ray} = \frac{N_{on} - N_{off}}{N_{off}} \tag{7.1}$$

The gamma rays per cosmic ray rate can be a useful way of looking at data as it accounts for the level of the off-source field and allows the direct comparison of datasets

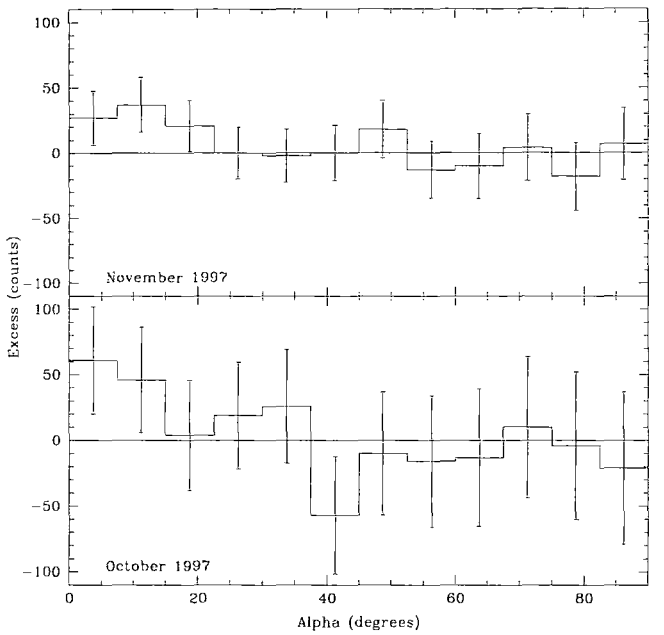

Figure 7.6: Shows the *alpha* plots for individual months in 1997 for PKS 2155–304.

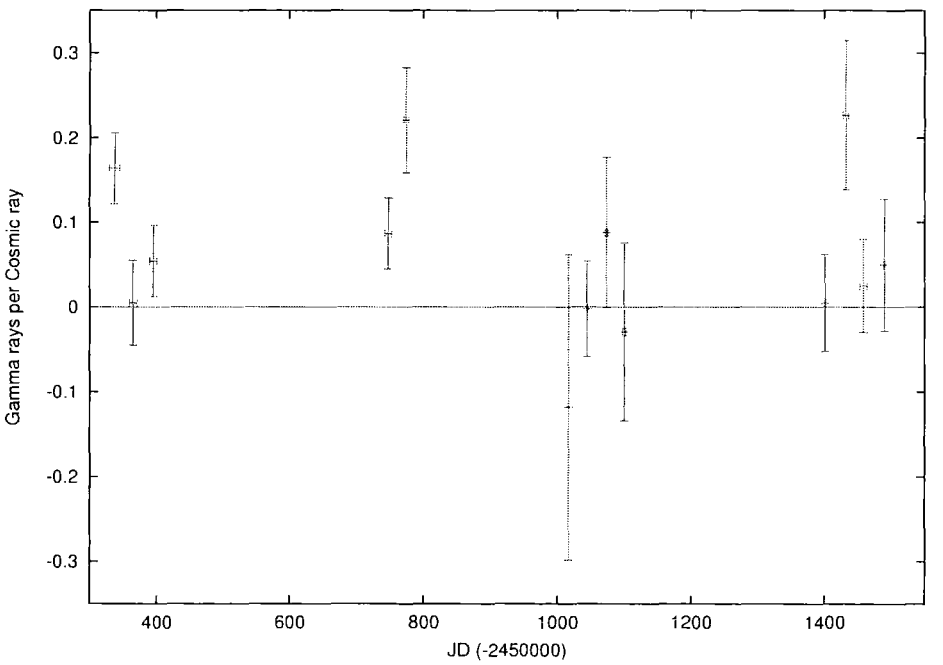

Figure 7.7: The monthly values of gamma rays per cosmic ray for PKS 2155–304 from 1996 to 1999.

with different durations.

7.2.4 Individual Nights

Another way to interpret gamma ray data is by looking at the number of gamma rays per cosmic ray present in a given observing night.

It may be clearer to examine this gamma rays per cosmic ray data on a yearly basis also, as shown in figures 7.8, 7.9, 7.10 and 7.11. In order to check that there were no biases present in the gamma rays per cosmic ray data, a plot of the distribution of the value of the gamma rays per cosmic ray rate was made and can be seen in figure 7.12. The distribution approximates a gaussian distribution centered around 0.15, indicating no bias. If a bias were present, the distribution would be non-gaussian.

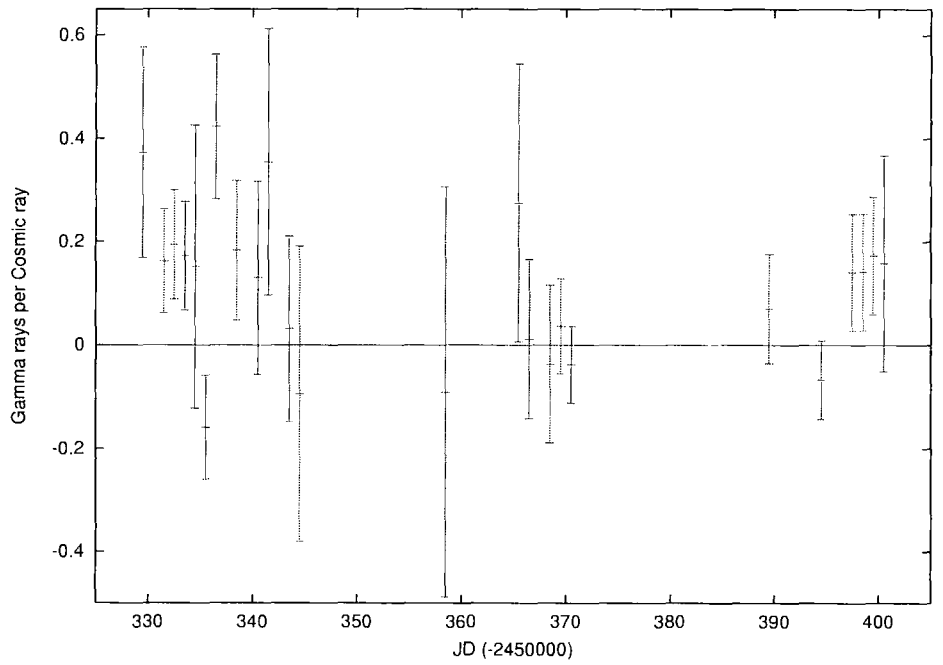

Figure 7.8: Gamma rays per cosmic ray for PKS 2155–304 in 1996.

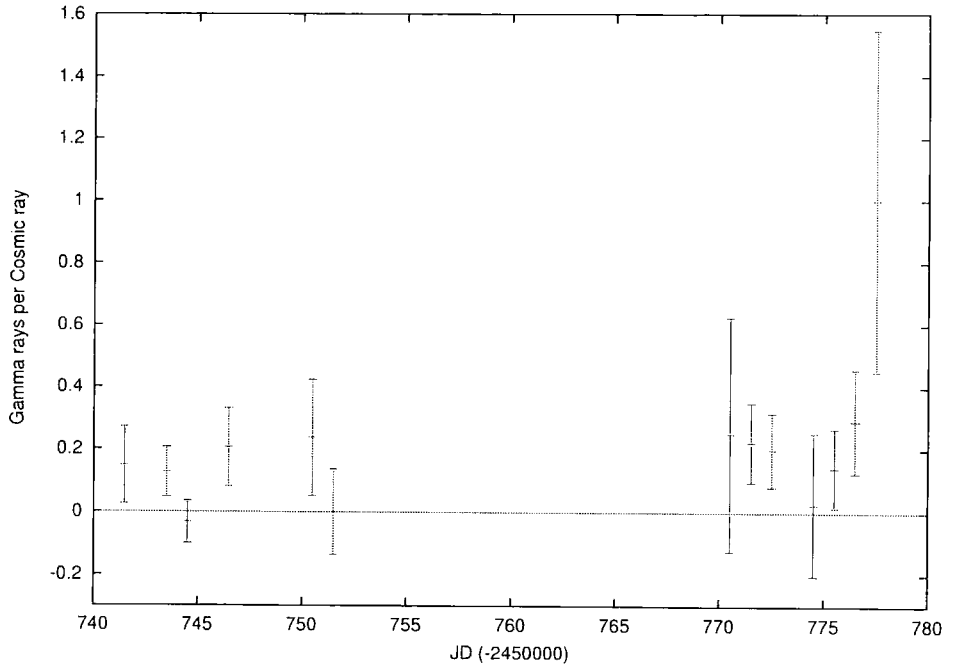

Figure 7.9: Gamma rays per cosmic ray for PKS 2155–304 in 1997.

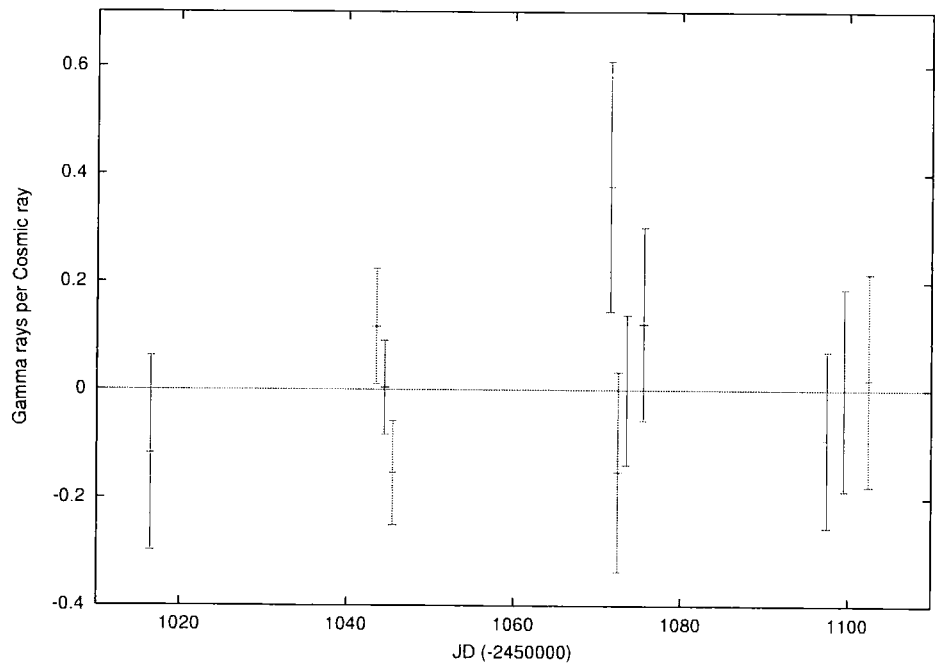

Figure 7.10: Gamma rays per cosmic ray for PKS 2155–304 in 1998.

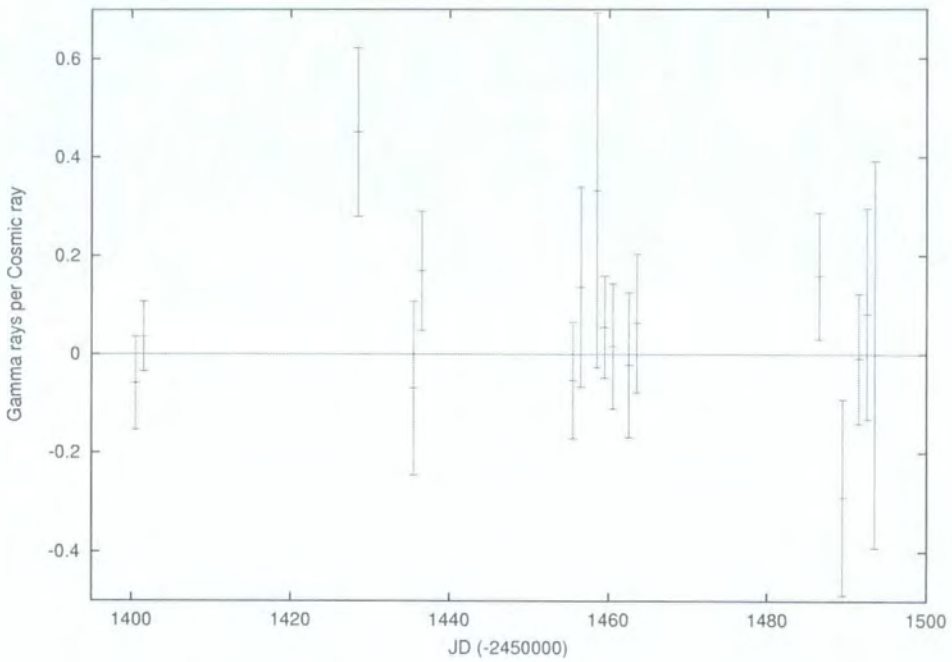

Figure 7.11: Gamma rays per cosmic ray for PKS 2155–304 in 1999.

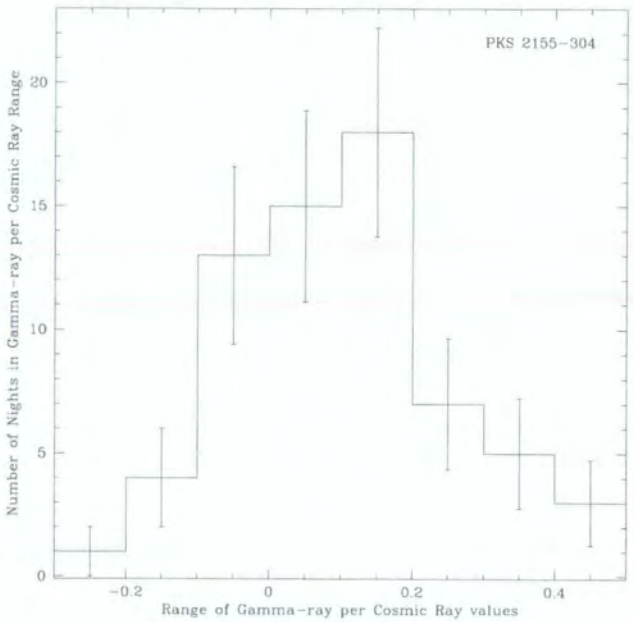

Figure 7.12: Distribution of gamma rays per cosmic ray for the entire PKS 2155–304 dataset.

7.3 The 1999 Data Subset

These data will be discussed separately from the rest of the data as they represent the greatest addition to the dataset from what has already been published. Most PKS 2155–304 observations in 1999 were taken in chopped mode (see section 6.1.1). However, during 1999, the Durham group experimented with a new mode of observing objects – offset tracking mode, as discussed in section 6.1.2.

It was noted that the overall count rate of the Mark 6 decreased over its lifetime. On comparing two similar (environmental conditions, time of year, observed object) nights, by 1999, the count rate had decreased by over 50% compared to previous years. This may have been to due to the age and wear of the PMTs. Initial tests carried out at the University of Durham on the PMTs indicate that they had indeed degraded. Other factors such as degradation of mirror performance may also have contributed to the fall in count rate. Unfortunately, the Mark 6 was decommissioned before the nature of the degradation could be fully investigated.

7.3.1 Offset Tracked Mode Data

There were only three nights of observations in this mode listed in table 7.2, amounting to 17 hours of observations with PKS 2155–304 in the field of view. No evidence for a signal was found in this dataset.

The average X-ray flux from PKS 2155–304 in 1999 was at a similar level to what it was in 1996, implying that if the same physical processes were at work in the source, gamma ray emission should be detectable from PKS 2155–304 at this time. It may be

that the apparent reduction in telescope sensitivity was the cause of this difference.

These data were not discussed in conjunction with the rest of the data as there was no distinct control exposure associated with them and the event selection used to identify gamma rays was slightly different as outlined in section 6.1.2.

7.3.2 Chopped Mode Data

There were 28 hours of data taken in chopped mode during 1999. Figure 7.13 shows the monthly *alpha* plots for PKS 2155–304 during 1999. Figure 7.14 shows a false

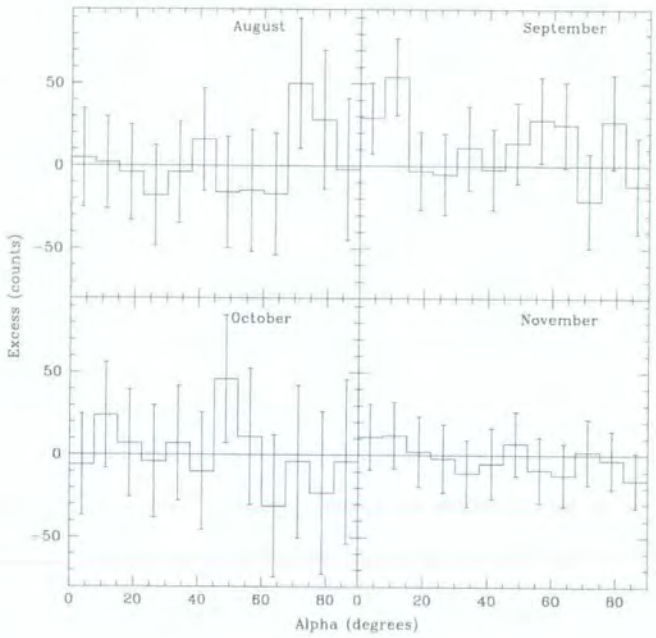

Figure 7.13: Monthly *alpha* plots of chopped observations of PKS 2155–304 during 1999.

source analysis plot (see section 1.3.2) for the PKS 2155–304 1999 data set. The results show no evidence for emission from PKS 2155–304 during 1999. The 3σ upper limit for emission was determined to be $5.3 \times 10^{-12}\text{cm}^{-2}\text{s}^{-1}$ for energies > 0.7 TeV from the 1999

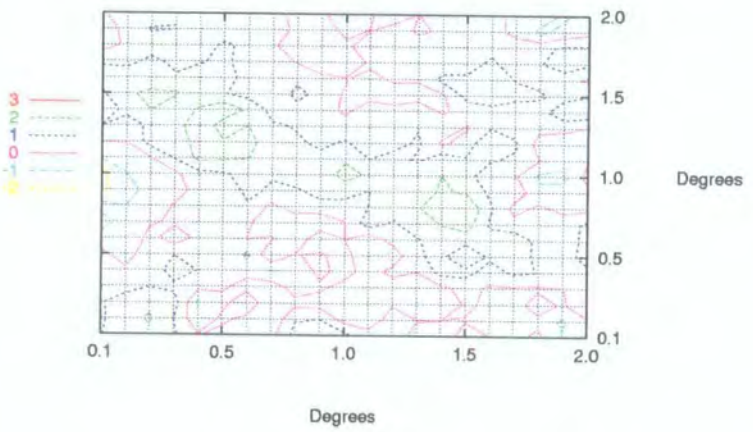

Figure 7.14: False source analysis plot of the chopped 1999 data only (section 1.3.2) in the field of view of the detector. The values indicate the significance (σ) at a particular point in the field of view, with no correction for the number of false source positions considered.

dataset. The upper limit is calculated using an energy threshold of > 0.7 TeV, which was determined by simulations based on the detection of PKS 2155–304 in 1996 and 1997.

It is not unreasonable to expect that the energy threshold would have increased by 1999 due to decreased sensitivity of the Mark 6. An estimate of this decrease was calculated by comparing pre-1999 observations with 1999 observations. The criteria for selection was that the nights were on the same date in both years, so that the source would follow the same path along the sky on both nights and observations were recorded under clear and stable weather conditions. A total of 5 pairs of nights were used in this analysis and off-source tided number counts were used. It was estimated that the energy threshold of the Mark 6 was 1.5 ± 0.1 TeV by 1999.

7.4 Lightcurves

Lightcurves of observations of PKS 2155–304 are shown in figures 7.15, 7.16, 7.17 and 7.18 for each observing year from 1996 through 1999. Figure 7.19 shows the lightcurve for PKS 2155–304 using upper limits calculated on a monthly basis.

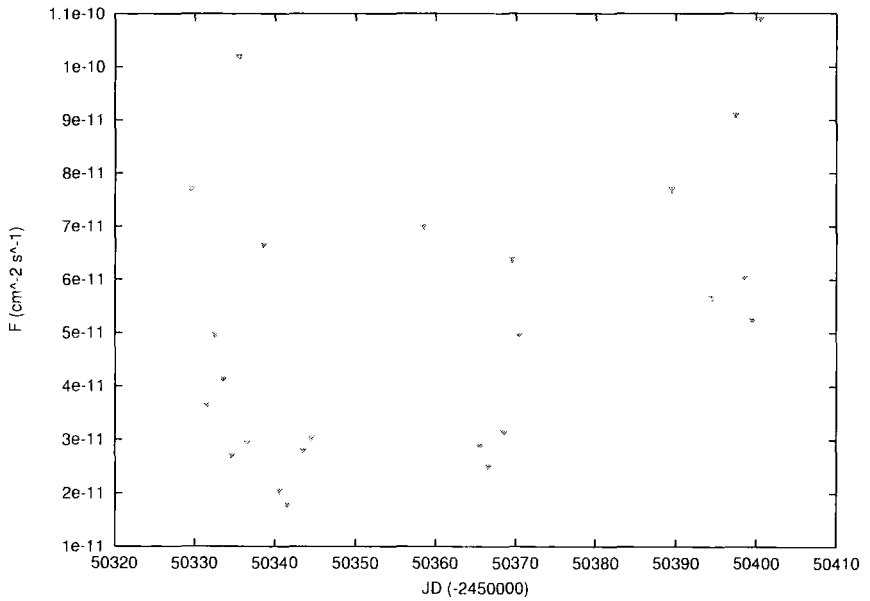

Figure 7.15: A lightcurve for observations of PKS 2155–304 in 1996. All points represent 3σ upper limits.

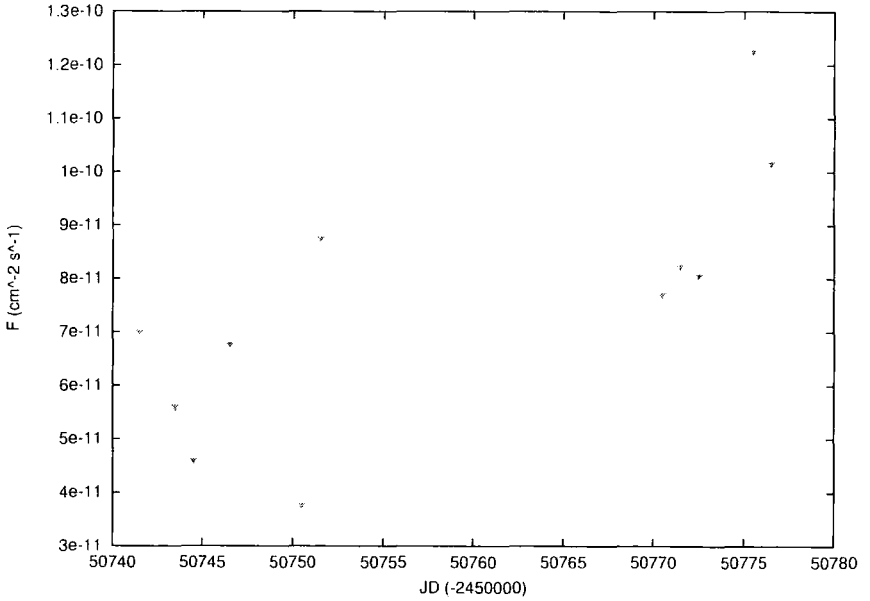

Figure 7.16: A lightcurve for observations of PKS 2155–304 in 1997. All points represent 3σ upper limits.

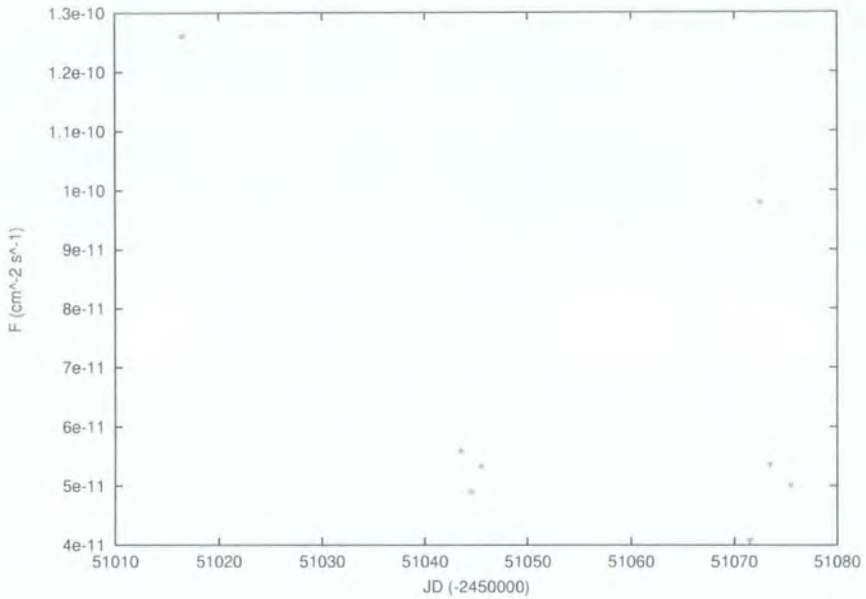

Figure 7.17: A lightcurve for observations of PKS 2155–304 in 1998. All points represent 3σ upper limits.

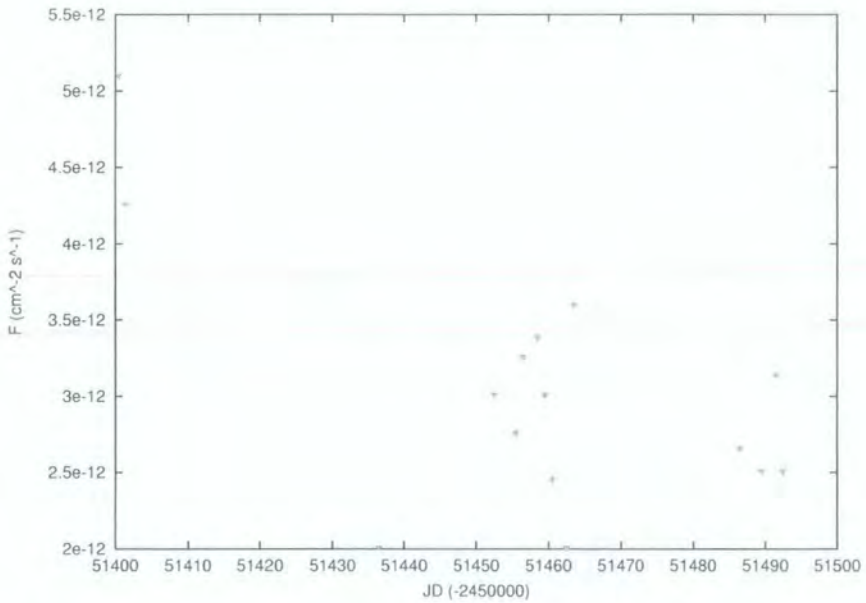

Figure 7.18: A lightcurve for observations of PKS 2155–304 in 1999. All points represent 3σ upper limits. The sensitivity and energy threshold of the Mark 6 decreased so this data has been extrapolated to E> 700GeV so that it may be compared to data from 1996 to 1998.

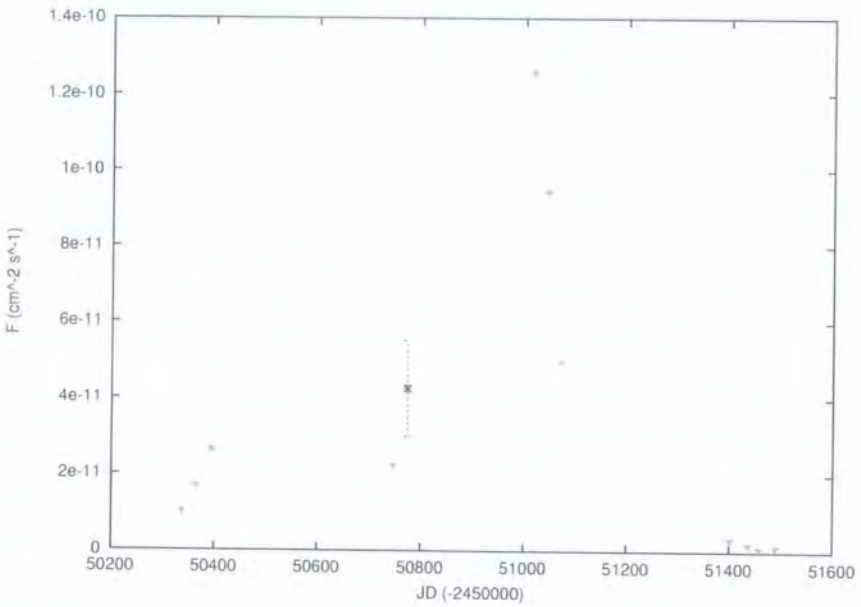

Figure 7.19: A lightcurve for monthly observations of PKS 2155–304 from 1996 to 1999. All points represent 3σ upper limits except the 3 sigma detection observed in November 1997 (point with errorbars).

7.5 Sources of Error

7.5.1 Statistical Errors

These are simple Poissonian errors. For example in the case of N_{ON}, the statistical error is simply $\sqrt{N_{ON}}$.

7.5.2 Systematic Errors

Rayleigh scattering, ozone scattering and aerosol scattering are liable to introduce a significant source of error at Cherenkov wavelengths. Rayleigh scattering is the dominant mechanism and is governed by the column density of the atmosphere over the telescope location, which is related to barometric pressure.

Although the majority of ozone in the atmosphere is at altitudes greater than shower maximum, ozone extinction will still be significant at lower altitudes and will reduce transmission for wavelengths below $\sim$ 300 nm. Aerosol scattering in the lower layers of the atmosphere will introduce light attenuation, which will be highly variable given the constantly changing aerosol density.

As, the Mark 6 was sited at a relatively low altitude (260m above sea level) aerosol concentration was likely to have a large effect on the observed count rate.

Nolan (2002) describes the overall systematic errors affecting the Mark 6 observations. There is a 10% error due to atmospheric attenuation and a 15% error due to differences in telescope simulations using various codes.

7.6 A Search for Variability

7.6.1 The t-test

A t-test was carried out on two samples of PKS 2155–304 data. The first sample consisted of the 1996 and 1997 data in daily gamma rays per cosmic ray form. The second sample consisted of the 1998 and chopped 1999 data also in daily gamma rays per cosmic ray form. The test was performed to determine whether or not the two samples were likely to be from the same parent population. If it were shown that both samples were likely to be from the same parent population, this would imply that the Mark 6 observations were simply sampling from a constantly emitting source. If not, this would imply that the samples were taken from a variable source. The value of t is calculated by the following

equation:

$$t = \frac{\bar{x} - \bar{y}}{\sqrt{\frac{var_x}{n_x} + \frac{var_y}{n_y}}} \tag{7.2}$$

where $\bar{x}$ is the mean value of x, $\bar{y}$ is the mean value of y, var_x is the variance of x, var_y is the variance of y, n_x is the number of values of x and n_y is the number of values of y. This gives $t = 2.46$, with in this case, 63 degrees of freedom. These values may be used

	Mean	Variance	n
1996/1997	0.15	0.04	37
1998/1999	0.04	0.03	28

Table 7.4: Values used to calculate t in the t-test.

to determine the significance of the initial hypothesis in t-test tables.

The results of the t-test showed that there was only a 1% chance that both samples were from the same parent population. It is possible that this significant change is due to PKS 2155–304 being a variable source and that it was in a different state in 1996/7 than in 1998/9 and it is possible that the change is due to the change in response of the telescope.

7.6.2 χ^2 Test

The χ^2 test was performed on the dataset again in gamma rays per cosmic ray format to search for variability on a daily scale. χ^2 is calculated using the following equation:

$$\chi^2 = \left(\sum_i^n \frac{\bar{x} - x_i}{\sigma}\right)^2 \tag{7.3}$$

$$\text{Reduced } \chi^2 = \frac{\chi^2}{\text{Number of Degrees of Freedom}}$$

where x_i is the gamma rays per cosmic ray value, $\bar{x}$ is the mean gamma rays per cosmic ray value and σ is the standard deviation.

Period	Mean (grpcr)	χ^2	Degrees of Freedom	Reduced χ^2
1996	0.11	29.71	23	1.29
1997	0.22	20.78	10	1.73
1998	0.01	8.50	12	0.85
1999	0.06	14.32	16	0.89
All years	0.10	73.94	64	1.16

Table 7.5: Results of a χ^2 search for variability in PKS 2155–304.

If the source was constant, the reduced χ^2 value would be ~ 1. As seen in table 7.5, there is no strong evidence for variability.

The t-test and χ^2 test give marginally inconsistent results. However, in neither case is the evidence for or against variability particularly strong. A more detailed variability examination will be possible with the more sensitive new generation of gamma ray telescopes such as H.E.S.S. and CANGAROO III that will record higher event count rates.

7.7 X-ray Observations of PKS 2155–304

Two X-ray satellites observed PKS 2155–304 between 1996 and 1999, RXTE and BeppoSAX. Some of these observations are discussed in this section.

7.7.1 Rossi X-ray Timing Explorer

The Rossi X-ray Timing Explorer (RXTE) was launched on 30th December 1995. RXTE features unprecedented time resolution in combination with moderate spectral resolution to explore the variability of X-ray sources. Timescales from microseconds to months are covered in an instantaneous spectral range, 2 – 250 keV.

The All Sky Monitor (ASM) consists of 3 scanning shadow cameras on one rotating boom with a total net effective area of 90 cm^2. The ASM operates in the 2–10 keV range and rotates in such a way as to scan most of the sky every 1.5 hours, including targeted observations of a number of the brightest X-ray sources. This gives observers the opportunity to spot any new phenomenon quickly and to develop a flux variability record on a number of sources, PKS 2155–304 included.

7.7.2 RXTE Observations

Figures 7.20, 7.21, 7.22 and 7.23 show the RXTE ASM observations of PKS 2155–304 in the years 1996, 1997, 1998 and 1999 respectively. Note that the vertical sum band intensity scale is different for each year. There were pointed RXTE observations of PKS 2155–304 in 1997 (see section 5.2.5). Both ASM and pointed observations give similar results, within errors.

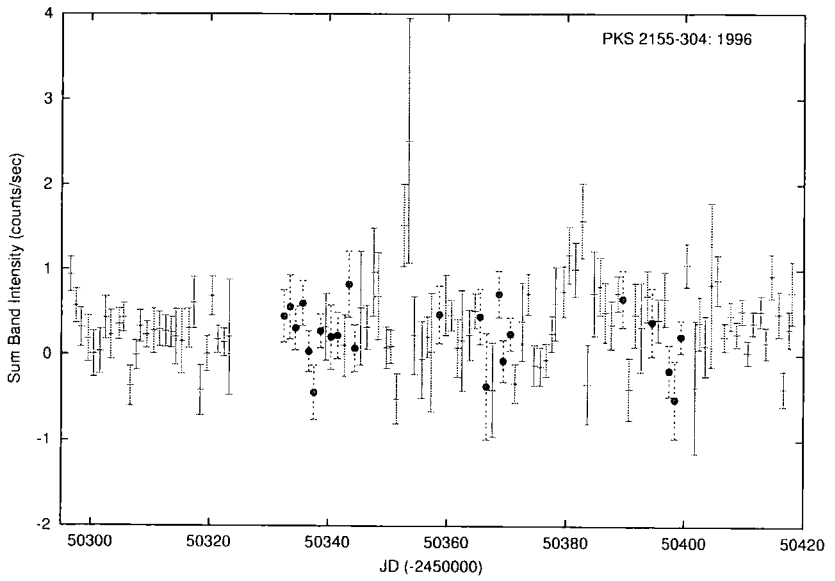

Figure 7.20: RXTE ASM one day averages for PKS 2155–304 in 1996. The solid black circles indicate that the Mark 6 was observing at this time.

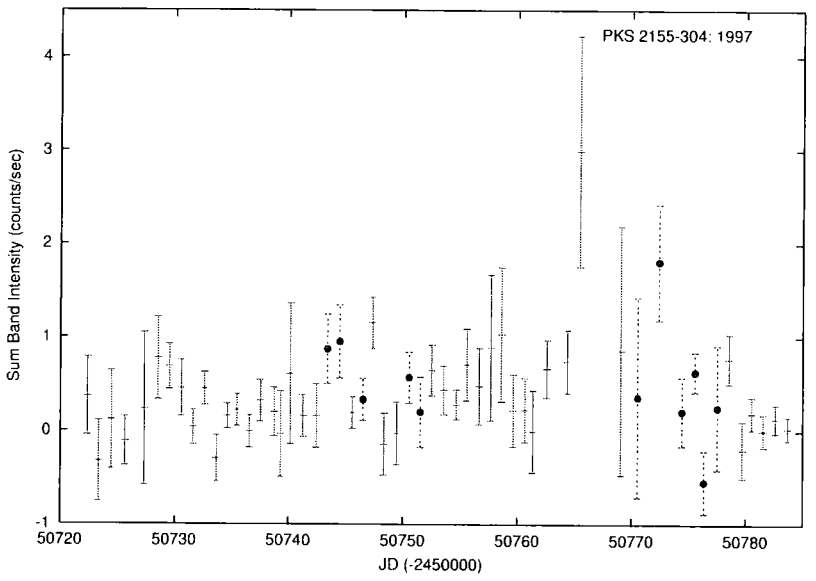

Figure 7.21: RXTE ASM one day averages for PKS 2155–304 in 1997. The solid black circles indicate that the Mark 6 was observing at this time.

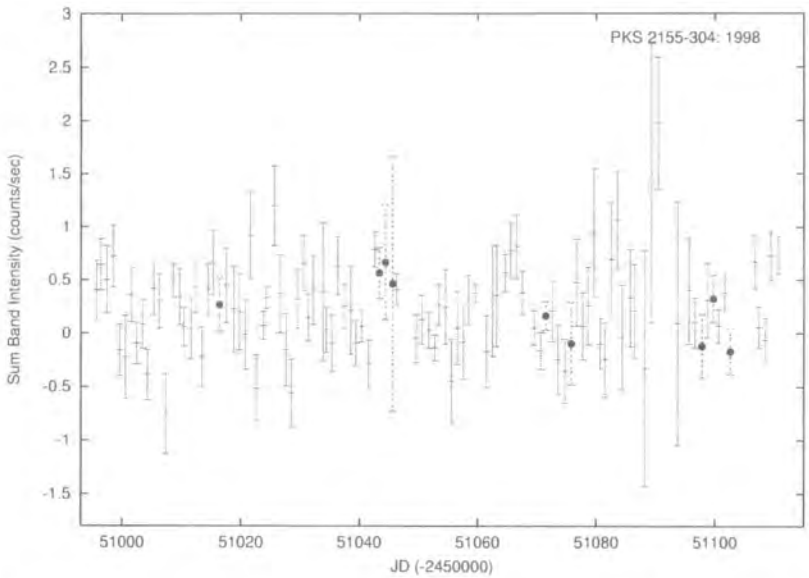

Figure 7.22: RXTE ASM one day averages for PKS 2155–304 in 1998. The solid black circles indicate that the Mark 6 was observing at this time.

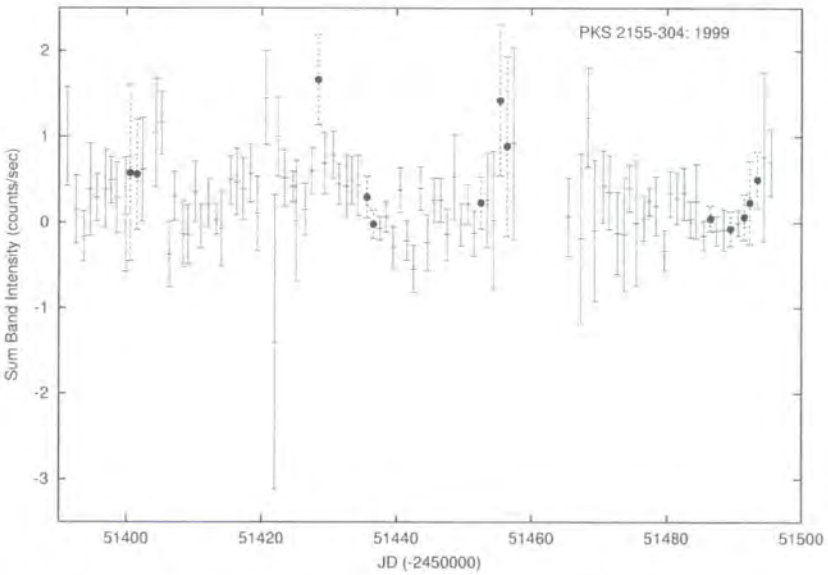

Figure 7.23: RXTE ASM one day averages for PKS 2155–304 in 1999. The solid black circles indicate that the Mark 6 was observing at this time.

The Correlation Co-efficient

To determine how well a set of measurements x and y are correlated, a correlation co-efficient can be calculated. The linear correlation coefficient, r, is a number between -1 and 1 and measures how close to a straight line a set of points are. A correlation coefficient of zero corresponds to no correlation. r can be evaluated using the relation:

$$r = \frac{\sigma_{xy}}{\sigma_x \sigma_y} \tag{7.4}$$

where σ_x and σ_y are the standard deviations for x and y respectively and σ_{xy} is the covariance between the two datasets.

PKS 2155–304 is monitored almost daily by the ASM onboard RXTE. As was outlined in chapter 4, certain models for blazar emission predict that the X-ray and gamma ray emission are correlated. The observed ASM flux values were plotted against the Mark 6 gamma rays per cosmic ray values in order to see if there was any correlation.

Figure 7.24 shows a graph of the value of gamma rays per cosmic ray versus the RXTE ASM one day average intensity values for PKS 2155–304. The correlation coefficient was found to be -0.056 for the entire PKS 2155–304 dataset, meaning that the Mark 6 data is very poorly correlated to the X-ray data. This may be due to a lack of statistics. However, it is worth noting that the X-ray flux of PKS 2155–304 was at its highest when it was observed in TeV gamma rays with the Mark 6.

7.7.3 BeppoSAX

The BeppoSAX satellite was the first X-ray mission to cover more than three decades of energy, from $0.1 - 300$ keV, with a relatively large area, a medium energy resolution

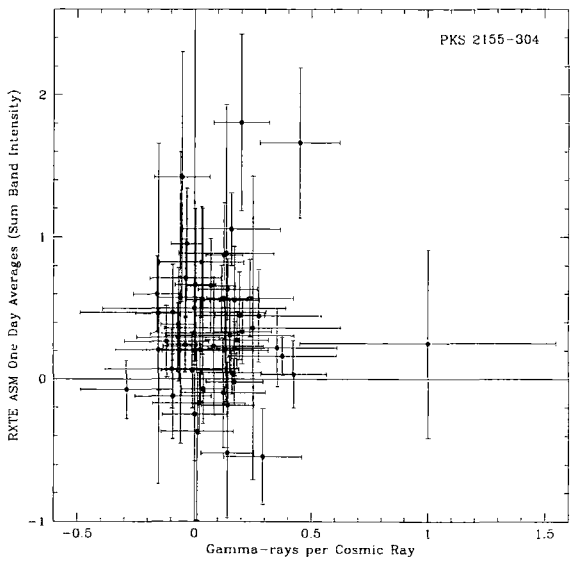

Figure 7.24: Correlation between the daily rate of gamma rays per cosmic ray and the RXTE ASM One Day Average Intensity Values for PKS 2155–304.

and imaging capabilities in the range of $0.1 - 10$ keV. The Medium Energy Concentrator Spectrometers (MECS) operated in the $1.3 - 10$ keV range and comprised a set of three identical grazing incidence telescopes with double cone geometry, with position sensitive gas scintillation proportional counters in their focal planes. The Low Energy Concentrator Spectrometer (LECS) was a low energy ($0.1 - 10$ keV) telescope, identical to the other three, but with a thin window position sensitive gas scintillation proportional counter in its focal plane.

There are observations of PKS 2155–304 taken using BeppoSAX almost contemporaneous with Mark 6 observations of PKS 2155–304 (see section 7.7.4).

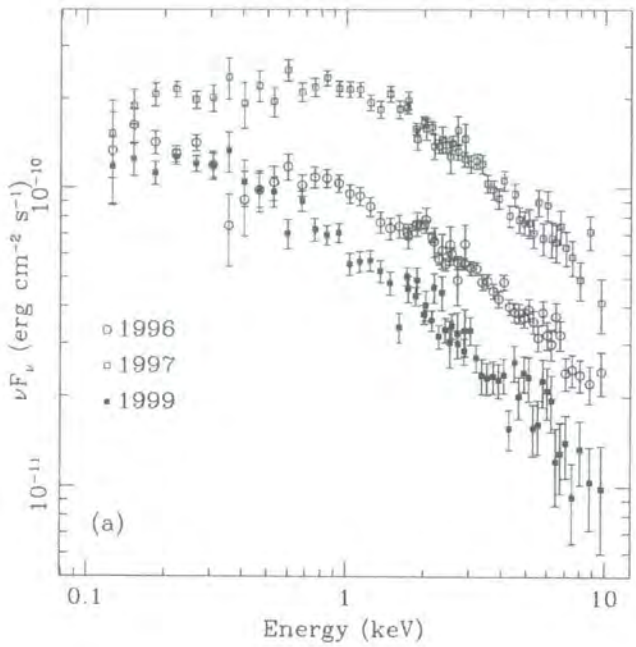

Figure 7.25: BeppoSAX Observations of PKS 2155–304 in 1996, 1997 and 1999 (Zhang et al 2002).

7.7.4 BeppoSAX Observations

It can be seen in figure 7.25 that PKS 2155–304 was most bright in $0.1 - 10$ keV X-rays in 1997 when it was also observed in VHE gamma rays by the Mark 6.

Figures 7.26 and 7.27 show BeppoSAX observations of PKS 2155–304 in 1997 and 1999 respectively. It is worth noting that PKS 2155–304 was about 5 times brighter in $0.1 - 2$ keV X-rays and about 3 times brighter in $2 - 10$ keV X-rays in 1997 than in 1999.

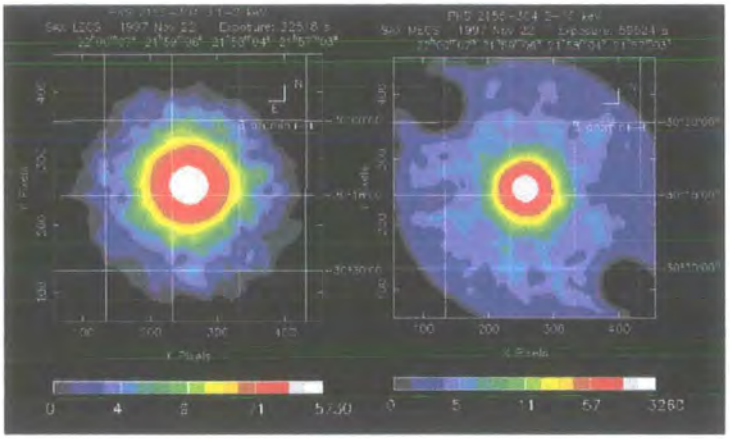

Figure 7.26: BeppoSAX Observations of PKS 2155–304 on 22 November 1997. The image was obtained from the BeppoSAX public archive (BeppoSAX archive 2003).

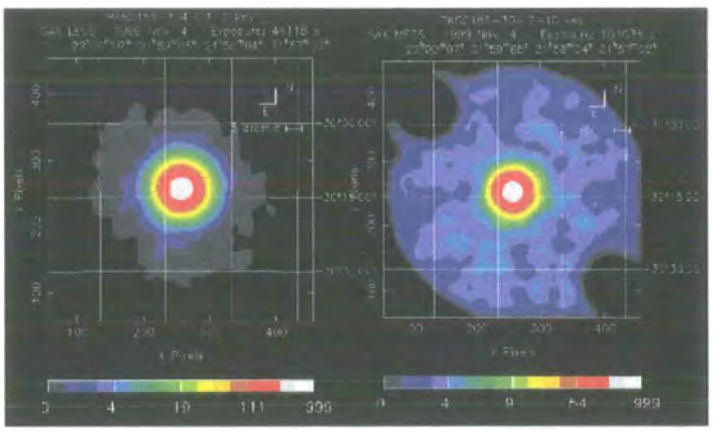

Figure 7.27: BeppoSAX Observations of PKS 2155–304 on 04 November 1999. The image was obtained from the BeppoSAX public archive (BeppoSAX archive 2003).

7.8 Infrared Background Absorption in the Context of PKS 2155–304

As described in section 4.5, very high energy gamma rays from blazars may be absorbed by IR photons. This effect will, of course, be greater at larger redshifts.

When first detected, PKS 2155–304 was the most distant source of TeV photons known at $z = 0.116$. More recently, gamma rays were observed from H 1426+428 with $z = 0.129$ (Aharonian et al. 2002). Observations of H 1426+428 were in good agreement with models for infrared background absorption.

Spectral studies by Nolan (2002) give a gamma ray spectrum of PKS 2155–304 based only on two energy points which are consistent with a power law of index 3.2 ± 0.9. In figure 7.28 it is shown that if power law with spectral index 2.6 were taken as the intrinsic spectrum of the AGN, the steepening due to absorption by a reasonable model of the IR background would be small compared to the observational uncertainty in the spectrum.

Stecker & de Jager (1997) presented a model to predict the intergalactic gamma ray pair production absorption coefficient, as a function of energy and redshift (up to $z = 0.54$). Their model used COBE results, theoretical models of the galactic spectral energy distribution of the intergalactic infrared background field (IIRF) together with estimates of the IIRF from galaxy counts. The results of their model were tested against observations of the spectrum of Mrk 421, including HEGRA observations.

The expected reduction in flux due to absorption of gamma rays from PKS 2155–304 is by a factor of $\sim e^{-1}$, based on models by Stecker & de Jager (1997) of 0.7 TeV emission from a source at $z = 0.1$. However, with new experiments such as H.E.S.S.

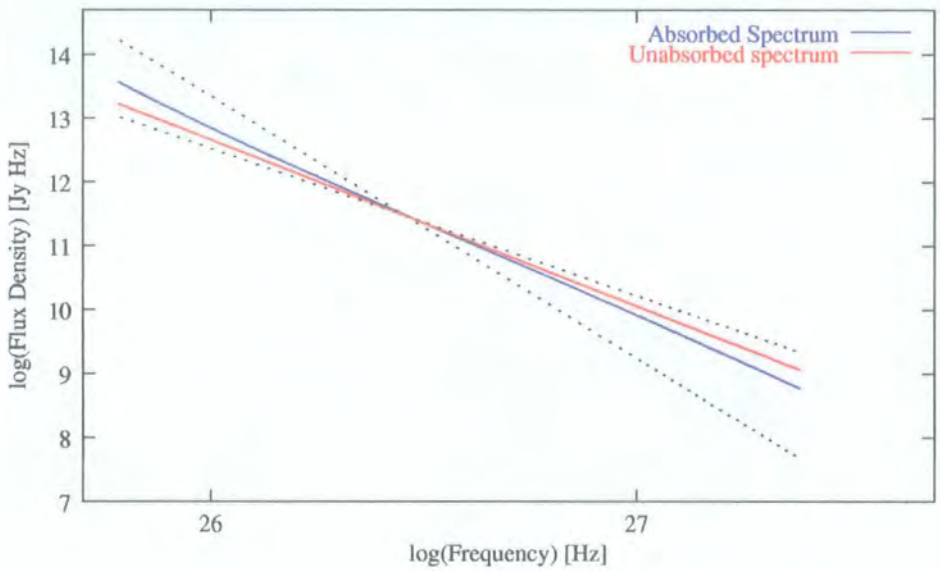

Figure 7.28: The spectrum of PKS 2155–304 was found to be a power law of spectral index 3.2 ± 0.9 (Nolan 2002). The shaded area covers the errors in the measurement of the spectrum. The red line represents the unabsorbed spectrum (spectral index 2.6). The blue line represents this spectrum after IR absorption using a model by Stecker & de Jager (1997). Both the unabsorbed and absorbed spectra lie within the errors as determined by Nolan (2002), making it impossible to say whether the emission has been subject to absorption. The systematic errors in Nolan (2002) do not allow direct comparison of fluxes between experiments, however spectral indices may be compared. The spectral lines shown have been shifted to make this comparison clearer.

and CANGAROO III, more detailed energy spectra of PKS 2155–304 may be obtained allowing conclusions to be made with respect to PKS 2155–304 and the IRB.

7.9 Conclusion

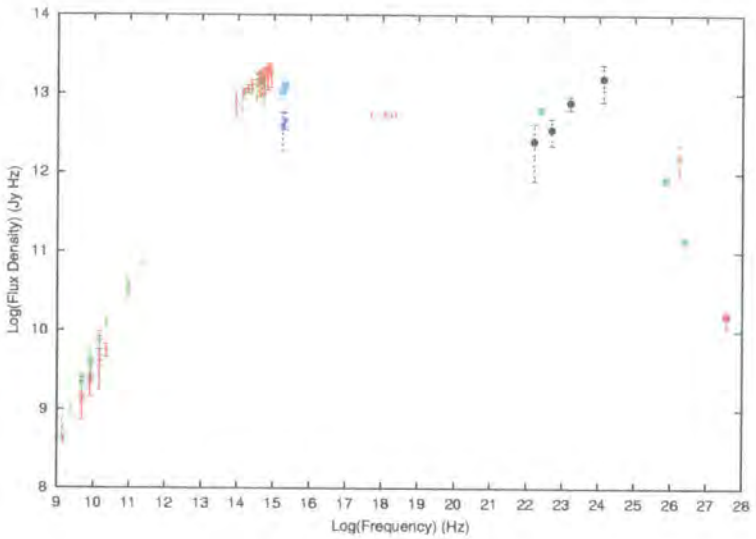

Figure 7.29: The spectral energy distribution of PKS 2155–304 was compiled from Chiapetti et al. (1999) and references therein. i.e. Courvoisier et al. (1995) Pesce et al. (1997) Pian et al. (1997) Chiapetti et al. (1999) Urry et al. (1993) Stecker et al. (1996) Vestrand, Stacy & Sreekumar (1995) Chadwick et al. (1999) and this work (magenta circle). Predictions by Stecker et al. (1996) are represented by blue squares without errorbars. The data are not contemporaneous.

A search for TeV gamma ray emission from Mark 6 observations of PKS 2155–304 between 1996 and 1999 was undertaken. An overall positive signal was present in the dataset. Upon further investigation, the signal was found to be predominantly from 1996 and 1997 observations, specifically September 1996, October 1997 and November

1997.

A 3σ upper limit to emission (see equation 1.7) above 1.5TeV, in 1999 was determined to be $6.6 \times 10^{-14}\text{cm}^{-2}\text{s}^{-1}$. These points are shown in the SED of PKS 2155–304 in figure 7.29.

Evidence for variability within the dataset was searched for by using the t-test and χ^2 tests. While evidence for variability was found, it was not very strong. Further investigations with the new generation of gamma ray telescopes will help to determine, more accurately, the variability of PKS 2155–304.

Evidence for correlation of X-ray and gamma ray emission was looked for and found to be weak within this dataset. However, it is worth noting that the ASM and Mark 6 observations were not contemporaneous but were taken within eight hours of each other.

It is worth noting that at the time of the 1996/7 detection PKS 2155–304 was found to be in a heightened state of X-ray emission. In 1997, when gamma ray emission was detected, the maximum X-ray flux of PKS 2155–304 as observed by RXTE was $F_{(2-10\text{ keV})} = 2.3 \times 10^{-10}$ erg cm^{-2} s^{-1} (Vestrand & Sreekumar 1999).

The average RXTE ASM intensity for PKS 2155–304 is similar at times corresponding to Mark 6 observations in 1996 and 1999. The overall BeppoSAX X-ray spectrum for PKS 2155–304 has a much lower flux density in 1999 than in 1996, as shown in figure 7.25. However, as blazars are known to vary on timescales of the order of minutes it is possible that the X-ray flux was actually low when the Mark 6 observations were taken in 1999. As the event count rate is significantly lower in 1999 than in 1996, it is likely that the Mark 6 was significantly less sensitive in 1999 than in 1996.

This, in turn, would result in an increased energy threshold for the Mark 6 to a level

where absorption by the DEBRA would have more of an influence on detectable photons. The increased energy threshold of the Mark 6 was estimated to be 1.5 ± 0.1 TeV. The level of absorption due to the IRB for emission from PKS 2155–304 at 1.5 TeV would be $e^{-1.4}$ (Stecker & de Jager 1997).

During the 1999 observations however, the X-ray flux was much less than what it was in 1996 or 1997, as can be seen in figure 7.25. PKS 2155–304 was not emitting gamma rays at a level detectable by the Mark 6 at this time. During the 1998 and 1999 observation periods, PKS 2155–304 was not seen to be very bright in X-rays. This non-detection of a signal from PKS 2155–304 does not impose any restriction on possible emission models of blazars.

Further observation of PKS 2155–304 by the next generation of telescopes will be required to answer questions on the physics at work. Observations of PKS 2155–304 made with the H.E.S.S. telescopes are discussed in chapter 9.

Chapter 8

Observations of PKS 2005–489 and PKS 0548–322

PKS 2005–489 and PKS 0548–322 are both close, Southern hemisphere, high frequency peaked BL Lac objects (see section 3.1.4). PKS 2005–489 has a redshift of $z = 0.071$ (Falomo et al. 1987) and PKS 0548–322 has a redshift of $z = 0.069$ (Fosbury & Disney 1976). Both Stecker et al. (1996) and Costamante & Ghisellini (2002) have predicted that PKS 2005–489 and PKS 0548–322 should be TeV gamma ray emitters.

This chapter will outline the observational history of these blazars and focus on observations taken with the Mark 6 between 1996 and 1998.

8.1 The Observational History of PKS 2005–489 and PKS 0548–322

PKS 2005–489 was discovered in the Parkes 2.7 GHz survey (Wall et al. 1975), initially classified as an N galaxy* (Savage et al. 1977), and subsequently identified as a BL Lac object on the basis of its bright star-like nucleus, flat radio spectrum, and featureless optical continuum (Wall et al. 1986, and references therein).

8.1.1 Companion Galaxies

BL Lac objects have been found to be more likely to have a significant number of companions compared to other AGN. PKS 2005–489 and PKS 0548–322 are no exception.

PKS 2005–489

Falomo (1996) reports on observations of PKS 2005–489 taken using the New Technology Telescope (NTT) at the European Southern Observatory (ESO) under 1 arcsec seeing conditions. The host galaxy was found to be rather round (eccentricity $\lesssim 0.05$) and as for all BL Lac objects, is an elliptical galaxy. The derived absolute magnitude, $M_R = -23.7$, is slightly fainter than that ($M_R = -24.2$) previously derived by Stickel et al. (1993). Falomo et al. (2000) report on Hubble Space Telescope (HST) observations of PKS 2005–489 and its diffuse companion, the nature of which is unknown awaiting spectroscopic observations.

*A type of radio galaxy having a brilliant starlike nucleus containing most of the luminosity of the system.

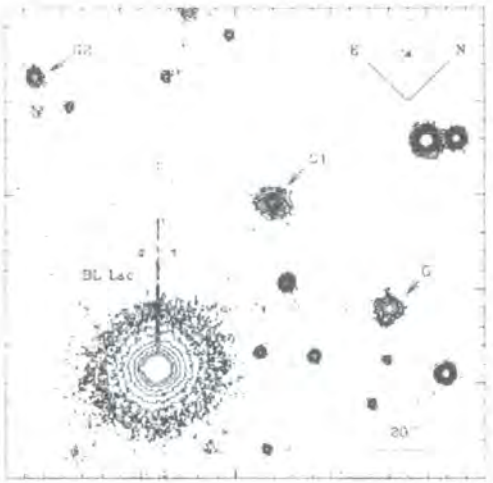

Figure 8.1: The field of view of PKS 2005–489 taken from Pesce et al. (1994). The jet like feature seen is a diffraction spike from the bright nucleus. This image was taken using observations from the 3.5m NTT at ESO. It was shown that PKS 2005–489 has at least three galaxies in its field at similar redshift.

PKS 0548–322

Kinman (1978) noted the presence of galaxies near to PKS 0548–322 and suggested they are close enough to be interacting. Later, Falomo et al. (1995) reported on the direct subarcsecond resolution imaging of the nebulosity and spectroscopy of galaxies in the field of PKS 0548–322. The host galaxy has $M_V = -23.4$ and exhibits signs of interaction with a close companion galaxy at ~ 25 kpc. The source is located in a rich cluster of galaxies. Spectra of five galaxies in the field indicate that they are at the same redshift as PKS 0548–322 (between z=0.067 and 0.072) supporting the imaging result of a surrounding cluster associated with PKS 0548–322. There are clear signs of interaction with the host galaxy of PKS 0548–322 via the presence of extended low surface brightness emission located $\sim 8''$ to the West (as seen in figure 8.2). For PKS 0548–322, one of the nearby galaxies

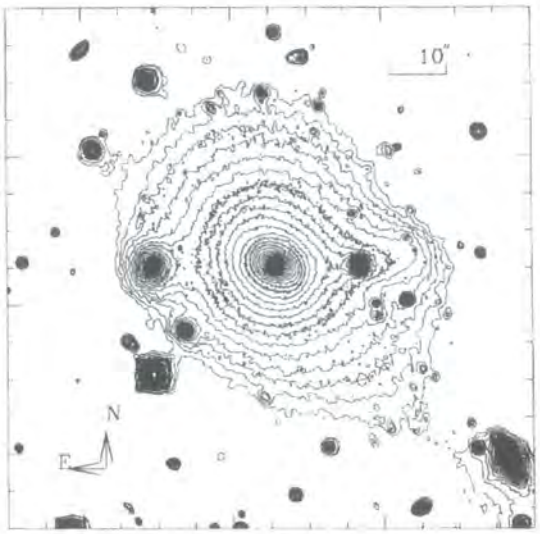

Figure 8.2: The field of view of PKS 0548–322 taken from Falomo et al. (1995). This image was obtained using the Superb Seeing Imager (SUSI) at the 3.5m NTT at ESO.

is obviously in tidal interaction with the BL Lac host, as indicated by the low-surface brightness and extended emission described in Falomo et al. (1995). This is the first clear case of interaction between a BL Lac and a companion. Such interactions seem to occur frequently in Seyfert and other active galaxies (Heckman et al. 1986).

8.1.2 Radio Observations

All blazars have been detected at radio wavelengths.

PKS 2005–489

Giommi et al. (1995) report on the radio to X-ray flux of BL Lac objects. They used non-contemporaneous observations of objects to construct SEDs. Radio flux density $F_{0.41\mathrm{GHz}} = 1.31 \pm 0.04$ Jy was reported by Large et al. (1981). $F_{2.7\mathrm{GHz}} = 1.06 \pm 0.04$ Jy and $F_{5.0\mathrm{GHz}} =$

1.19 ± 0.04 Jy were reported by Wall et al. (1975).

PKS 0548–322

Giommi et al. (1995) gave the monochromatic flux at 5 GHz as 230 mJy. PKS 0548–322 is the only BL Lac known to be a head-tail radio source[†] (Antonucci & Ulvestad 1984).

8.1.3 Infrared and Visible Observations

PKS 2005–489 is a moderately variable object ($\Delta m = 0.53$; Boyzan et al. 1990). The limited infrared data (from Wall et al. 1986) show a variation of only about 0.25 mag. Bersanelli et al. (1992) report on J, H, K, and L band observations of PKS 2005–489 and PKS 0548–322 taken with the 3.6m and 2.2m telescopes at ESO. The results are presented in table 8.1. It can be seen that PKS 0548–322 is much fainter than PKS 2005–489 at optical wavelengths. Also, it can be noted that the range between the minimum and maximum flux is much greater for PKS 2005–489 than for PKS 0548–322.

[†]A class of relatively weak radio sources associated with clusters of galaxies and characterised by a high brightness "head" close to the optical galaxy and a long low brightness "tail".

Object	F_J (mJy)	F_H (mJy)	F_K (mJy)	F_L (mJy)
PKS 0548–322	5.63±0.56	7.17±0.22	6.87±0.27	
	5.04±0.20	6.72±0.20	6.32±0.13	
PKS 2005–489	25.70±0.77	31.00±0.93	33.11±1.68	38.86±5.05
	19.32±0.39	23.73±1.19	26.06±1.04	27.64±5.25

Table 8.1: Taken from Bersanelli et al. (1992): ESO JHKL photometry observations of PKS 2005–489 and PKS 0548–322 between 1987 and 1989. The first line in each object represents the maximum flux observed while the second line represents the minimum flux observed.

The maximum recorded value of the polarisation of the optical light from PKS 2005–489 is 2%. Most BL Lac objects of the 1 Jy sample exhibit higher values (Stickel et al. 1993). This may be related to the state of the magnetic field within the jet of PKS 2005–489.

8.1.4 Ultraviolet Observations

Edelson (1992) reviewed IUE observations of PKS 2005–489, from which the mean UV flux was determined to be 3.38 mJy. The Colorado IUE Active Galaxy survey reported on observations of PKS 0548–322 (Edelson et al. 1992). It was found to have a flux density of between 0.29±0.02 mJy and 0.326±0.014 mJy, which is $\sim$ 10 fainter than PKS 2005–489. PKS 2005–489 and PKS 0548–322 were detected in the UV band by EUVE (Marshall et al. 1995).

8.1.5 X-ray Observations

PKS 2005–489

Ghosh & Soundararajaperumal (1995) report observations of PKS 2005–489 on five occasions with EXOSAT between 1984 and 1985. Of these five observations only three had signal significance above 4 σ. A weak emission bump around the near-infrared and optical bands is present and there is no discontinuity in the UV to X-ray region as seen in figure 8.3. Ciliegi et al. (1993) report on EXOSAT observations of PKS 2005–489 during 1984

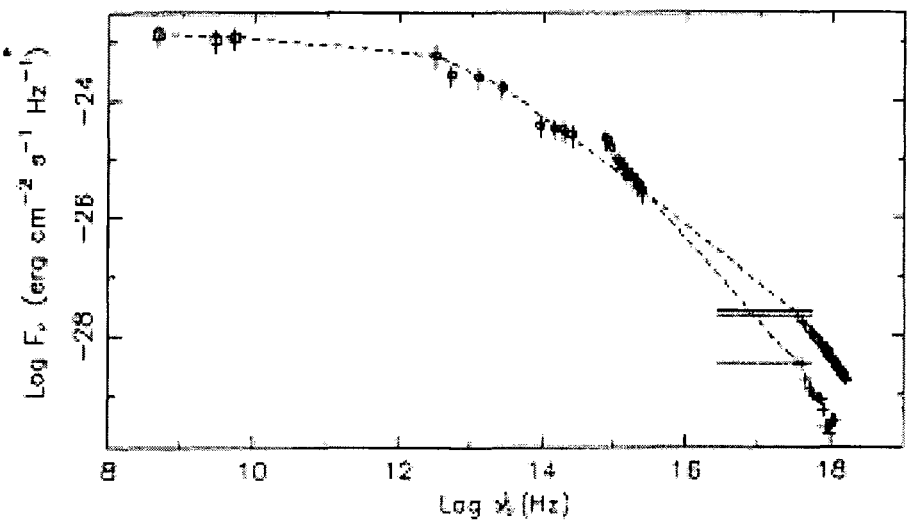

Figure 8.3: The multifrequency spectrum of PKS 2005–489 taken from Ghosh & Soundararajaperumal (1995) and references therein.

and 1985 when the $2-8$ keV flux varied between $(0.23 \pm 0.37) \times 10^{-2}$ photons cm^{-2} s^{-1} and $(6.32 \pm 0.35) \times 10^{-2}$ photons cm^{-2} s^{-1}. From these EXOSAT observations, Sambruna et al. (1994) found that PKS 2005–489 varied in intensity by a factor of ~ 10 from the higher states of 1984 to the lower states of 1985. Long-term variability in X-rays was noted by Wall et al. (1986), who studied two 1984 observations. Sambruna et al. (1995)

reported on two ROSAT PSPC pointed observations of PKS 2005–489 and found that the $0.2 - 20$ keV continuum spectrum of PKS 2005–489 was steep (photon index ~ 3.0) and extrapolated well to the faintest spectrum measured with EXOSAT in a harder range. The X-ray spectrum was found to harden with increasing intensity. The smooth connection of the X-ray spectrum to the optical UV continuum suggests a common synchrotron origin, while SSC scattering could explain the observed gamma rays. Sambruna et al. (1995) applied the inhomogeneous relativistic jet model to PKS 2005–489 and found that the derived value of the magnetic field is similar to that of the X-ray bright BL Lac object Mrk 421. The spectral hardening with increasing intensity in PKS 2005–489 can be accounted for by a small gradient in the density of the relativistic electrons and by a substantial increase of their maximum energy. It was suggested that magnetic field strengths and particle energies may be the main physical quantities governing the shape of the multifrequency continuum emission in blazars.

PKS 0548–322

Barr et al. (1988) report on EXOSAT observations of PKS 0548–322 during March 1986. The $0.05 - 10$ keV X-ray spectrum was found to be characterised by a relatively flat continuum (power-law energy spectral index ≈ 0.9) below 5 keV which steepened at higher energies. It was concluded that, assuming the X-ray emission arose via synchrotron emission with the spectral break due to radiative losses, reacceleration of the emitting particles and an inhomogeneous emission region were indicated. The source was determined to be in a low state of emission with 2 keV flux intensity < 0.008 photons cm^{-2} s^{-1}.

Ghosh & Soundararajaperumal (1995) reported observations of PKS 0548–322 at five

epochs with EXOSAT between 1985 and 1986. PKS 0548–322 did not display long-term variability of the low-energy and medium-energy count rates, but significant rapid variability of the medium-energy count rate was found on 2nd November 1983 and 7th and 8th March 1986, which was also noted by Giommi et al. (1990). No intrinsic absorption has been observed in this source. Ghosh & Soundararajaperumal (1995) claimed that a single parabola could represent the multifrequency spectrum of this blazar – see figure 8.4. PKS 0548–322 was observed in X-rays with GINGA five times between January 1990

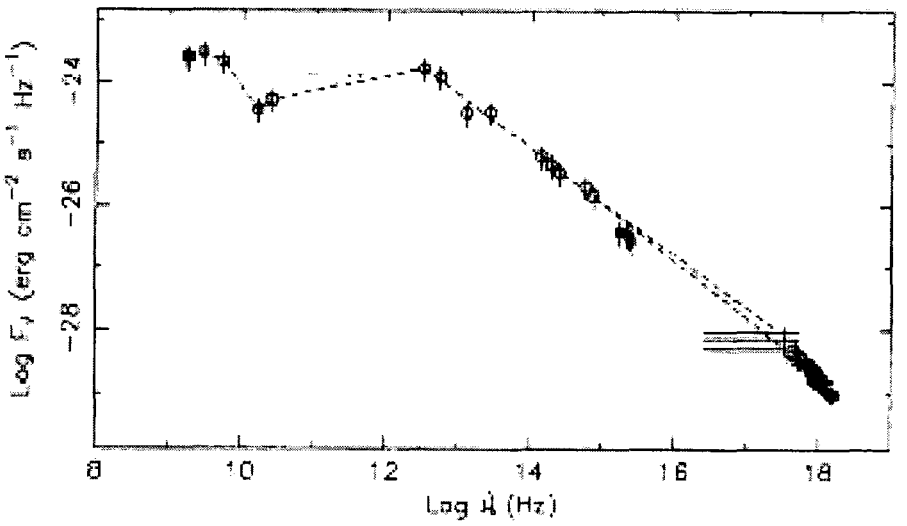

Figure 8.4: The multifrequency spectrum of PKS 0548–322 taken from Ghosh & Soundararajaperumal (1995) and references therein.

and March 1991 (Tashiro et al. 1995). The $2-10$ keV flux varied by a factor of 2.5 and the spectral index varied between 0.8 ± 0.02 and 1.03 ± 0.04. No simple relation was found between the flux and the spectral index. Results indicate that PKS 0548–322 exhibited a relatively flat X-ray spectrum ($\alpha \sim 1$) among BL Lacs, together with complex changes and occasional spectral bending. PKS 0548–322 exhibits one of the clearest examples of

soft X-ray absorption features as confirmed by ASCA observations (Tashiro et al. 1994). Lamer et al. (1996) report a ROSAT flux measurement of PKS 0548–322 from 1992 of $F_{1\mathrm{keV}} = 9.59\ \mu\mathrm{Jy}$.

8.1.6 Gamma ray Observations

PKS 2005–489

PKS 2005–489 was detected by EGRET at energies > 100 MeV with a flux of $(1.8 \pm 0.5) \times 10^{-7}$ photons cm^{-2} s^{-1} (Fichtel et al. 1994). It was also recorded at marginal significance in the GeV EGRET catalogue with a flux of $(2.2 \pm 0.8) \times 10^{-8}$ cm^{-2} s^{-1} for energies greater than 1 GeV (Lamb & Macomb 1997). The CANGAROO group has reported upper limits to TeV emission for PKS 2005–489. Roberts et al. (1998) reported observations of PKS 2005–489 taken in August 1993 and August/September 1994. During this time they obtained 41 hours on-source and 38 hours of off-source data. PKS 2005–489 was not detected, but a 2σ upper limit to emission of $F_{>2\mathrm{TeV}} < 1.1 \times 10^{-12}$ cm^{-2} s^{-1} was determined. CANGAROO observed PKS 2005–489 from 27$^{\mathrm{th}}$ August to 9$^{\mathrm{th}}$ September 1997. This consisted of 17 hours on-source and 15 hours of off-source data. Again the source was not detected but a 2σ upper limit of $F_{>1.5\mathrm{TeV}} < 7.0 \times 10^{-12}$ photons cm^{-2} s^{-1} was determined. During these 1997 observations the RXTE ASM showed an average X-ray count rate of 0.8 ± 0.1 per second. Observations of PKS 2005–489 taken using the Mark 6 will be discussed in section 8.3.

PKS 0548–322

McNaron-Brown et al. (1995) report OSSE observations of PKS 0548–322 taken during June 1992. PKS 0548–322 was detected at energies $0.05 - 0.15$ MeV, to the 3σ level, with a flux of $(2.60 \pm 2.06) \times 10^{-3}$ photons cm^2 s^{-1} MeV^{-1}. 2σ upper limits were reported of $F_{0.15-0.5\mathrm{MeV}} < 1.24 \times 10^{-3}$ photons cm^2 s^{-1} MeV^{-1} and $F_{0.5-1.0\mathrm{MeV}} < 1.16 \times 10^{-3}$ photons cm^2 s^{-1} MeV^{-1}. Gamma ray emission from PKS 0548–322 was not detected with EGRET. The CANGAROO group reported observations of PKS 0548–322 taken from 28$^{\mathrm{th}}$ October to 27$^{\mathrm{th}}$ November 1997 (Roberts et al. 1999). This amounted to 26 hours on-source and 22 hours of off-source observations. No evidence for gamma ray emission was found during this time, and a 2σ upper limit of $F_{>1.5\mathrm{TeV}} < 4.3 \times 10^{-12}$ photons cm^{-1} s^{-1} to the integral flux was determined. No evidence for detectable flare activity on the scale of ~ 1 day was found either. The average RXTE ASM count rate during this time was 0.14 ± 0.07 s^{-1}. The maximum count rate during this period was 0.45 ± 0.8 s^{-1}. The optical activity of PKS 0548–322 was monitored between 29$^{\mathrm{th}}$ October and 6$^{\mathrm{th}}$ November 1997 by a Celestron C14 Schmidt-Cassegrain with an Optec UBVRI filter set and an SBIG ST-6 CCD at the CANGAROO, Woomera site. No variations were found throughout this period and the average R band flux was 4.48 mJy, similar to other optical measurements (see e.g. Xie et al. 1996). These optical and X-ray observations indicate that PKS 0548–322 was in a typical state of activity during the CANGAROO observations. Observations of PKS 0548–322 taken using the Mark 6 will be discussed in section 8.3.

8.2 Multiwavelength Campaigns

PKS 2005–489

Perlman et al. (1999) reported monitoring PKS 2005–489 with RXTE in October to November of 1998. During these months the source underwent a spectacular flare; at its peak on November 10, its $2 - 20$ keV flux was 3.33×10^{-10} ergs cm^{-2} s^{-1}, over thirty times brighter than in quiescence. The X-ray spectrum was seen to harden prior to the peak, steepened in the declining phase and then hardened again as the flux continued to decrease. This pattern has been observed in several HBLs including Mrk 421 (Takahashi et al. 1996, Takahashi et al. 1999), PKS 2155–304 (Sembay et al. 1993, Chiapetti et al. 1999) and Mrk 501 (Pian et al. 1998). While such behaviour has been seen before, the simplicity, magnitude and duration of this flare allowed it to be studied in great detail. Perlman et al. (1999) argued that this flare was caused by either the injection of particles into the jet or in situ particle acceleration and that the spectral steepening which followed the flare maximum was the result of synchrotron cooling. Contrary to other recently observed blazar flares these results do not imply a major shift in the location of the synchrotron peak during this flare. By comparison, the 1997 flare of Mrk 501 (Pian et al. 1998) represented an increase in $2 - 10$ keV flux of slightly less than a factor of 20 (peak to quiescence; during its flare Mrk 501's synchrotron spectrum peaked at 100 keV) and a peak luminosity of 1.9×10^{45} erg s^{-1}. Observations by Perlman et al. (1999) show that PKS 2005–489 was in an enhanced flux state for at least 3 months. The flare's peak was characterised by a plateau lasting about 4 days (see figure 8.5) and the half-maximum region spanned 35 ± 5 days. No variability was found on timescales of less than 1 day.

Figure 8.5 shows that the emission in the harder bands declines faster. No evidence of a lag is found when cross correlating the $2-5$ keV and $5-10$ keV light curves. When RXTE observations commenced on October 14, the X-ray spectrum of PKS 2005–489 was already flatter than it would be in quiescence ($\alpha = 1.45$ compared with $\alpha = 1.6-1.9$).

During this flare, the X-ray spectrum of PKS 2005–489 responded similarly to other HBLs but with larger changes in the declining phase (where $\alpha = 1.5-1.8$, similar to values obtained in quiescence) than in the rising phase (see figure 8.5). Importantly, the data do not imply a large shift in the location of the synchrotron peak. This flare of PKS 2005–489 thus appears to have been more similar to flares of Mrk 421 (Takahashi et al. 1999) than Mrk 501 (Pian et al. 1998) where much larger shifts in the spectral peak were observed. This could indicate a diversity in physical circumstances in blazar flares such as the balance between acceleration, particle injection and cooling. The usual interpretation of the X-ray spectral changes observed in HBLs (see models by e.g. Georganopoulos & Marsher 1998) is that the hardening observed during the flare's rising phase is caused by reacceleration and/or injection of electrons (either freshly injected or already within the jet). This may be associated with a local compression or augmentation of the jet magnetic field. In the declining phase, synchrotron or Compton cooling is the dominant factor. Perlman et al. (1999) interpreted the flare as follows: the increase of flux was due to a fresh injection or acceleration of energetic particles throughout the source, which was assumed to happen on a timescale that was (locally) much shorter than the light travel time across the source. The decrease in flux, which was slower than the rise for all energies, was caused by those particles cooling via synchrotron radiation. No TeV gamma ray emission has so far been detected from PKS 2005–489, so the synchrotron

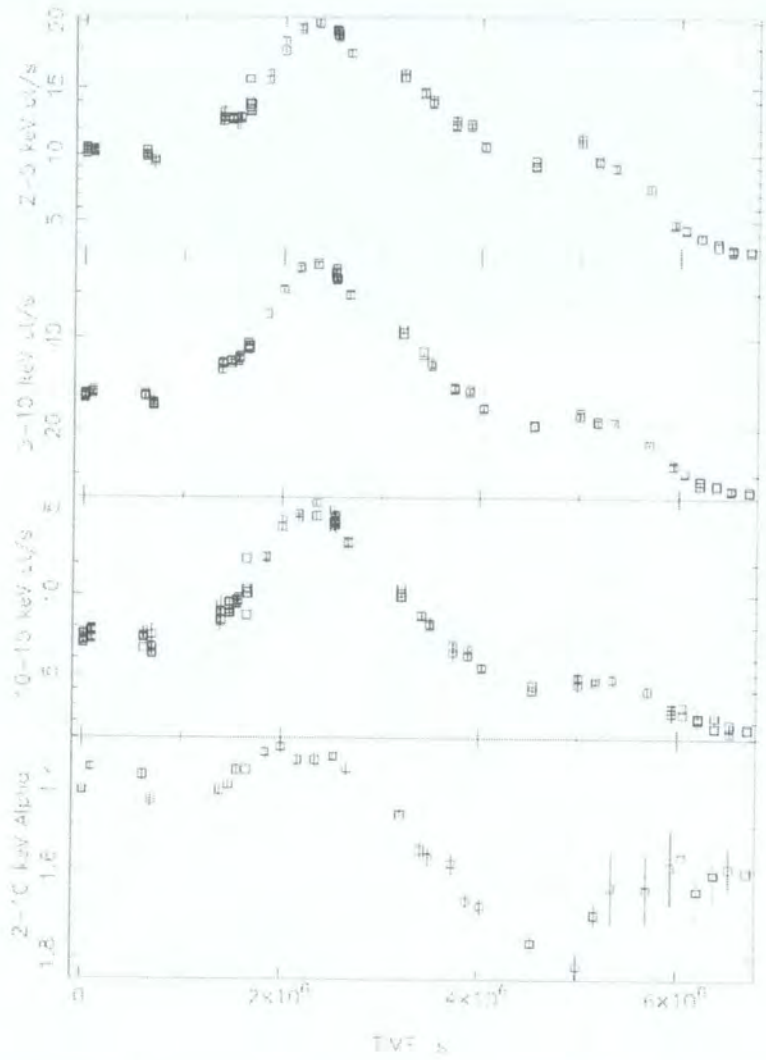

Figure 8.5: The RXTE PCA count rates and energy spectral indices for PKS 2005–489 during October to December 1998 are shown. Count rates are given in the 2-5 keV (top), 5-10 keV (second from top) and 10-15 keV bands (third from top), while the spectral indices plotted (bottom) are for the 2-10 keV band. Given the observed spectra, the weighted mean energy of the photons in the 2-5 keV band is ~3 keV, in the 5-10 keV band it is ~7 keV, and in the 10-15 keV band it is ~12 keV. These values are spectral index dependent, but change by only a few percent for the spectra observed. On this figure, a time of 0 s refers to the beginning of the first (October 14) observation, and the peak, which occurred on November 10, is at 2.4×10^6 s. Taken from Perlman et al. (1999).

component is likely to be more luminous than the Compton component. It is therefore assumed that synchrotron losses dominate. Tagliaferri et al. (2001) also reported on JHK observations of PKS 2005–489 in 1998 one day before BeppoSAX observations of a flare were taken (see section 8.1.5). During this time there was little change in the slope of the IR spectrum as the luminosity changed. This is due to the fact that the synchrotron peak is at much higher energies. The K magnitude changed by only 0.32 magnitudes during these observations. Tagliaferri et al. (2001) also report on BeppoSAX observations of PKS 2005–489 from 1st to 2nd November 1998, following an active X-ray state detected by RXTE. The synchrotron peak frequency was determined to be between 10^{15} Hz and 2.5×10^{16} Hz, depending on the model assumptions. A non-contemporaneous SED for PKS 2005–489 is shown in figure 8.6.

PKS 0548–322

There have been no multiwavelength campaigns on PKS 0548–322. A non-contemporaneous SED for PKS 0548–322 is shown in figure 8.7.

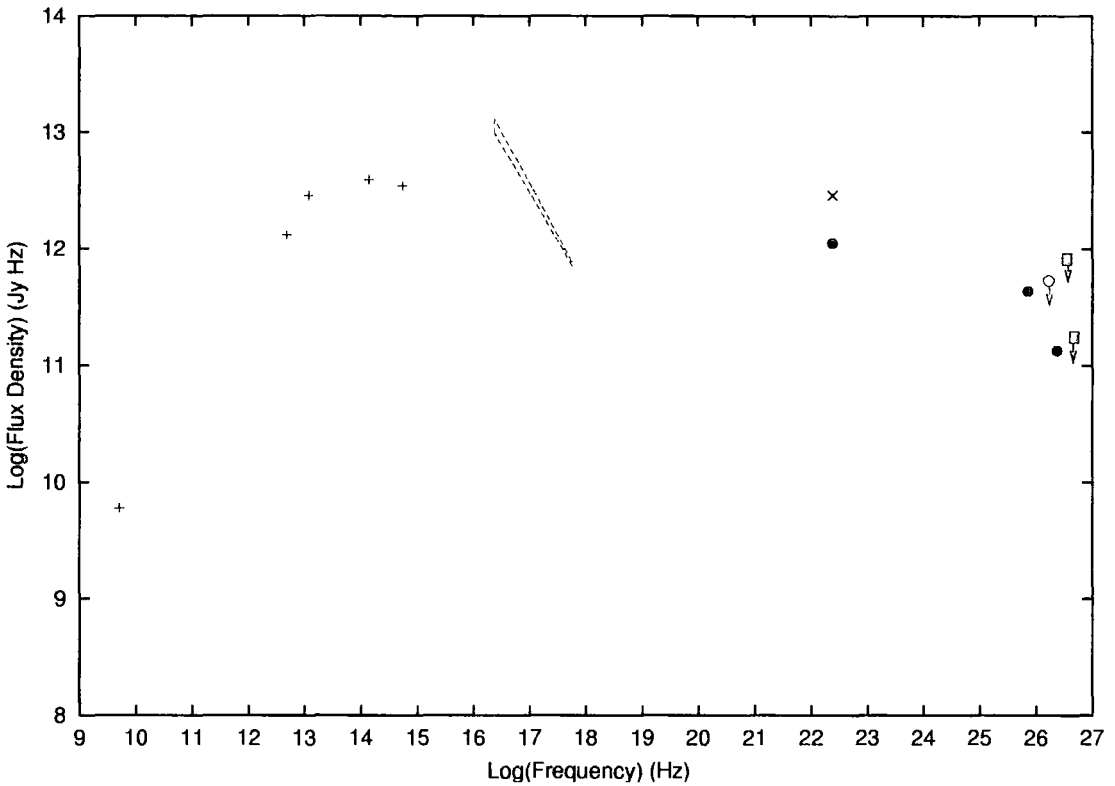

Figure 8.6: The broadband spectral energy distributions for PKS 2005–489. The radio to X-ray points are from the compilation of Fossati et al. (1998). CANGAROO observations are 2 σ upper limits (blue squares) (Roberts et al. 1999). The point from the present work is denoted by the solid pink circle and is also a 2 σ upper limit. Flux predictions of Stecker et al. (1996) are represented by solid black circles. Measurements are not contemporaneous. The EGRET observation (blue cross) is a $\sim 4\sigma$ detection from the first source catalogue Fichtel et al. (1994).

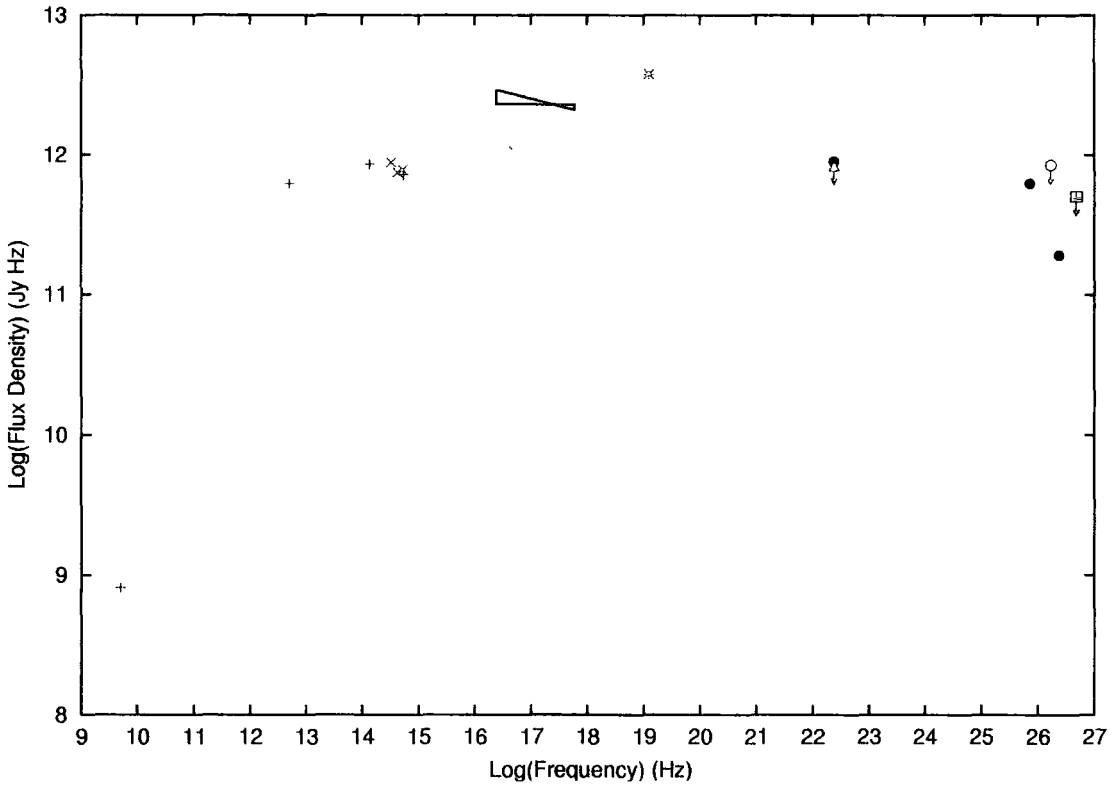

Figure 8.7: The broadband spectral energy distributions for PKS 0548–322. The radio to X-ray points are from the compilation of Fossati et al. (1998). The CANGAROO observation is a 2 σ upper limit (blue box) (Roberts et al. 1999). The 2 σ upper limit from the present work is denoted by a solid pink circle. Flux predictions of Stecker et al. (1996) are represented by solid black circles. The EGRET 2σ upper limit is represented by a magenta triangle (Fichtel et al. 1994). Measurements are not contemporaneous.

8.3 Observations Using the Mark 6

PKS 2005–489 and PKS 0548–322 were observed between 1996 and 1998 using the Mark 6. After quality control, there were just under 87 hours of on-source observations of PKS 2005–489 and just over 24 hours of on-source observations of PKS 0548–322 taken in chopped mode (section 6.1.1) using the Mark 6. There tended to be unsuitable weather (lightning) at the Mark 6 site when PKS 0548–322 was observable. This is the main reason for the small PKS 0548–322 dataset. The PKS 2005–489 data in October 1998 were taken during a multiwavelength campaign as described in section 8.2.

8.3.1 Observation Log

Date (yymmdd)	No. of pairs	Date (yymmdd)	No. of pairs	Date (yymmdd)	No. of pairs
960616	6	970605	3	980528	7
960618	2	970607	5	980529	4
960718	1	970608	5	980811	2
960719	2	970609	2	980813	3
960806	3	970610	5	980817	7
960807	6	970705	5	980818	9
960810	14	970706	14	980819	10
960811	6	970707	5	980820	7
960812	14	970728	8	980823	5
960813	8	970729	9	980824	6
960814	12	970730	11	980825	3
960816	1	970731	3	980913	9
960817	4	970801	3	980915	6
		970805	10	980916	7
		970807	15	980917	6
		970826	10	980918	2
		970827	9	980919	7
		970828	10	980921	5

continued on next page

Table 8.2: *continued*

Date (yymmdd)	No. of pairs	Date (yymmdd)	No. of pairs	Date (yymmdd)	No. of pairs
		970829	10	981011	1
		970920	2	981014	2
		970921	3	981015	8
		970924	9	981017	6
		970925	10	981021	6
		970926	8	981022	4
		970927	5		
		970930	9		

Table 8.2: Catalogue of Observations of PKS 2005–489 with the University of Durham Mark 6 Telescope. The data are listed in columns according to the observing year.

Date (yymmdd)	No. of pairs	Date (yymmdd)	No. of pairs	Date (yymmdd)	No. of pairs
960218	6	970925	1	980128	7
960219	4	970926	3	980129	4
961009	3	970927	2	981015	5
961010	5	970930	6	981017	7
961012	7	971023	2	981021	2
961013	5	971025	3		
961015	2				
961016	4				
961107	6				
961110	6				
961111	9				
961112	8				
961113	6				

Table 8.3: Catalogue of Observations of PKS 0548–322 with the University of Durham Mark 6 Telescope. The data are listed in columns according to the observing year.

8.3.2 Mark 6 Observations

State	On	Off	Excess	Significance (σ)
Tidied events	1,374,379	1,373,132	1,247	0.8
Shape selected events	111,574	109,881	1,693	3.6
Events with *alpha* $< 22.5°$	16,881	16,869	12	0.1

Table 8.4: Results of various event selections for PKS 2005–489 at all zenith angles. The cause in the drop of significance after the *alpha* $< 22.5°$ is due to an excess of gamma rays at large values of *alpha* as seen in figure 8.8.

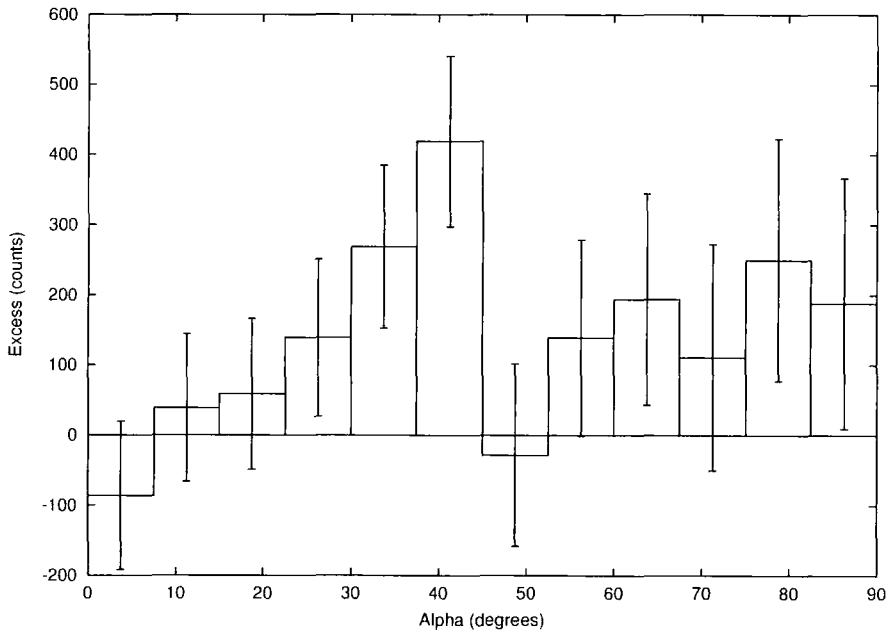

Figure 8.8: Alpha plot for the entire PKS 2005–489 dataset.

Observations made using the Mark 6 found no evidence for long-term emission of VHE gamma rays from either PKS 2005–489 or PKS 0548–322. Observations were made over a three year period, as outlined in tables 8.2 and 8.3. Data were analysed by the same procedure as used for PKS 2155–304. Tables 8.4 and 8.5 show the effect on event counts

State	On	Off	Excess	Significance (σ)
Tidied events	364,992	362,808	184	0.2
Shape selected events	23,743	23,188	555	2.6
Events with *alpha* $< 22.5°$	3,258	3,438	20	0.2

Table 8.5: Results of various event selections for PKS 0548–322 at all zenith angles. The cause in the drop of significance after the *alpha* $< 22.5°$ is due to an excess of gamma rays at large values of *alpha* as seen in figure 8.9.

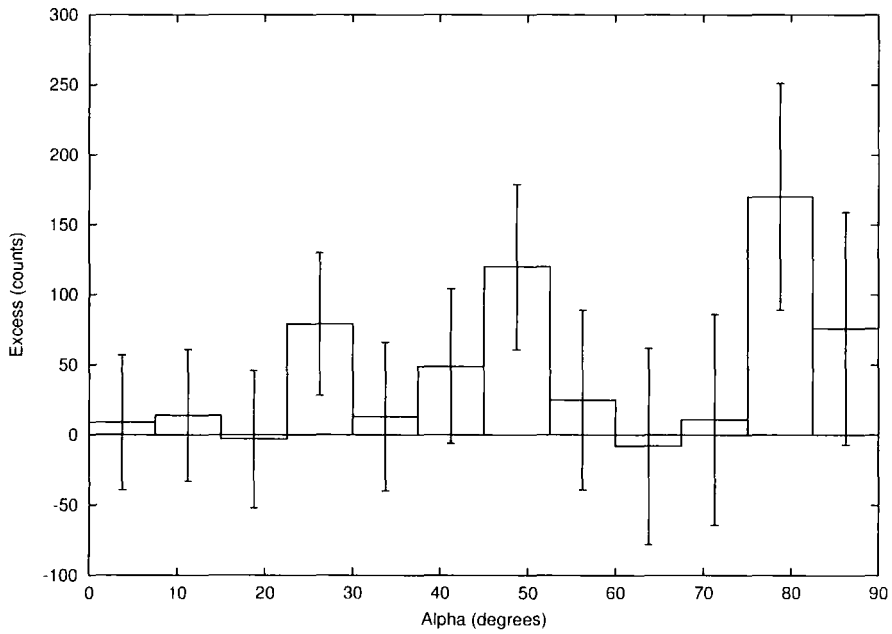

Figure 8.9: Alpha plot for the entire PKS 0548–322 dataset.

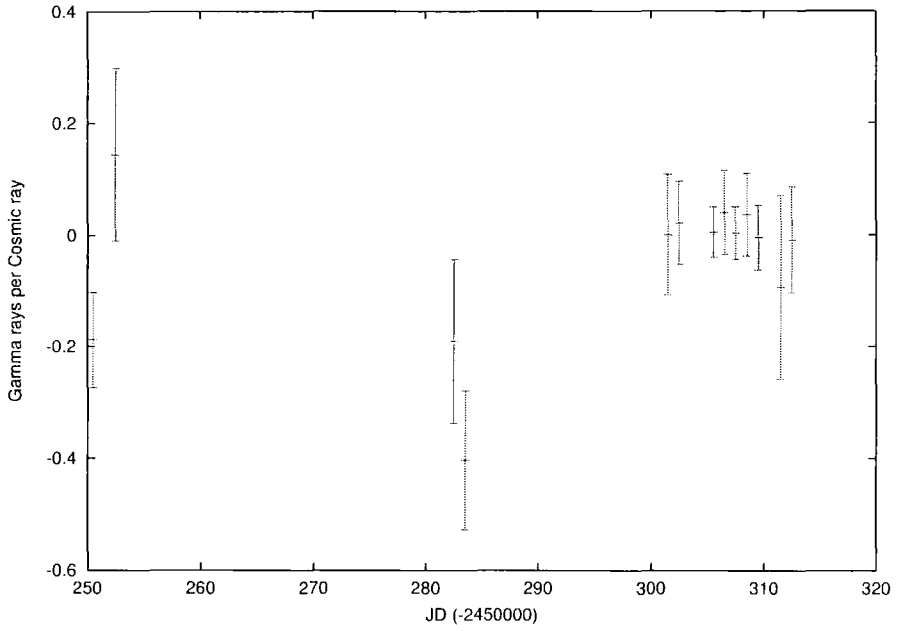

Figure 8.10: Daily rate of gamma rays per cosmic ray for PKS 2005–489 during 1996 as observed using the Mark 6.

of various stages of the analysis procedure.

As in the case of PKS 2155–304, graphs of the number of gamma rays per cosmic ray were plotted for both PKS 2005–489 and PKS 0548–322 (figures 8.10, 8.11, 8.12, 8.13, 8.14 and 8.15). Values consistent with zero were observed for the most part. Further inspection showed that any promising data points are the result of poor statistics.

A graph showing the distribution of gamma rays per cosmic ray values for each observation was plotted for each object, as seen in figure 8.16. In the case of PKS 2005–489, the distribution is seen to approximate a gaussian centered around zero, consistent with the non-detection of gamma ray emission from this object. In the case of PKS 0548–322, there are only a few observations compared to PKS 2005–489 and PKS 2155–304 but the distribution of gamma rays per cosmic ray is also centered around zero (figure 8.16).

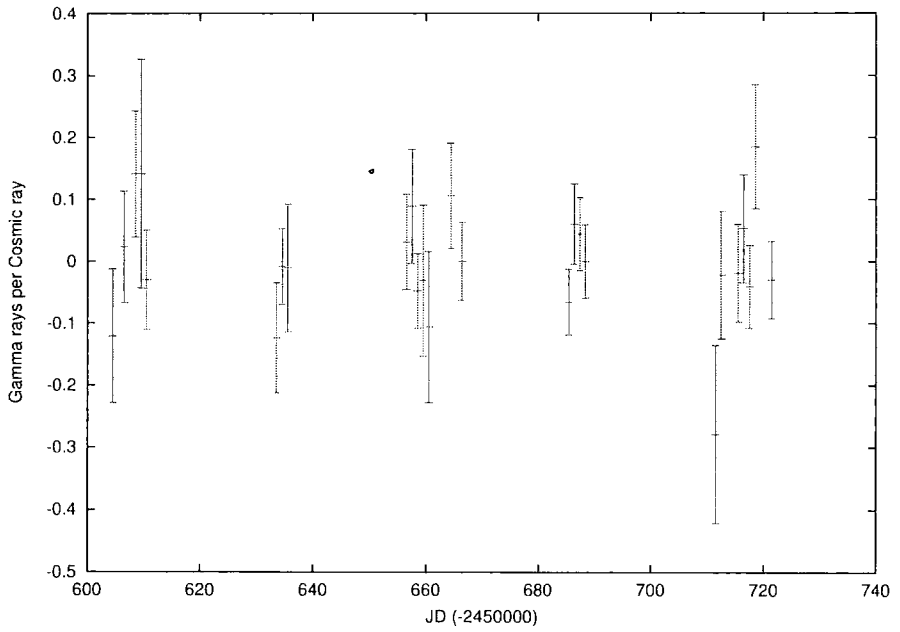

Figure 8.11: Daily rate of gamma rays per cosmic ray for PKS 2005–489 during 1997 as observed using the Mark 6.

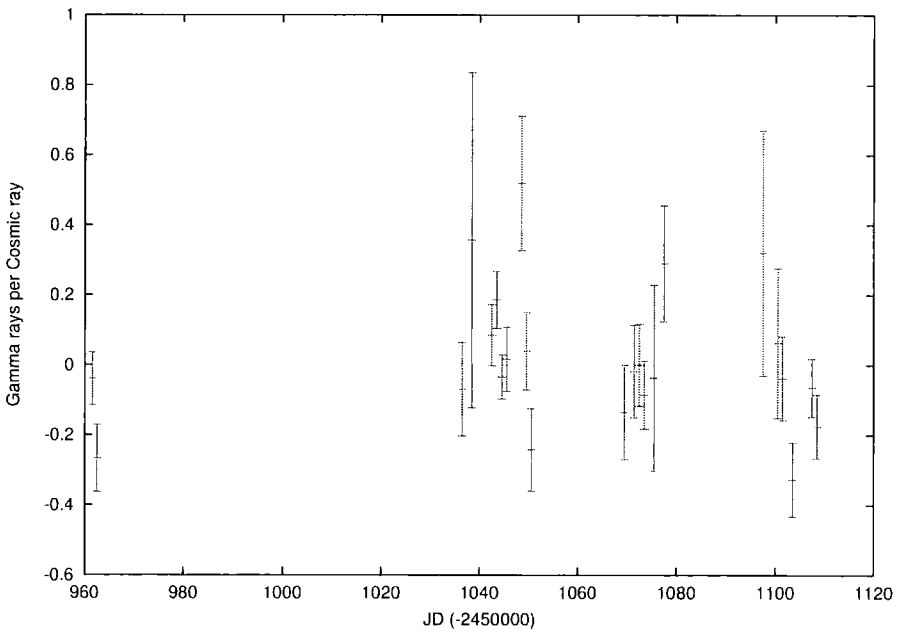

Figure 8.12: Daily rate of gamma rays per cosmic ray for PKS 2005–489 during 1998 as observed using the Mark 6.

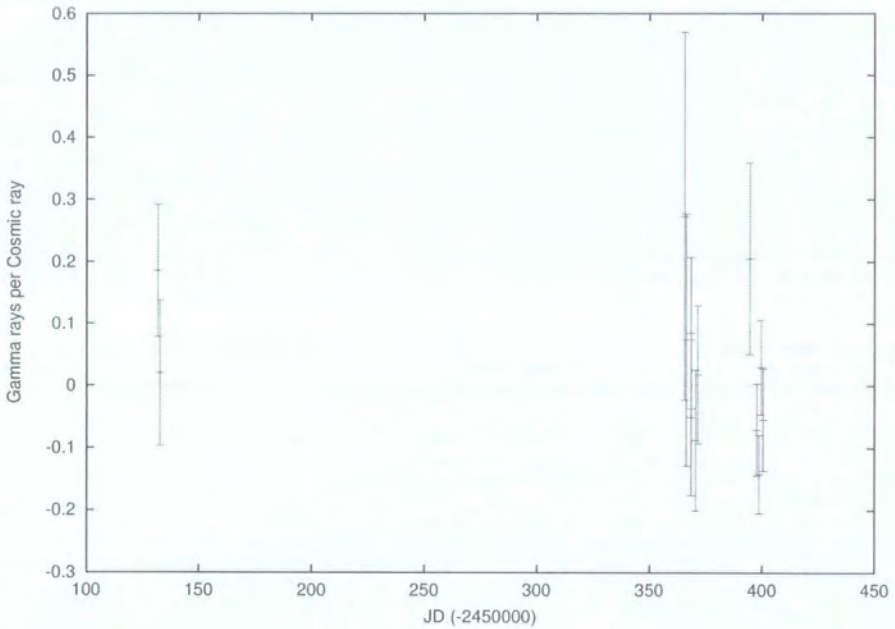

Figure 8.13: Daily rate of gamma rays per cosmic ray for PKS 0548–322 during 1996 as observed using the Mark 6.

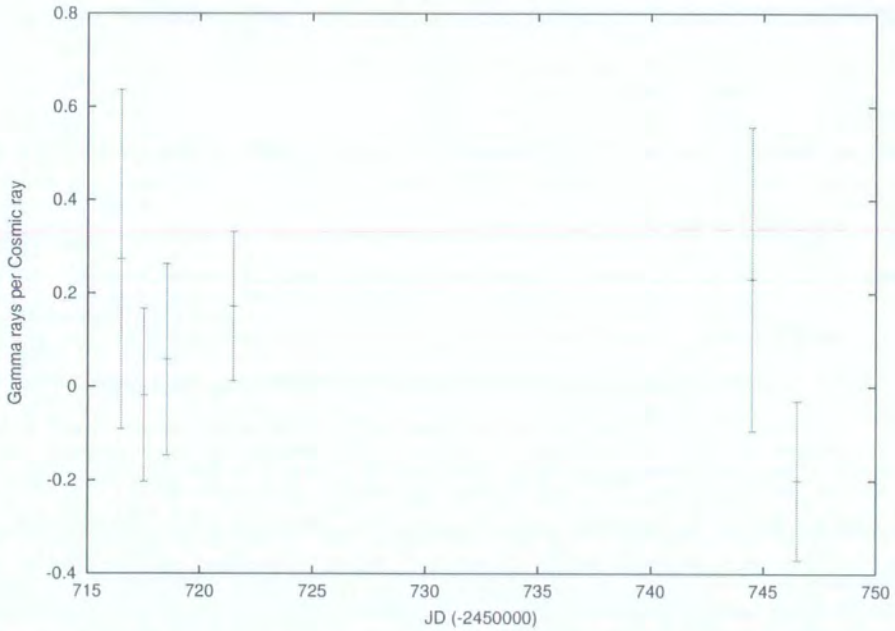

Figure 8.14: Daily rate of gamma rays per cosmic ray for PKS 0548–322 during 1997 as observed using the Mark 6.

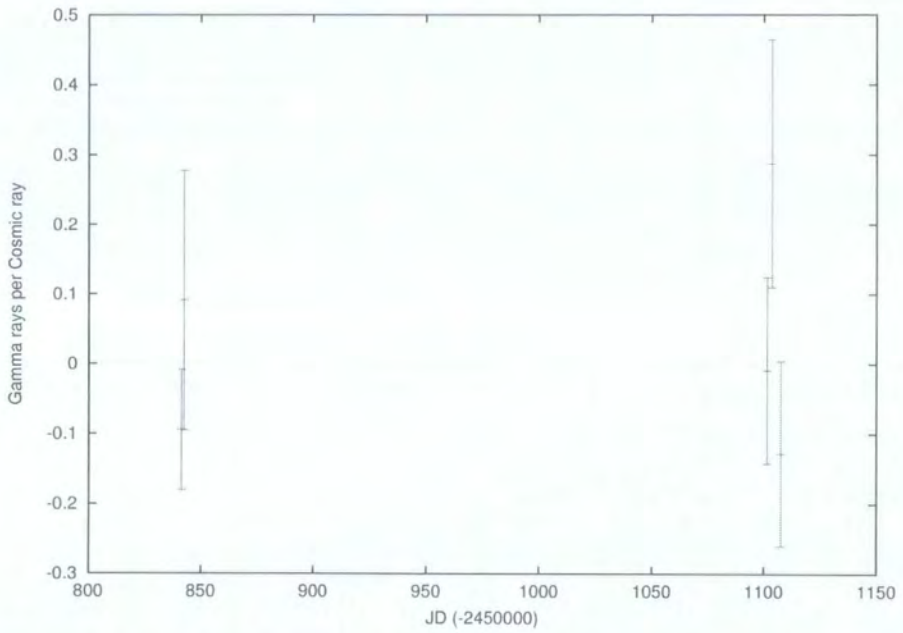

Figure 8.15: Daily rate of gamma rays per cosmic ray for PKS 0548–322 during 1998 as observed using the Mark 6.

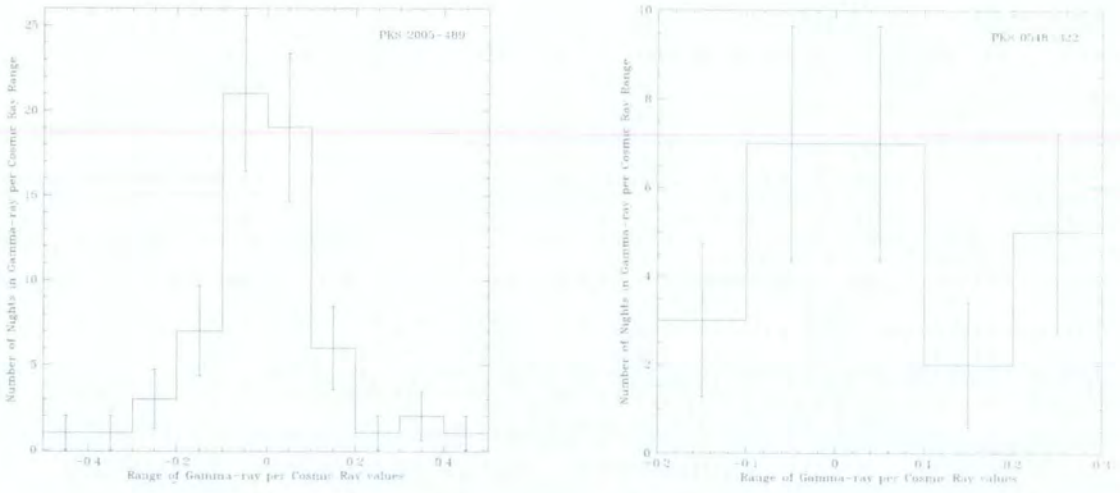

Figure 8.16: Distribution of Daily Values of Gamma rays per Cosmic Ray for PKS 2005–489 (left) and PKS 0548–322 (right).

Figures 8.17 and 8.18 show lightcurves for PKS 0548–322 and PKS 2005–489 respectively.

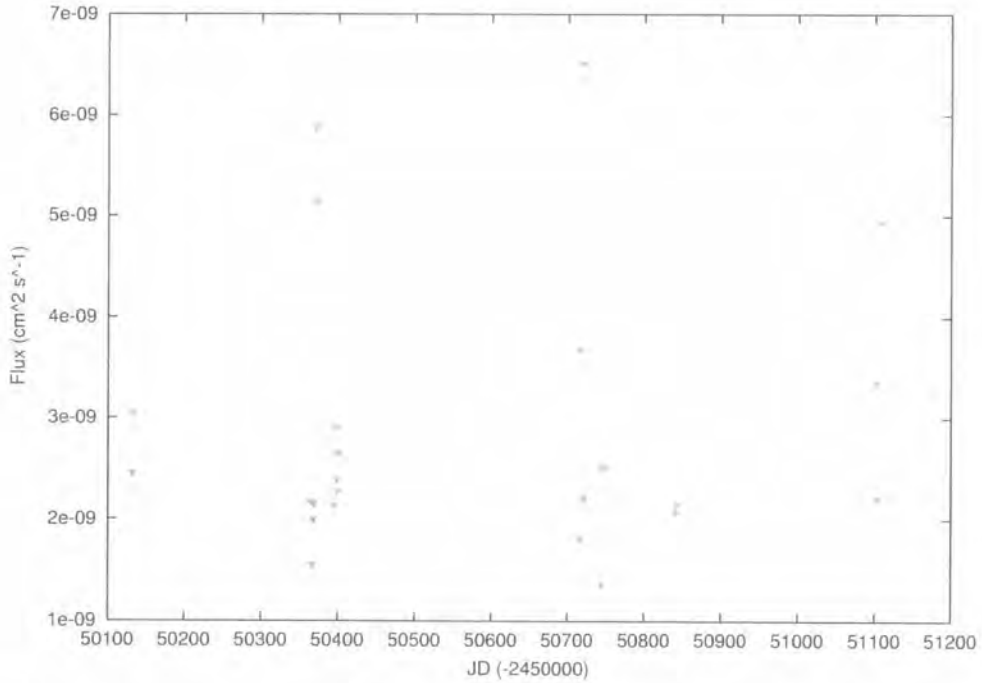

Figure 8.17: Lightcurve for observations of PKS 0548–322 between 1996 and 1998. All points are 3σ upper limits.

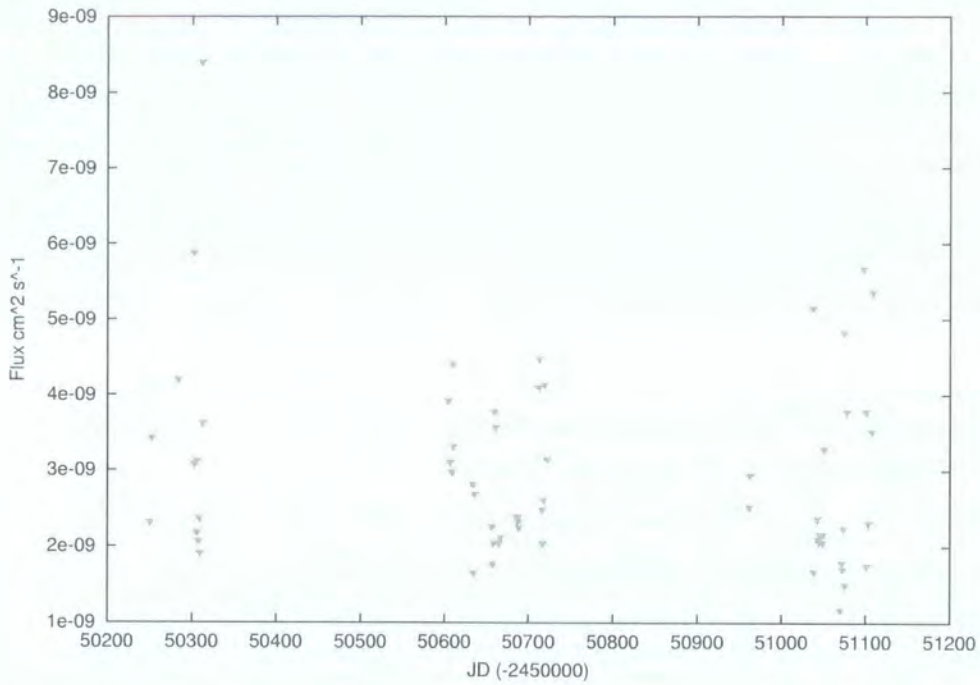

Figure 8.18: Lightcurve for observations of PKS 2005–489 between 1996 and 1998. All points are 3σ upper limits.

Figure 8.19 and 8.20 show the distribution of cosmic ray rates averaged monthly and yearly, respectively. The cosmic ray rate varies from observation to observations because of changes in the atmosphere, giving rise to the spread of cosmic ray rates seen particularly in figure 8.19.

A false source analysis plot was produced for PKS 2005–489 and PKS 0548–322 and can be seen in figures 8.21 and 8.22, respectively. No evidence for the presence of a source in the field of view is seen. The 3σ upper limit for VHE gamma ray emission at energies greater than 700 GeV was determined to be 4.8×10^{-12} cm^{-2} s^{-1} for PKS 2005–489 and 7.6×10^{-12} cm^{-2} s^{-1} for PKS 0548–322.

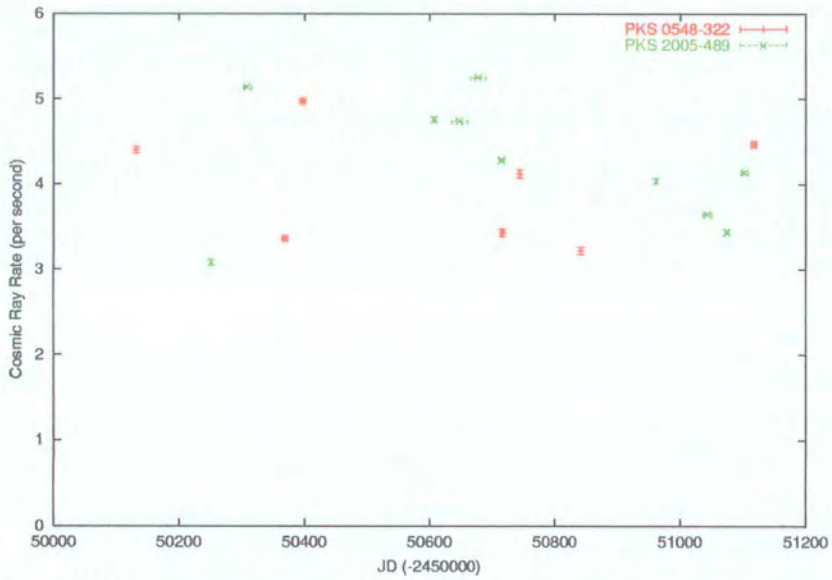

Figure 8.19: The observed cosmic ray rate during observations of PKS 0548–322 and PKS 2005–489 averaged over a year.

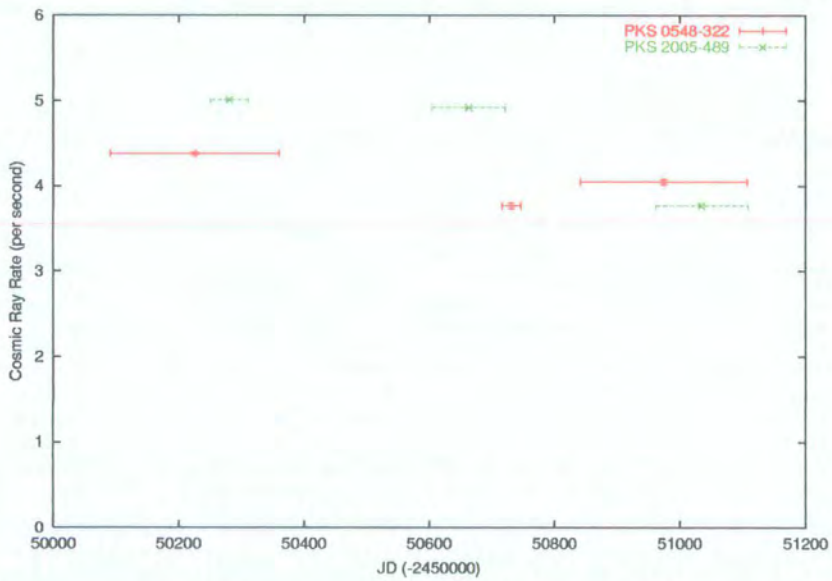

Figure 8.20: The observed cosmic ray rate during observations of PKS 0548–322 and PKS 2005–489 averaged monthly.

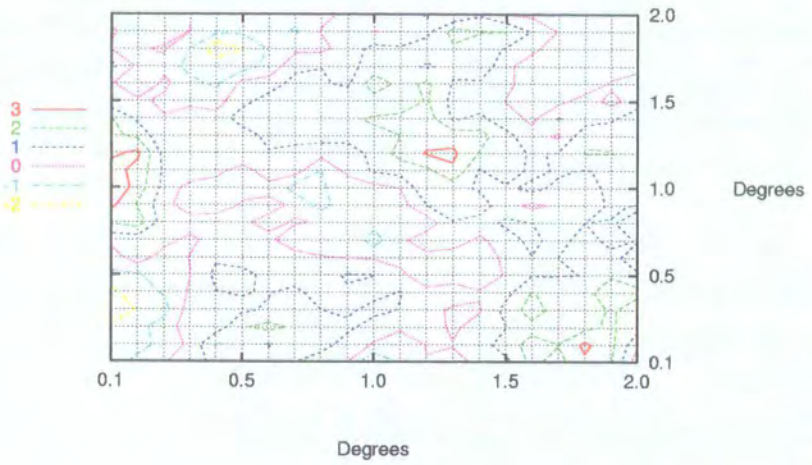

Figure 8.21: False source analysis plot for PKS 2005–489 in terms of σ in the field of view of the detector.

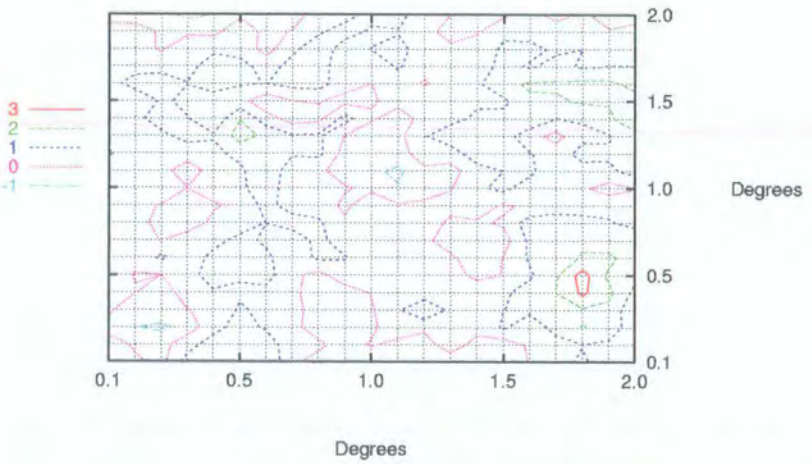

Figure 8.22: False source analysis plot for PKS 0548–322 in terms of σ in the field of view of the detector.

8.4 X-ray Data

Only RXTE ASM data were available for the same times as the Mark 6 data. Graphs of the X-ray versus gamma ray data can be seen in figure 8.23. The correlation coefficients were found to be 0.012 for PKS 2005–489 and -0.256 for PKS 0548–322 . This provides no evidence for X-ray – gamma ray correlation for PKS 2005–489 and a slight anti-correlation for PKS 0548–322 .

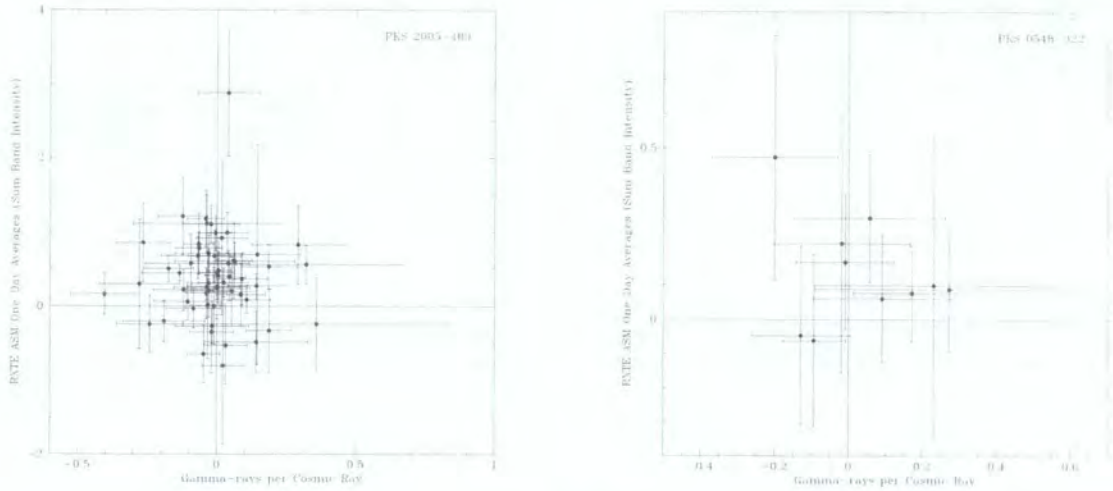

Figure 8.23: Correlation between the Daily rate of gamma rays per cosmic ray and the RXTE ASM One Day Average Intensity Values for PKS 2005–489 (left) and PKS 0548–322 (right). Neither source shows any strong indication of correlation.

8.5 Discussion

Synchrotron self-Compton and External Compton models can account for the phenomenology of gamma ray bright blazars (e.g. Fossati et al. 1998, Ghisellini et al. 1998). These

models predict that

- there is a fixed ratio between the frequencies of the Compton and synchrotron energy peaks of 5×10^8.
- the high energy peak luminosity and the radio luminosity (at 5 GHz) have a fixed ratio of 3×10^3.

Stecker et al. (1996) made predictions of the VHE flux from these objects, using a simple model for the VHE emission and taking into account absorption on the IR background. They use simple arguments to relate the VHE fluxes to the X-ray flux assuming that the emission is similar to that observed for Mrk 421. These points are included in the SEDs in figures 8.6 and 8.7. It should be emphasised that the models of Fossati et al. (1998), Ghisellini et al. (1998) and Stecker et al. (1996) are descriptive of classes of blazars, but do not provide accurate predictions for individual objects. Naturally, these models are consistent with the detailed TeV spectra available for Mrk 421 and Mrk 501, but it is far from clear that all blazars can be fully characterised by the synchrotron luminosity and the peak energy flux frequency alone. A further caveat when using descriptive models to predict the flux for an individual object arises from the fact that the compiled SEDs are not derived from simultaneous measurements and may be subject to significant observing biases. Many EGRET blazars are only seen in outburst, whereas radio measurements may be dominated by quiescent emission. Even with these reservations, it is still helpful to consider the order of magnitude prediction generated by applying these models to these objects. PKS 2005–489 shows very different temporal behaviour in outburst to that of either Mrk 421 or Mrk 501. The latter two objects both show short timescale variations

($\sim$ 15 min). The RXTE X-ray light curve of PKS 2005–489 during the 1998 outburst shows no evidence of variations on timescales of less than a day (Perlman et al. 1999). This suggests that a detailed model of this particular object must invoke factors that explain this difference and which may also affect the TeV emission. The VHE observations ended well before the peak of the outburst, so the upper limits given do not constrain correlation models as strongly as would be the case if the outburst had occurred three weeks earlier.

Figures 8.6 and 8.7 show the broadband SEDs for PKS 2005–489 and PKS 0548–322 respectively. Data points at other wavelengths are taken from the compilation of Fossati et al. (1998) and were obtained by averaging all available data in wavelength bands. Upper limits from this work have been calculated assuming a differential spectral index of 2.6. It was noted that the new limits to VHE emission provide a much stronger constraint to the SEDs than previously reported results. We can use these SEDs to test whether these measurements suggest that these objects conform to the prediction of the model of Fossati et al. (1998). For PKS 0548–322 the synchrotron peak is seen to occur at a frequency of $\geq 10^{17.5}$ Hz. This in turn implies that the Compton peak should occur at $\geq 1.5 \times 10^{26}$ Hz or ≥ 0.6 TeV. The radio flux at 5 GHz is measured to be $\sim 1.2 \times 10^{-14}$ erg cm^{-2} s^{-1} (Kühr et al. 1981, Stickel et al. 1991, Giommi et al. 1995) which leads to an expected flux at the Compton peak (0.6 TeV) of 3.6×10^{-11} cm^{-2} s^{-1}. Similarly for PKS 2005–489, the SED (figure 8.6) indicates that the synchrotron peak occurs at about 10^{16} Hz. The model of Fossati et al. (1998) then predicts that the Compton peak will occur at about 5×10^{24} Hz i.e. $\sim$ 20 GeV. The radio flux at 5 GHz is measured to be 6.05×10^{-14} erg cm^{-2} s^{-1} (Wall et al. 1986) which leads to an expected flux at the Compton peak (20 GeV) of 1.8×10^{-10} cm^{-2} s^{-1}. Neither of these predictions is in conflict

with limits to the VHE emission from these objects. The emission model described by Stecker et al. (1996) predicts values of 0.51×10^{-11} cm^{-2} s^{-1} for the VHE flux from PKS 2005–489 and 1.3×10^{-11} cm^{-2} s^{-1} for PKS 0548–322. The experimental upper limits determined from Mark 6 observations are not in conflict with these predictions. Using an inhomogeneous jet model (from Ghisellini et al. (1985)), Sambruna et al. (1996) have modelled the expected VHE flux from PKS 2005–489. They predict a sharp cut-off in the Compton peak at about 100 GeV. Again, this is not in conflict with the present results.

A multiwavelength campaign on PKS 2005–489 occurred during September and October 1998. During this period there was a large X-ray flare from PKS 2005–489 which lasted until December 1998 (Remillard 1998, Perlman et al. 1999). VHE observations were made with the Mark 6 telescope at all times that weather conditions and moon phase permitted during October 1998. PKS 2005–489 was at too large zenith angles during November and December for meaningful observations to be made. The Mark 6 observations are discussed in section 8.3. VHE observations were available for 1998 October 15, 17, 21 and 22. Stecker et al. (1996) use the relation

$$\nu_{\rm x} F_{\rm x} \sim \nu_{\rm TeV} F_{\rm TeV} \tag{8.1}$$

to predict the TeV emission from a source. The daily gamma ray upper limits together with the X-ray rates from Perlman et al. (1999) and those predicted by the model by Stecker et al. (1996) are shown in table 8.6. There was no indication of VHE emission at the sensitivities achievable with the Mark 6 during this flare. Table 8.6 also lists the predicted values for VHE gamma ray emission, based on the Stecker et al. (1996) model.

On all three nights, the predicted values and the upper limits are of the same order.

Date	$F_{>700\ GeV}$ ($\times 10^{-11}$ cm^{-2}s^{-1})	$F_{2-10\ keV}$ ($\times 10^{-10}$ erg cm^{-2} s^{-1})	$^{*}F_{>700\ GeV}$ ($\times 10^{-11}$ cm^{-2}s^{-1})
15 October 1998	2.2	16.78	2.6
17 October 1998	3.9	–	–
21 October 1998	2.6	16.37	2.5
22 October 1998	4.4	15.40	2.4

Table 8.6: The 3σ upper limits to integral flux emission above 0.7 TeV from PKS 2005–489 during the 1998 flare. The X-ray measurements are from the RXTE observations of Perlman et al. (1999). The fourth column, labelled with *, lists the values of $F_{>0.7\ TeV}$ predicted using the model described by Stecker et al. (1996).

8.6 Conclusion

Neither PKS 2005–489 nor PKS 0548–322 was detected with the University of Durham Mark 6 telescope over its lifetime. The 3σ upper limits for detection were determined to be 4.8×10^{-12} cm^{-2} s^{-1} above 700 GeV for PKS 2005–489 and 7.6×10^{-12} cm^{-2} s^{-1} above 700 GeV for PKS 0548–322 . The threshold energy, defined as the peak of the differential triggering spectrum, for the observations has been estimated on the basis of simulations reported in Nolan (2002). The effective collecting area was determined to be 1.7×10^{9} cm^{2} at an energy threshold of 700 GeV (see figure 1.8). These results are not in conflict with predictions of Stecker et al. (1996) and Fossati et al. (1998). Unfortunately they cannot place any constraints on currently favoured gamma ray emission models, though

they are more constraining than any previous measurements. The broad-band spectral energy distributions of these two objects are not as well sampled as those of Mrk 501 and Mrk 421. In spite of this we observe that the broad-band SEDs for PKS 0548–322 and PKS 2005–489 compiled here bear a resemblance to those compiled for Mrk 501 and Mrk 421 respectively, e.g. by Kubo et al. (1998). PKS 0548–322 shows a broader, higher energy synchrotron peak than PKS 2005–489, which is similar to the comparison between Mrk 501 and Mrk 421. Mrk 501 and Mrk 421 are both at similar distance ($z = 0.033$ and $z = 0.031$ respectively) but show different VHE spectral shapes (Krennrich et al. 1999). Thus the different VHE spectral shapes must be due to variation in the intrinsic source spectrum and so the effects of gamma ray absorption on the IR background cannot be determined. Studies of VHE spectra from PKS 0548–322 and PKS 2005–489 with H.E.S.S. and CANGAROO III hold out the prospect of separating the effects of the source spectrum variation and IR absorption. The next generation of telescopes with larger collecting area and improved detectors will, it is hoped, shed some light on the processes at work in these objects.

Chapter 9

The Future

9.1 H.E.S.S. Observations of PKS 2155–304

The H.E.S.S. collaboration observed PKS 2155–304 during July and October 2002 using the first two telescopes of H.E.S.S. Phase I (energy threshold $\sim$ 150 GeV). Preliminary analysis indicates that during this time, PKS 2155–304 was detected to a total significance level of 11.9 σ. This was determined from less than 7 hours of on-source observations, 2.2 hours in July 2002 at a significance of 9.9 σ and 4.7 hours in October 2002 at a significance of 6.6 σ. This is an indication that the TeV emission from PKS 2155–304 may have decreased during the intervening months.

This positive detection of PKS 2155–304 using the first H.E.S.S. telescope was reported in Djannati-Ataï et al. (2003). An estimation of the TeV flux of PKS 2155–304 has not been reported at this time.

Figure 9.1 shows the RXTE ASM one day average counts for PKS 2155–304 between July and November 2002.

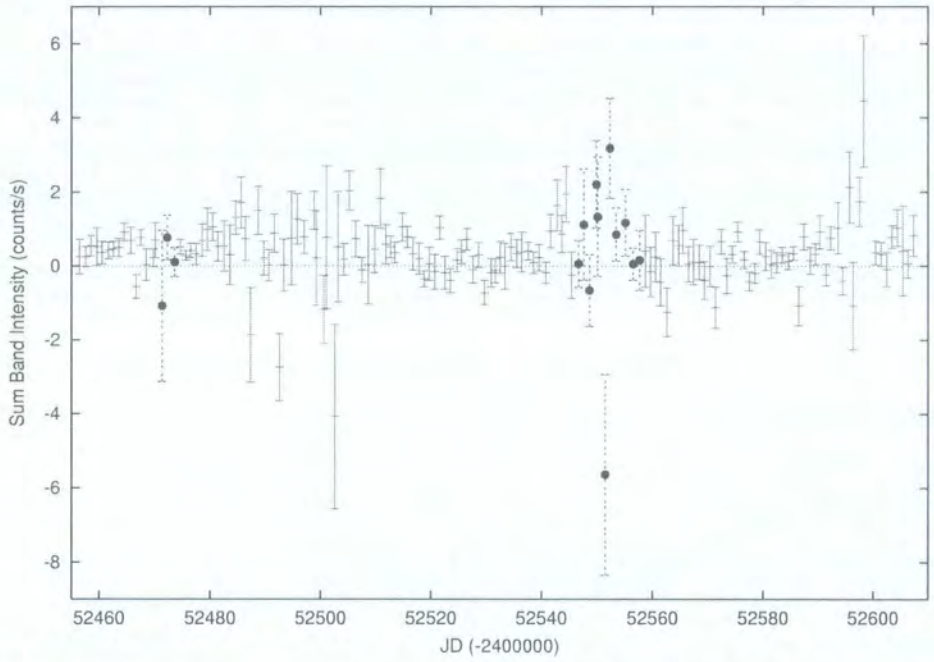

Figure 9.1: RXTE one day average values in 2002. Black circles indicate that H.E.S.S. was observing at this time.

The average count rate for these ASM observations is 0.29 counts s^{-1} for the time when H.E.S.S. observed PKS 2155–304. This is lower than it was when the Mark 6 detected PKS 2155–304 in 1996/1997, when the ASM recorded 0.37 counts s^{-1}.

H.E.S.S. was capable of detecting high energy gamma rays from PKS 2155–304 when it was not in outburst, as evidenced by the X-ray observations. This is a reflection on the sensitivity of the H.E.S.S. array. Observations of the Crab Nebula between the zenith angles of 45° and 50° for a total of 4.65 hours gave a 20.1σ detection. This equates to 3.6 gamma rays per minute. As the analysis is refined, the significance of these results and the effective sensitivity of the experiment are likely to increase.

9.2 More TeV Blazars

With the new generation of Cherenkov telescopes, such as H.E.S.S. and CANGAROO III, it is likely that more Southern hemisphere blazars will be detected at TeV energies. This will assist the efforts to determine the nature of the infrared background as outlined in section 4.5.

Costamante & Ghisellini (2002) describe a scheme for identifying the most likely TeV emitting blazar candidates.

They claim that the two ingredients for a strong TeV emission by the synchrotron self Compton process are the density of electrons energetic enough to produce TeV photons and the density of seed photons to be scattered. For synchrotron frequencies which are not too large, the scattering process between photons at the synchrotron peak and the electrons producing the peak itself is in the Thomson regime. In this case the relevant electrons could scatter the bulk of the synchrotron photons to high energies.

Therefore, according to Costamante & Ghisellini (2002), the best TeV blazar candidates should have both a large $\nu_{\rm peak}$ and a sufficiently strong soft seed IR photon emission. They expect that $\sim$ 100 more TeV gamma ray blazars will be detected by the new generation of Cherenkov telescopes.

Table 9.1 lists a number of blazars that should be targeted by H.E.S.S. in the search for TeV emitting blazars. They are the subset of the list of potential sources predicted in Costamante & Ghisellini (2002) that culminate within 45° of the zenith, as observable by H.E.S.S.

The performance of an atmospheric Cherenkov telescope varies with the zenith angle

of the source. At zenith angles greater than 45° the raw trigger rate decreases significantly. However, there is an advantage of observing at larger zenith angles in that, although the energy threshold of an array will increase, there is an increase in the effective area for the higher energy events.

Blazar Name	Redshift	Blazar Name	Redshift
*0229+200	0.139	1101–232	0.186
0323+022	0.147	*1114+202	0.139
0414+009	0.287	1440+122	0.162
0548–322	0.069	*1553+113	0.360
0556–384	0.034	*1722+119	0.018
0809+024	unknown	1741+196	0.084
0851+203	0.306	2005–489	0.071

Table 9.1: A list of potential TeV blazars observable by H.E.S.S., based on criteria outlined in Costamante & Ghisellini (2002). Those marked with an asterisk (*) have an upper limit to emission imposed on them by Whipple observations (de la Calle Pérez 2003)

9.3 Future Multiwavelength Campaigns

Multiwavelength campaigns have already been approved by H.E.S.S. and XMM to observe PKS 2005–489 and PKS 0548–322 as well as another southern hemisphere blazar 1ES 1101–232 in 2004. These will be carried out in order to determine the connection between X-rays and gamma rays from these objects.

This will be the first time that PKS 0548–322 has been the subject of a multiwave-

length campaign. The superior sensitivity of H.E.S.S. and XMM will provide multiwavelength observations of blazars of unprecedented quality.

9.4 Conclusion

Observations with the new generation of more sensitive telescopes will help to provide answers to the questions surrounding the nature of gamma ray production within blazars. Furthermore, extending the sample of VHE gamma ray emitting blazars at a range of redshifts may allow the determination of the IRB.

Recent HEGRA observations of M87, a radio galaxy at $z = 0.00436$, give a 4σ detection of gamma rays of greater than 730 GeV. If this source were confirmed as a gamma ray emitter, another class of AGN as potential TeV emitters would be established. Until now, only the blazar class of AGN has been detected at TeV energies. H.E.S.S. should also target close radio galaxies to attempt to discover more examples if M87 is detected. This would open an exciting new avenue for exploration in gamma ray astronomy.

Appendix A

Definition of the Hillas Parameters

Suppose the i^{th} PMT is given coordinates x_i, y_i (in degrees) and registers a signal s_i. The origin of the coordinate system is in the centre of the array of PMTs. An ellipse is fitted to the image and the Hillas parameters are calculated relative to the centre. Most of these parameters are illustrated in figure 1.6.

The fitting of the ellipse employs the following simple moments:

$$\begin{aligned}
\langle x \rangle &= \frac{\Sigma s_i x_i}{\Sigma s_i} \\
\langle y \rangle &= \frac{\Sigma s_i y_i}{\Sigma s_i} \\
\langle x^2 \rangle &= \frac{\Sigma s_i x_i^2}{\Sigma s_i} \\
\langle y^2 \rangle &= \frac{\Sigma s_i y_i^2}{\Sigma s_i} \\
\langle xy \rangle &= \frac{\Sigma s_i x_i y_i}{\Sigma s_i} \\
\langle x^3 \rangle &= \frac{\Sigma s_i x_i^3}{\Sigma s_i} \\
\langle y^3 \rangle &= \frac{\Sigma s_i y_i^3}{\Sigma s_i}
\end{aligned}$$

$$\begin{aligned} \langle x^2 y \rangle &= \frac{\Sigma s_i x_i^2 y_i}{\Sigma s_i} \\ \langle x y^2 \rangle &= \frac{\Sigma s_i x_i y_i^2}{\Sigma s_i} \end{aligned} \tag{A.1}$$

and

$$\begin{aligned} \sigma_{x^2} &= \langle x^2 \rangle - \langle x \rangle^2 \\ \sigma_{y^2} &= \langle y^2 \rangle - \langle y \rangle^2 \\ \sigma_{xy} &= \langle xy \rangle - \langle x \rangle \langle y \rangle \\ \sigma_{x^3} &= \langle x^3 \rangle - 3\langle x \rangle \langle x^2 \rangle + 2\langle x \rangle^3 \\ \sigma_{y^3} &= \langle y^3 \rangle - 3\langle y \rangle \langle y^2 \rangle + 2\langle y \rangle^3 \\ \sigma_{x^2 y} &= \langle x^2 y \rangle - 2\langle xy \rangle \langle x \rangle + 2\langle x \rangle^2 \langle y \rangle - \langle x^2 \rangle \langle y \rangle \\ \sigma_{x y^2} &= \langle x y^2 \rangle - 2\langle xy \rangle \langle y \rangle + 2\langle x \rangle \langle y \rangle^2 - \langle x \rangle \langle y^2 \rangle \end{aligned} \tag{A.2}$$

Given the following definitions:

$$\begin{aligned} k &= \sigma_{y^2} - \sigma_{x^2} \\ l &= \sqrt{k^2 + 4\sigma_{xy}^2} \\ m &= \langle y^2 \rangle - \langle x^2 \rangle \\ n &= \sqrt{m^2 + 4\langle xy \rangle^2} \\ u &= 1 + \frac{k}{l} \\ v &= 2 - u \end{aligned}$$

(A.3)

the Hillas parameters calculated from:

$$\begin{aligned}
\langle Size \rangle &= \Sigma s_i \\
\langle Length \rangle^2 &= \frac{\sigma_{x^2} + \sigma_{y^2} + l}{2} \\
\langle Width \rangle^2 &= \frac{\sigma_{x^2} + \sigma_{y^2} - l}{2} \\
\langle Miss \rangle^2 &= \frac{u\langle x \rangle^2 + v\langle y \rangle^2}{2} - \frac{2\langle xy \rangle \sigma_{xy}}{l} \\
\langle Distance \rangle^2 &= \langle x \rangle^2 + \langle y \rangle^2 \\
\langle Alpha \rangle &= \sin^{-1}\left(\frac{\langle Miss \rangle}{\langle Distance \rangle}\right) \\
\langle Azwidth \rangle^2 &= \frac{\langle x^2 \rangle + \langle y^2 \rangle - n}{2}
\end{aligned}$$

(A.4)

Taken from (Dunlea 2001).

Appendix B

Bethe Heitler Pair Production

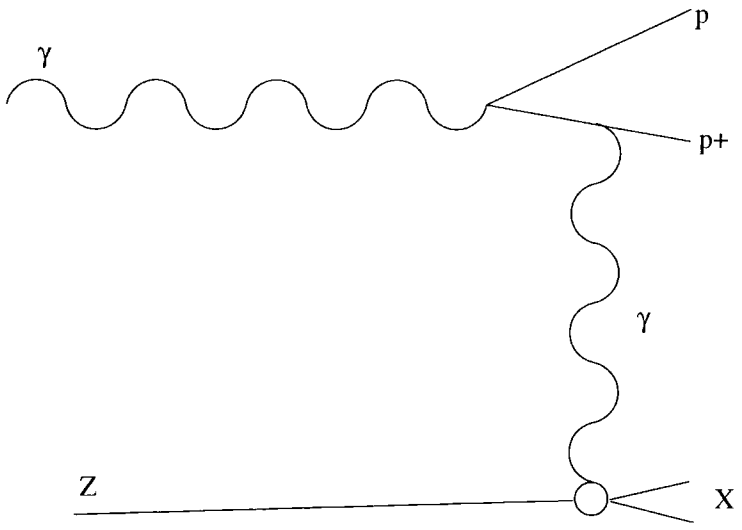

Figure B.1: A Feynman diagram illustrating the Bethe-Heitler pair production process (Bauer & Leuschner 1999). p and p^+ are leptons.

The Bethe-Heitler pair production process involves a photon pair producing in the presence of a nucleus.

Bibliography

Aharonian, F. A., et al., 1997, A&A, 327, L5

Aharonian, F. A., et al., 1999a, A&A, 349, 11

Aharonian, F. A., et al., 1999b, A&A, 350, 757

Aharonian, F. A., 2000, New Astronomy, 5, 377

Aharonian, F. A., et al., 2001, A&A, 366, 62

Aharonian, F. A., et al., 2002, A&A 384, L23

Angel, J. R. P., & Stockman, H. S., 1980, ARA&A, 18, 321

Antonucci,R. R. J. & Ulvestad, J. S., 1984, Nature, 308, 617

Atkins, R., et al., 2004, astro-ph/0403097

Aye, K.-M., et al., 2001, Proc. 27^{th} Int. Cosmic Ray Conf., Hamburg, 7, 2597

Aye, K.-M., et al., 2003, Proc. 28^{th} Int. Cosmic Ray Conf., Tsukuba, to be published

Balbus, S. A. & Hawley, J. F., 1991, ApJ, 376, 214

Barr, P., et al., 1988, ApJ, 324, L11

Bauer, G. & Leuschner, A., 1999, hep-ph/99003345

Bazer-Bachi, R., et al., 2001 in AIP Conf. Proc., 558, High Energy gamma ray Astronomy, ed. F.A. Aharonian & H. J. Völk (New York: AIP), 643

Bednarek, J. N., Kirk, J. G., & Mastichiadis, A., 1996a, A&AS, 307, L17

Bednarek, J. N., Kirk, J. G., & Mastichiadis, A., 1996b, A&AS, 120, 571

Begelman, M. C. & Sikora, M., 1987, ApJ, 322, 650

Begelman, M. C., et al., 1990, ApH, 362, 38

Bernlöhr, K., 2000, APh, 12, 255

Bekki, K., 1999, ApJ, submitted (astro-ph/9904044)

BeppoSAX Archive site: `http://www.asdc.asi.it/mmia/index.php?mission=saxnfi`, last visited 6th July 2003

Bertone, E., et al., 2000, A&A, 356, 1

Bersanelli et al., AJ, 104, 28

Biller, S. D., et al., 1998, Physical Review Letters, 80, 2992

Blandford, R. D. 1993 in Compton gamma ray Observatory, AIP Conf. Proc, 280, ed. M. Friedlander, N. Gehrels & D. J. Macomb (New York: AIP), 533

Blandford, R. D. & Konigl, A., 1979, ApJ, 232, 34

Blandford, R. D. & Levinson, A, 1995, ApJ, 441, 79

Blandford, R. D. & Payne, D. G., 1982, MNRAS, 199, 883

Blandford, R. D., & Rees, M. J., 1974, MNRAS, 169, 395

Blandford, R. D., & Rees, M. J., 1978, in Pittsburgh Conference on N Lac Objects, ed. A. N. Wolfe (Pittsurgh: Pittsburgh Univ. Press), 328

Blandford, R. D. & Znajek, R. L., 1977, MNRAS, 179, 433

Blumenthal, G. R., & Gould, R. J., 1970, Rev. Mod. Phys., 42, 237

Bond, J. R., et al. 1984, ApJ, 277, 445

Boyzan, E., et al., 1990, AJ, 99, 1421

Bregman, J. N., et al., 1990, ApJ, 352, 574

Brinkmann, W., et al. 1994, A&A, 288, 433

Brinkmann, W., et al. 2000, A&A, 362, 105

Buckley, J. H., et al., 1996, ApJ, 472, L9

Buckley, D. J., et al., 1998, Exp. Astron., 9, 237

Burbidge, G., & Hewitt, A., 1992, in Varibility of Blazars, ed. E. Valtaoja & M. Valtonen (Cambridge:Cambridge Univ. Press), 4

Camenzind, M., & Krockenberger, M., 1992, A&A, 255, 59

Canizares, C. R., & Kruper, J., 1984, ApJ, 278, L99

Carni, M. T., & Miller, H. R., 1992, ApJ, 385, 146

Carr, J. R., 1984, ApJ, 277, 445

Catanese, M., et al. 1997, ApJ, 487, L143

Cawley, M. F., et al., 1990, ExA, 1, 173

Celotti, A., Maraschi, L., & Treves, A., 1991, ApJ, 377, 403

Celotti, A., 2002 in Relativistic Flows in Astrophysics, ed. Guthmann, A. W., et al. Springer

Chadwick, P. M., et al., 1999a, ApJ, 513, 161

Chadwick, P. M., et al., 1999b, J. Phys. G: Nucl. Part. Phys., 25, 1749

Chadwick, P.M. et al., A&A, 364, 450c

Cheng, K. S., & Ding , W. K. Y., 1994, A&A, 288, 97

Chiapetti, L., et al., 1999, ApJ, 521, 552

Ciliegi, P., et al., 1993, ApJS, 85, 111

Cooke, B. A., et al., 1978, MNRAS, 182, 489

Costamante, L. & Ghisellini, G., 2002, A&A, 384, 56

Courvoisier, T. J.-L., et al., 1995, ApJ, 438, 108

Dahari, O. A., 1984, AJ, 89, 966

de la Calle Pérez et al., 2003, ApJ, 559, 909

Dermer, C. D., & Schlickeiser, R., 1993, ApJ, 416, 458

Dermer, C. D., & Schlickeiser, R., 1994, ApJS, 90, 945

Dermer, C. D., et al. 1992, A&A, 256, L27

Dermer, C. D., et al. 1993, ApJ, 416, 458

Djannati-Ataï,A., et al., 1999, A&a, 350, 17

Djannati-Ataï,A., et al., 2003, Proc. 28th Int. Cosmic Ray Conf., Tsukuba, to be published

Dondi, L., & Ghisellini, G., 1995, MNRAS, 273, 583

Dunlea, S., 2001, Ph.D Thesis, University College Dublin, "TeV Astrophysical Gamma ray selection using a multivariate Kernel selection algorithm"

Edelson, R. A, & Krolik, J. H., 1988, ApJ, 333, 646

Edelson, R., 1992, ApJ, 401, 516

Edelson, R., 1992, ApJS, 83, 1

Edelson, R., et al., 1995, ApJ, 438, 120

Edge, D. O., 1959, Mem. R. Astron. Soc., 68, 37

Eichler, D. & Witta, P. J., 1978, Nature, 274, 38

Fath, E. A., 1908, Lick Obs. Bull. 5, 71

Falomo, R. et al., 1987, ApJ, 318, L39

Falomo, R. et al., 1995, ApJ, 438, L9

Falomo, R. 1996, MNRAS, 283, 241

Falomo, R., Scarpa, R., Treves, A. & Urry, C. M. 2000, ApJ, 542, 731

Fan, J. H., & Lin, R. G., 2000, 355, 880

Fanaroff, B. L., and Riley, J. M., 1974, MNRAS, 167, 31

Fegan, D. J., 1997, J. Phys G: Nucl. Part. Phys, 23, 1013

Fichtel, C. E., 1994, ApJS, 94, 551

Flynn, C. `http://www.astro.utu.fi/~cflynn/astroII/l8.html` visited 9th January 2004.

Fosbury, R. A. R., & Disney, M. J., 1976, ApJ, 207, 75

Fossati, et al., 1998, MNRAS, 299, 443

Frank, I. & Tamm, I., 1937, Dokl, Akad, Nauk. 14, 109

Gaidos, J. A., et al. 1996, Nature, 383, 319

Georganopoulos, M. & Marsher, A., 1996, in ASP Conf. Ser. 110, Blazar Continuum Variability, ed. H. R. Miller, J. R. Webb, & J. C. Noble (San Francisco: ASP), 262

Georganopoulos, M. & Marsher, A., 1998, ApJ, 506, L11

George, I. M., & Fabian, A. C., 1991, MNRAS, 249, 352

Ghisellini, G., et al., 1985, A&A, 146, 204

Ghisellini, G., et al., 1998, MNRAS, 306, 247

Ghisellini, G., & Madau, P., 1996, MNRAS, 280, 67

Ghisellini, G., et al., 1996, A&AS, 120, C503

Ghisellini, G., & Maraschi, L. 1989, ApJ, 340, 181

Ghisellini, G., & Maraschi, L. 1996, in ASP Conf. Proc. 110, Blazar Continuum Variability, ed. H. R. Miller, J. R. Webb, & J. C. Noble (San Francisco: ASP),436

Ghosh, K. K., & Soundararajaperumal, S., 1995, ApJS, 100, 37

Giommi, P., et al., et al., 1990, ApJ, 356, 432

Giommi, P., et al., et al., 1995 check this reference and the one below it

Giommi, P., Ansari, S. G., & Micol, A., 1995, A&AS, 109, 267

Ginzburg, V. L. & Syrovatskii, S. I., 1965, ARA&A, 3, 297

Ginzburg, V. L. & Syrovatskii, S. I., 1969, ARA&A, 7, 375

Goeckel, 1910, Phys. Zeits., 11, 280

Gould, R. J., 1965 Physics Review Letters, 15, 577

Gould, R. J., & Jung, Y.-D., 1991, ApJ, 373, 271

Griffiths, R. E., et al., 1979, ApJ, 234, 810

Hartman, R. C., et al., 1999, ApJS, 123, 79

Heckman, T. et al., 1986, 1986, ApJ, 311, 526

Heidt, J., et al., A&A, 341, 683

Hess, V. F., 1911, Phys. Zeits., 12, 998

Hewitt, A., & Burbidge, G., 1993, ApJS, 87, 451

Hillas, A. M., 1985, ICRC, La Jolla, 3, 445

Hillas, A. M., 1996, Sp. Sci. Rev. 75, 17

Hillas, A. M., 1999, APh, 11, 27

Ho, L. C., et al., 1993, AAS, 182, 1705

Horan, D., et al., 2002, ApJ, 571, 753

Hutchings, J. B., 1989 ApJ, 342, 660

Impey, C. D, & Neugebauer, G., 1988, AJ, 95, 307

Jannuzi, B. T., 1994, ApJ, 428, 130

Jelley, J. V., 1958, "Cherenkov Radiaion and its Applications" Pergamon Press.

Jones, T. W., et al., 1974, ApJ, 188, 353

Jurkevich I., 1971, Ap&SS 13, 154

Kataoka, J., et al., 2000, ApJ, 528, 243

Kembhavi, A. K., & Narlikar. J. V., 1999, Quasars and Active Galacitc Nuclei an Introduction, Cambridge University Press.

Kinman, T. D. 1978 in Proc. Pittsburgh Conf. on Bl Lac Objects, ed. A. M. Wolfe (Pittsburgh: Univ. of Pittsburgh), 82

Krawczynski, H., et al., 2002, MNRAS, 336, 721

Krawczynski, H., et al., in AIP Conf. Proc., 558, High Energy gamma ray Astronomy, ed. F.A. Aharonian & H. J. Völk (New York: AIP), 639

Krennrich, F., et al., 1999, ApJ, 511, 149

Kifune, T., et al., 1995, ApJ, 438, L91

Kino, M., et al., 2002, ApJ, 564, 97

Königl, A., 1981, ApJ, 449, L99

Königl, A., et al., 1995, ApJ, 446, 598

Kubo, H., et al., 1998, ApJ, 504, 693

Kühr, H., et al., 1981, A&AS, 45, 367

Lamb, R. C. & Macomb, D. J., 1997, ApJ, 488, 872

Lamer et al., 1996, A&A, 311, 384

Large, M. I., et al., 1981, MNRAS, 194. 1013

Learned, J., & Mannheim, K., 2000, Ann. Rev. Nucl. Part. Sci. 50, 679

Levinson, A., 1996, ApJ, 467, 546

Li, T.-P. & Ma, Y.-Q., 1983, ApJ, 272, 317

Longair, M. S., 1992, High Energy Astrophysics Volume 1: Particles, photons and their detection. Second Edition, Cambridge University Press.

Lowder, D. M., et al., 1991, Nature, 353, 331

Maccagni, D., et al., 1989, in BL Lac Objects, ed. L. Maraschi, T. Maccacaro, &M. -H., Ulrich(Berlin: Springer), 281

MacKenty, J. W., 1990, ApJS, 72, 231

Malkan, M. A. & Stecker, F. W., 1998, ApJ, 496, 13

Mannheim, K., 1993, A&A, 269, 67

Mannheim, K. & Biermann, P. L, 1992 A&A 253, L21

Maraschi, L., Ghisellini, G., Celotti, A., 1992, ApJ, 397, L5

Marscher, A., 1977, ApJ, 216, 244

Marscher, A.,& Gear, W., 1985, ApJ, 298, 114

Marshall, H. L., et al., 2001, ApJ, 549, 938

Marshall, H. L., et al., 1995, ApJ, 439, 90

Mastichiadis, A., & Kirk, J. G. 1997, A&A, 320, 19

Mattox, J. R., et al. 1993, ApJ, 410, 609

McNaron-Brown, K., et al., 1995, ApJ, 451, 575

Mead, A. R. G., et al., 1990, A&AS, 83, 183

Merrifield, M., 1995, http://www.astro.soton.ac.uk/PH308/AGN/Seyferts.html, last accessed 20/05/03

Miller, H. R., McAlister, 1983, ApJ, 272, 26

Miller, J. S. & Goodrich, R. W., 1990, ApJ, 355, 456

Mücke, A., et al., 2003, APh, 18, 593

Mukherjee, R., et al., 1996, ApJ, 470, 831

Nilsson, K. et al. 1999, PASP, 111, 1223

S.J. Nolan, 2002, Ph.D. Thesis, University of Durham, Simulation Studies of the Imaging Atmospheric Cherenkov Technique using the Durham Mark 6 and H.E.S.S. Telescopes

Osborne, et al., J. L., 2002, Bull. Astr. Soc. India, 30, 51

Padovani, P. & Urry, C. M., 192, ApJ, 387, 449

Perlman, E. S., et al., 1999, ApJ, 523, L11

Pesce, J. E., et al., AJ, 107, 494

Pesce, J. E., et al., 1997, ApJ, 486, 770

Peterson, B. M., 1997, An Introduction to Active Galactic Nuclei, Cambridge University Press.

Pica, A. J., et al., 1988, AJ, 96, 1215

Pian, E., et al. 1997, ApJ, 486, 784

Pian, E., et al. 1997, ApJ, 492, L17

Pohl, M., & Schlickeiser, R., 2000, A&A, 354, 395

Protheroe, R., 1996, in Proc. IAU Colloquim. 163, Accretion Phenomena and Related Outflows. eds. Wickramasinghe, D., et al.

Protheroe, R., 2001, in Particle and Fields in Radio Galaxies, Laing R., Blundell, K. eds., AP in press (2001)

Quinn, J., et al., 1996, ApJ, 456, L83

Quinn, J., et al., 1999, ApJ, 518, 69

Rees, M. J., et al., 1982 Nature vol. 295 Jan 7, p. 17

Rees, M. J., 1967, MNRAS, 137, 429

Remillard R., IAU Circ. 7041

Roberts, M. D., 1998, A&A, 337, 25

Roberts, M. D., 1999, A&A, 343, 691

Romero, G. E., et al., 1999, A&AS,135, 477

Romero, G. E., et al., 2002, A&A, 390, 431

Salpeter, E. E., 1964, ApJ, 140, 796

Salamon, M. H., & Stecker, F. W., 1998 ApJ, 493, 547

Sambruna, R., et al., 1994, ApJS, 95, 371

Sambruna, R., et al., 1995, ApJ, 449, 567

Sambruna, R., et al., 1996, ApJ, 463, 444

Samuelson, F. W., et al. 1998, ApJ, 501, L17

Sauty, C., et al., 2002 in Relativistic Flows in Astrophysics, ed. Guthmann, A. W., et al. Springer, 41

Savage, A., et al., 1977, MNRAS, 179, 135

Scarpa et al., 1999, ApJ, 521, 134

Schuster, C., et al., 2002, A&A, 382, 829

Schwartz, D. A., et al., 1979, ApJ, 229, L53

S.E. Shaw, 1999, Gamma/Hadron Discrimination Using Composite Chereknov Telescopes

Sembay, S., et al., 1993, ApJ, 404, 112

Sikora M., et al. 1987, ApJ, 320, L81

Sikora, M., Begelman, M. C., & Rees, M. J., 1993, in Compton gamma ray Observatory, AIP Conf. Proc, 280, ed. M. Friedlander, N. Gehrels & D. J. Macomb (New York: AIP), 598

Sikora M., 1994, ApJS, 90, 153

Sikora, M., Begelman, M. C., & Rees, M. J., 1994, ApJ, 421, 153

Sikora, M. 1997, in AIP Conf. Proc. 410, 4th Compton Symp, ed. C. Dermer, M. S. Strickman, & J. D. Kurfess (New York: AIP), 494

Sikora, M., et al., 1997, ApJ, 484, 108

Sikora, M. & Madejski, G., 2000, ApJ, 534, 109

Sikora, M., et al., 2001, ApJ, 554, 1

Slipher, V. M., 1917, Lowell Obs. Bull. 3, 59

Smith, P. S., & Sitko, M. L., 1991, ApJ 383, 580

Smith, P. S., et al., 1992, ApJ, 400, 115

Sommers, P., et al., 1987, J. Phys. G.: Nucl. Part.Phys.13, 553

Stecker, F. W. 1999, APh, 11, 83

Stecker, F. W., de Jager, O. C., & Salamon, M. H., 1992, ApJ, 390, L49

Stecker, F. W., Salamon, M. H., & de Jager, O. C., 1994, ApJ, 432, L1

Stecker, F. W., et al., 1996, ApJ, 473, L55

Stecker, F. W. & de Jager, O. C., 1997, ApJ, 476, 712

Stecker, F. W. & de Jager, O. C., 1998, A&A, 334, L85

Stecker, F. W. & Salamon, M. H., 1997, Proc. 25th Int. Cosmic Ray Conf. 3, 317

Stickel, M., et al., 1991, ApJ, 374, 431

Stickel, M., et al., 1993, A&AS, 98, 393

Swanenburg, B. N. et al., Nature, vol. 275, Sept. 28, 1978, p. 298

Tagliaferri, G., et al., AA, 368, 38

Takahashi, T., et al., et al 1996, ApJ, 470, L89

Takahashi, T., et al., et al 1999, Astropart. Phys. 11, 177

Tanihata, C., et al., 2001, ApJ, 563, 569

Tashiro, M., et al., 1994 New Horizons of X-ray Astronomy

Tashiro, M., et al., 1995, PASJ, 47, 131

Tavecchio, F., et al. 1998, ApJ, 509, 608

Tommasi, L., et al., 2001, ApJS, 132, 73

Tornikoski,M., et al., 1996, A&AS, 116, 157

Treves, A., et al., 1989, ApJ, 341, 733

Ulrich, M. -H., Maraschi, L., & Urry, C. M., 1997, ARA&A, 35, 445

Urry,C. M., & Padovani, P., 1995, PASP, 107, 83

Urry, C. M.& Mushotzky, R. F., 1982, ApJ, 253, 38

Urry, C. M., et al., 1993, ApJ, 411, 614

Urry, C. M., et al., 1997, ApJ, 486, 799

Urry, C. M., et al., 1998, In: Scarsi L., et al. (eds.) The Active X-ray Sky. Nucl. Phys. B (Proc. Suppl.) 69, 419

Vermeulen, R. C. & Cohen, M. H., 1994, ApJ, 430, 467

Vestrand, W.T., Stacy, J. G., & Sreekumar, P., 1995, ApJ, 454, L93

Vestrand, W.T., & Sreekumar, P., 1999, APh, 11, 197

von Montigny, C., et al. 1995, ApJ, 440, 525

Wagner, S. J., et al., 1995, ApJ, 454, L97

Wagner, S. J., et al., 1995, A&A, 298, 688

Wall, J. V., et al., 1975, Austalian J. Phys., Astrophys Suppl. No. 34, 55

Wall, J. V., et al., 1986, MNRAS, 216, 173

Wandel, A., & Urry, C. M., 1991, ApJ, 367, 78

Weekes, T. C., et al., 1988, Phys Reports, 160, 1

Wehrle, A. E., et al., 1998, ApJ, 497,178

Wiita, P. J., 1982, ApJ, 256, 266

Worrall, D. M., & Wilkwa, B. J., 1990, ApJ, 360, 396

Xie, G. Z., et al., 1996, AJ, 111, 1065

Xie, G. Z., et al., 1997

Yee, H. K. C., 1987, AJ, 94, 1461

Zel'dolvich, Ya.B., & Novikov, I. D., 1964 Sov. Phys. Dokl., 158, 811

Zeilik, M., Gregory, S. A., and Smith, E. v. P., 1992, Introductory Astronomy and Astrophysics, Third Edition, Saunders College Publishing

Zhang, Y. H., & Xie, G. Z., 1996, A&AS, 116, 289

Zhang, Y. H., et al., 2002, ApJ, 572, 762

Zweerink, J., et al., 1997, ApJ, 490, L141